Thermal and Electronic Transport Properties of Zinc Antimonide

by

PAUL JOHN SHAVER

CENTER FOR SPACE RESEARCH

and

ENERGY CONVERSION AND SEMICONDUCTOR LABORATORY

DEPARTMENT OF ELECTRICAL ENGINEERING

MASSACHUSETTS INSTITUTE OF TECHNOLOGY

CAMBRIDGE 39, MASSACHUSETTS

SCIENTIFIC REPORT NO. 1

on

CONTRACT: NASA Grant NsG 496 (part)

M.I.T. Task: 9827

April 20, 1965

THERMAL AND ELECTRONIC TRANSPORT
PROPERTIES OF ZINC ANTIMONIDE

by

PAUL JOHN SHAVER

CENTER FOR SPACE RESEARCH

and

ENERGY CONVERSION AND SEMICONDUCTOR LABORATORY
Department of Electrical Engineering
MASSACHUSETTS INSTITUTE OF TECHNOLOGY
Cambridge 39, Massachusetts

SCIENTIFIC REPORT NO.1

on

April 20, 1965

THERMAL AND ELECTRONIC TRANSPORT
PROPERTIES OF ZINC ANTIMONIDE

by

PAUL JOHN SHAVER

This report is identical to a thesis submitted to the Department of Electrical
Engineering, M.I.T., April 20, 1965, in partial fulfillment of the requirements
for the degree of Doctor of Science.

ABSTRACT

N65-34394

The preparation of single crystals of p-type ZnSb is described. A horizontal
zone recrystallization method was used with an antimony rich molten zone. Argon
gas was added to the sealed growth ampoule to suppress decomposition during
crystal growth. Copper doping was used to control the hole concentration. Doping
with Al, Se, or In failed to produce n-type ZnSb. Methods are described for
making electrical and thermal contacts to this material.

A reversible increase in the hole concentration of undoped, p-type crystals
was found to occur under annealing at elevated temperatures (60°C to 240°C) in
inert atmospheres. With storage at room temperature, the hole concentration was
found to relax towards the pre-annealing hole concentration. A plausible
explanation is advanced for this phenomenon.

The following measurements were made on carefully oriented, p-type single
crystal samples: thermoelectric power and thermal conductivity at 0°C; Hall
effect and electrical resistivity between 77.3 and 325°K; and magnetoresistance
measurements at 77.3°K.

These measurements indicate a slight (12%) anisotropy in the thermal
conductivity, no anisotropy in the thermoelectric power and no anisotropy in the
Hall effect. Considerable anisotropy was measured in the electrical conductivity.
It was found that $\sigma_c = 1.5 \sigma_a = 2.5 \sigma_b$, approximately.

For thermoelectric applications, the highest figure of merit is obtained
with thermal and electrical currents directed along the c-axis of the crystal.
At 0°C, the maximum thermoelectric figure of merit was found to be $0.74 \times 10^{-3} (°K)^{-1}$.
The thermal conductivity at this doping level was 0.037 watts/cm-°K which is
about twice the value for polycrystalline ZnSb.

The experimentally observed results of the galvanomagnetic measurements are
shown to be in excellent agreement with a model for the valence band conduction
processes which assumes that: a single general ellipsoid describes surfaces of
constant energy in reciprocal space and that the relaxation time is either a
scalar function of energy or a tensor of constants with a factorable energy
dependence.

Author

ACKNOWLEDGEMENTS

TABLE OF CONTENTS

LIST OF TABLES

LIST OF FIGURES

CHAPTER 1

LITERATURE SURVEY, SUMMARY OF
PREVIOUSLY DETERMINED PROPERTIES OF ZnSb
AND OUTLINE OF EXPERIMENTAL WORK

1.1 LITERATURE SURVEY

Modern interest in the thermoelectric properties and applications of
zinc antimonide began with the researches of Maria Telkes in 1936.[1] In
1947, Telkes[2] measured a conversion efficiency of 5.6% for a zinc antimonide
versus constantan thermoelectric power generator that operated between 400°C
and 0°C. Telkes[3], in 1954, reported efficiencies versus operating temperature
differential for couples of ZnSb versus constantan and ZnSb versus a bismuth-
tin alloy. Her zinc antimonide elements were prepared by the vacuum melting
of stoichiometric charges and vacuum casting. Small amounts of tin, silver,
and bismuth were added to lower the electrical resistivity and decrease the
brittleness of the alloy. It was found necessary to anneal the alloy since
the thermoelectric power and electrical resistivity of the cast samples were
variable when the couples were operated at elevated temperatures. The anneal-
ing was carried out at a temperature of 480°C for 24 hours. In 1955[4],
Telkes summarized her work and noted that these alloys are stable up to 450°C
when properly annealed. Various combinations of additives yielded thermoelectric
powers of 200 to 300 $\mu V/°C$, electrical resistivities on the order of 2×10^{-3}
ohm-cm, and thermal conductivities of about 0.014 watt/cm - °C.

In Germany, Justi and his co-workers have been looking into the thermo-
electric properties of homogeneous, polycrystalline ZnSb and alloys of ZnSb
and CdSb, i.e., ($Zn_x Cd_{1-x} Sb$). In 1960, Justi[5] reported that the thermo-
electric power of polycrystalline ZnSb can be represented by:

$$\alpha = 629 - 200 \log_{10} \sigma$$

where α is the thermoelectric power in $\mu V/°K$ and σ is the electrical conductivity in (ohm-centimeters).$^{-1}$ Justi also concludes that Cu is the best acceptor impurity. He was not able to prepare n-type ZnSb. Justi also presents the results of his measurements of the temperature dependence of the thermoelectric power between 4.2 °K and 350 °K.

In 1961, Justi and his co-workers reported[6,7] measurements of thermo-electric power, electrical conductivity, Hall coefficient, thermal conductivity and Nernst-Ettingshausen coefficient on homogeneous, polycrystalline ZnSb at temperatures between 4.2 and 300°K. They did not interpret their results in terms of a model for the transport processes in ZnSb.

Justi and Newman describe their work on polycrystalline $Zn_xCd_{1-x}Sb$ in a U.S. patent which was granted in 1962[8]. They found that their samples had to be annealed at 460-500°C in order to avoid the high temperature instabilities that were also reported by Telkes.

Recently, Justi, Rasch and Schneider[9] have reported on the preparation and transport properties of single crystals of ZnSb. The crystals were grown by the seeded, horizontal zone recrystallization process that was used by Kot and Kretsu[15] and Eisner, Mazelsky and Tiller.[22] Results are presented for the thermoelectric power as a function of electrical conductivity and for the Hall effect, electrical conductivity, and transverse magnetoresistance as functions of temperature between room temperature and 1.9 °K. Evidence of impurity band conduction in undoped crystals below about 25 °K is noted. Copper was used as an acceptor impurity. Ga and Te were used as donor impurities in unsuccessful attempts to produce n-type ZnSb. It was found that the $\alpha^2\sigma$ product for ZnSb single crystals was significantly greater than that of polycrystalline ZnSb. However, the thermal conductivity of the single

crystalline material was also increased to about twice the value for poly-crystalline ZnSb.

Unfortunately, this work makes no mention of the crystallographic orientation of the measurement samples. Thus, the anisotropies of the electrical and thermal properties were not determined. A knowledge of these anisotropies is needed in order to infer the nature of the energy band structure of ZnSb as well as to completely determine the potential of this material for thermo-electric energy conversion applications.

In 1962, Hruby and Kasper[10] reported the use of a HF, H_2O_2 and glycerol etch to both polish and decorate ZnSb and CdSb surfaces. A year later, Hruby[11] and co-workers described the Czochralski growth of ZnSb single crystals. Pulling speeds varied between 6 to 15 mm/hour. Room temperature electrical conductivities on the order of 1.5 $(\Omega\text{-cm})^{-1}$, Hall mobilities on the order of 300 cm^2/volt-sec and hole densities on the order of 3×10^{16} cm^{-3} were reported.

Pilat and his co-workers in Russia have tried to find thermoelectrically optimum zinc and cadmium concentrations for $Zn_xCd_{1-x}Sb$[12,13]. They worked with vacuum cast polycrystalline samples. It was found that the apparent thermal activation energy, thermoelectric power, Hall coefficient, and thermal conductivity exhibited a relative maximum and electrical conductivity an absolute minimum when the molecular composition of their alloy was 50% CdSb and 50% ZnSb. Most measurements were carried out at 130°C. The authors suggest that near the 1:1 composition, a chemical compound $ZnCdSb_2$ is formed. However, Miksovsky et al.,[14] did not observe $ZnCdSb_2$ in their work on the growth of single crystals of $Zn_xCd_{1-x}Sb$.

Several Russian and American workers have reported their work with single

crystals of ZnSb. In general, available reports briefly describe the crystal growing process and give the results of simple measurements of thermoelectric power, Hall coefficient and electrical conductivity versus temperature. In 1958 Kot and Kretsu[15] obtained single crystals for seed purposes by the Bridgeman method. Small pieces of these crystals with a definite orientation were then used as seeds for growing larger single crystals by a horizontal zone melting method in evacuated Pyrex test tubes. Two planes of easy cleavage were observed but not identified crystallographically. The Hall coefficient, electrical conductivity and thermoelectric power were measured over 100 to 500 °K in two directions normal to each of the plans of easy cleavage and in a third direction that was perpendicular to these two. As was expected (the unit cell of ZnSb is orthorhombic), the above measured electrical parameters were anisotropic. It was found that annealing the crystals above 200°C affected the transport parameters. For example, after annealing for 20 hours at 250°C the electrical conductivity of a sample increased 2-3 times but the electrical conductivity slowly decreased with time when the crystals were kept at room temperature. In general, these workers observed that their crystals were p-type with a carrier concentration of about $10^{16} cm^{-3}$, and had an energy gap of about 0.6 ev which was deduced from the temperature dependence of the Hall coefficient. Their crystals exhibited the onset of intrinsic conduction at 340°K, and exhibited the following conductivities:

$$\sigma_{11} = 3.8, \ \sigma_{22} = 4.6, \ \sigma_{33} = 2.8$$

(ohm-centimeters)$^{-1}$. At 350°K, the following thermoelectric powers were observed: before annealing, $\alpha_{11} = 770$, $\alpha_{22} = 790$, $\alpha_{33} = 740$ μV/°K after annealing, $\alpha_{11} = 470$, $\alpha_{22} = 510$, $\alpha_{33} = 440$ V/°K.

Since the absolute crystallographic orientations of the samples were unknown, the apparent anisotropies in the above quantities cannot be related to definite principal axes in ZnSb.

American workers mainly have approached the investigation of ZnSb from the point of view of its being just one member of a class of group II-V semiconductors. Hence, an undivided effort has not been put into the investigation of the transport properties of ZnSb.

In 1960, Stevenson[16] reported the results of cyclotron resonance experiments on p-type ZnSb with a hole concentration of 4×10^{18} cm^{-3}. He observed a single resonance due to carriers of undentified sign of charge. His data was consistent with a single extremum energy band model with an almost spherical energy band. He observed similar results in CdSb. The single crystals used by Stevenson were pulled from a melt.

In the same year, Turner, et al.,[17] reported some of the physical properties of several II-V semiconductors (Zn_3As_2, $ZnAs_2$, ZnSb, Cd_3As_2, $CdAs_2$ and CdSb). Zinc antimonide single crystals were pulled from melts containing 29-31% zinc by weight. The resulting single crystals were p-type with a carrier concentration of about 4×10^{18} cm^{-3}. The room temperature Hall mobility was 10 cm^2/volt-sec. The energy gap was estimated to be 0.53 ev from optical absorption data. In a second paper[18] (1961), these authors further summarize the electrical and optical properties of II-V compounds.

In 1961, Silvey et al.[19] described the pulling of single crystals of the II-V compounds. They observed that ZnSb forms peritectically at 546°C. Single crystals were pulled from Zn-Sb melts containing 29-31% Zn by weight. Since the II-V compounds which were grown exhibited thermal dissociation, crystal pulling was carried out in sealed quartz tubes under a pressure of the

more volatile dissociation product.

Hirayama[20] has investigated the thermal decomposition of ZnSb. Zinc was found to be the volatile species. A heat of formation for ZnSb of:

$$\Delta H^\circ = - 3.55 \pm 1 \text{ kcal/mole}$$

is obtained from his data on the heat of dissociation.

Hansen[21] presents the phase diagram for the zinc-antimony binary system.

Eisner et al.[22] described a zone recrystallization technique which they used to grow single crystals of ZnSb which were described as being of "good quality". Single crystals almost 4 inches long were grown in sealed vycor tubes by moving a molten antimony-rich zone along a charge of stoichiometric composition headed by a single crystal of ZnSb. The crystals were quite brittle, cleaving readily along the (100) plane, occasionally along the (010) plane and rarely along the (001) plane. Simple electrical measurements on a single crystal in a direction perpendicular to <100>, at 23° to <010> and 67° to <001> yielded a thermoelectric power that increased monotonically from 420 $\mu V/°K$ at -200°C to 570 $\mu V/°K$ at + 50°C. Intrinsic conduction became dominant at 10°C. Hall measurements indicated a p-type carrier concentration of about 10^{16} cm^{-3} and an energy band gap of 0.49 ev. In the extrinsic range, the Hall constant was about 200 cm^3/coulomb and the room temperature mobility was about 500 cm^2/volt-sec and increasing to 2000 cm^2/volt-sec at 100°K.

In 1964, Zavetova[23] published a short note describing the results of room temperature optical transmission experiments on thin a, b and c plane samples of ZnSb. The crystals were prepared by the Czochralski technique and had a hole density of about 3×10^{17} cm^{-3}. A room temperature optical energy gap of 0.480 ev was obtained. This value was independent of the

plane of polarization of the light. Some evidence for an indirect energy gap was obtained.

Also in 1964, Komiya, Masumoto and Fan[24] published the results of more complete optical absorption studies on ZnSb. Brief data on the temperature dependence (77 to 340°K) and anisotropy of the Hall mobilities ($\mu_c > \mu_a > \mu_b$) was included. Absorption edge energy thresholds of 0.50 (300°K), 0.59 (77°K) and 0.61 (4.2°K) were obtained independent of polarization. Evidence for an indirect energy gap was noted. The crystals were prepared by pulling from the melt. The apparent hole concentrations were on the order of 10^{16} cm^{-3}.

In 1964, Carter and Mazelsky[25] published the results of an investigation into the crystallographic structure and chemical bonding of ZnSb. Their work supersedes that of Almin[26] and Toman[27]. In addition to refining the previously determined crystal structure, these workers theoretically infer that ZnSb is an electron transfer compound with Zn^{-1} having a valence of three and Sb^{+1} having a valence of four. This interpretation of the valence scheme is in agreement with the observations of Ugai[28].

In 1962, Frost et al.[29] briefly presented observations on the effects of nuclear reactor irradiation on the electrical properties of ZnSb. The damage incurred was principally due to fast neutrons.

Khartsiev[30] has applied group theory to the ZnSb and CdSb crystal structure and has obtained qualitative predictions of the symmetry structure of the energy bands. Frei and Velitski[31] have criticized some of the analogies that Khartsiev drew in his work.

1.2 ZnSb - A SUMMARY OF PREVIOUSLY ESTABLISHED PHYSICAL PROPERTIES

Table 1.1 presents a summary of the previously established physical properties of zinc antimonide. Much of the early work was primarily concerned with crystal growth. Only a few measurements of electrical transport properties were made to characterize the single crystals. The 1960 work of Kot and Kretsu[15] does give some information on anisotropies in the Hall effect, electrical conductivity and thermoelectric power. However, the absolute orientation of the crystals was not established. The more recent work of Justi, Rasch and Schneider[9], presents results on measurements of electrical conductivity, Hall effect, magnetoresistance, and thermoelectric power for a number of acceptor doping levels and a temperature range of 1.9°K to room temperature. A measured value for the room temperature thermal conductivity is also included. However, all of this work was done on apparently unoriented single crystal samples since no mention is made of anisotropies. The recent work of Komiya, Masumoto and Fan[24] deals mainly with optical absorption measurements in ZnSb. A determination of the anisotropy of the Hall mobility in the temperature range of 77 to 350°K was published in this paper.

1.3 OUTLINE OF EXPERIMENTAL WORK

The preceding literature survey and summary indicates that the results of a number of basic transport measurements are needed before zinc antimonide can be characterized in fundamental terms. In particular, a determination of the anisotropies in the electrical conductivity, Hall effect, thermo-electric power and magnetoresistance effects is needed to infer details of the energy band structure. A determination of the anisotropy of the thermal conductivity is needed to completely evaluate the thermoelectric applications

TABLE 1.1

ZnSb-A SUMMARY OF PREVIOUSLY ESTABLISHED PHYSICAL PROPERTIES

PROPERTY	COMMENTS	REF.
Crystallographic: ZnSb Orthorhombic crystal Class D_{2h}^{15} space group 16 atoms in the primitive unit cell	at $28.4 \pm 2°C$ $a_o = 6.202$ Å $b_o = 7.742$ $c_o = 8.100$	25,26,27
Theoretical density of 6.44 g/cm^3 at 28°C	Calculated from the above lattice parameters using average atomic weights of: Zn = 65.38 Sb = 121.76	
Melting point 546°C	Forms peritectically from a stoichiometric melt	21
Thermal conductivity at room temperature: Polycrystalline material: 1.3×10^{-2} watts/cm-°K 1.4×10^{-2} Single crystal: $3.0 \times 10^{-2} \dfrac{\text{watts}}{\text{cm-°K}}$	 Hole density of 1.3×10^{18} cm^{-3} Justi et al (1964) - unoriented - hole density of 2×10^{16} cm^{-3}	 9 4 9

(cont.)

Table 1.1 (cont.)

PROPERTY	COMMENTS	REF.
Energy Band Gap:		
<u>Thermal:</u>		
0.52 - 0.57 ev.	Kot and Kretsu (1960)	15
0.49 ev.	Eisner et al. (1961)	22
<u>Optical:</u>		
Room temperature:	Turner et al. (1961)	17
0.53 ev.	hole concentration =	
	4×10^{18} cm^{-3}	
0.48 ev.	Zavetova (1964)	23
	hole concentration =	
	3×10^{17} cm^{-3}	
0.50 $\pm$ 0.03 ev. (300°K)	Komiya, Masumoto and Fan (1964)	24
0.59 $\pm$ 0.03 (77°K)	room temperature hole	
0.61 $\pm$ 0.03 (42°K)	concentration of about 10^{16} cm^{-3}	
Conductivity type –		
p type as grown	Justi et al. (1964)	9
n-type material has		
never been produced.		
Ga and Te donor doping		
has been tried in single		
crystal material		

(cont.)

Table 1.1 (cont.)

PROPERTY	COMMENTS	REF.
Effective masses: $m_t/m_o = 0.146 \pm 0.010$ $m_\ell/m_o = 0.175 \pm 0.010$	Stevenson (1960) p-type ZnSb– cyclotron resonance at 1.5°K– only one resonance was observed. The type (charge sign) of the carrier responsible for the resonance was not determined.	16
Hole conduction properties: Observed maximum Hall mobilities near room temperature 575 $\dfrac{cm^2}{volt-sec}$	Kot and Kretsu (1960) $p \approx 5 \times 10^{16}$ cm^{-3} horizontal zone growth	15
500 $\dfrac{cm^2}{volt-sec}$	Eisner et al. (1961) $p \approx 3 \times 10^{16}$ cm^{-3} horizontal zone growth	22
580 $\dfrac{cm^2}{volt-sec}$	Justi et al. (1964) $p \approx 2 \times 10^{16}$ cm^{-3} horizontal zone growth	9

Table 1.1 (cont.)

PROPERTY	COMMENTS	REF.
Hall mobilities near room temperature (cont.)		
$10 \dfrac{cm^2}{volt\text{-}sec}$	Turner et al. (1961) $p \approx 4 \times 10^{18} \ cm^{-3}$ Czochralski growth	17
$300 \dfrac{cm^2}{volt\text{-}sec}$	Hruby et al. (1963) $p \approx 3 \times 10^{16} \ cm^{-3}$ Czochralski growth	11
$650 \dfrac{cm^2}{volt\text{-}sec}$	Komiya, Masumoto and Fan (1964) $p \approx 2 \times 10^{16}$ Czochralski growth	24
Anisotropy of Hall mobility $\mu_c > \mu_a > \mu_b$	Komiya et al. (1964) 77°K through 350°K	24
Thermoelectric power near room temperature 500 to 750 μV/°K	Anisotropy of thermoelectric power is not clearly established.	15,22,9 11,24
Magnetoresistance: Transverse effect is on the order of 5% in a 14.6 kg. magnetic field at 77°K	Justi et al. (1964) Anisotropies and field dependences of the magneto-resistance effect have not been determined.	9

potential of ZnSb single crystals.

To obtain these goals, the following body of experimental work was completed.

1.3.1 Materials Preparation

1.3.1.1 Single crystal growth

When this investigation began, in the Spring of 1963, zinc antimonide single crystals that were prepared by the horizontal zone recrystallization technique had significantly greater Hall mobilities than Czochralski grown material. Hence, the horizontal zone recrystallization technique was used to prepare large single crystals of ZnSb.

1.3.1.2 Control of carrier concentration

Zinc antimonide is p-type as grown. Silver, gold and copper are effective p-type doping agents. There is some evidence[32] that copper has the greatest solubility limit of the three in ZnSb. Hence, copper was used to control the hole concentration in ZnSb. Unsuccessful attempts were made to produce n-type ZnSb. Aluminum, selenium and indium were used as chemical dopants.

1.3.2 Investigation of Thermal Instabilities

It has been reported that the electronic transport properties of ZnSb change with time at temperatures that generally lie above 100 to 200°C. In order to apparently eliminate these changes, it is known that it is necessary to anneal ZnSb thermoelements at temperatures above the desired operating temperature. This instability appears both in polycrystalline and single crystal material. This instability has been recorded through annealing experiments on the single crystals that have been used in this investigation. A reasonable model has been advanced which qualitatively

accounts for the observed behavior.

1.3.3 Transport Measurements

The following measurements have been made on carefully oriented single crystal specimens of ZnSb. The degree of anisotropy was determined for each quantity.

1.3.3.1 Electrical conductivity

This was measured over the temperature range of 77 to 320°K on p-type crystals with several hole concentration levels that ranged from 2 x 10^{16} up to 1 x 10^{19} cm^{-3}.

1.3.3.2 Hall effect

This was measured under the same conditions as those outlined above for the electrical conductivity. The magnetic field dependence of the Hall effect was observed.

1.3.3.3 Magnetoresistance

This was extensively measured at 77°K (liquid nitrogen) on a lightly doped copper crystal (p $\simeq$ 4 x 10^{17} cm^{-3}). Some measurements were also made on undoped p-type single crystals. The magnetic field dependence of the magnetoresistance was observed.

1.3.3.4 Thermoelectric power

This was measured on p-type single crystals which had a variety of doping levels. Measurements were made at 0°C.

1.3.3.5 Thermal conductivity

This was measured on p-type single crystals which had a variety of doping levels. Measurements were made at 0°C.

1.4 THEORETICAL DEVELOPMENTS

Appendix 1 deals with macroscopic symmetry considerations in the D_{2h} point group. The zero elements of the phenomenological transport tensors are derived from crystal symmetry considerations. Elements up through those of 4th order in the magnetic field strength are considered.

Appendix 2 presents a theoretical derivation of the electronic transport coefficients of an energy band extremum that has the shape of a general ellipsoid. This derivation proceeds from a solution of the Boltzmann equation in the relaxation time approximation. The tensor relaxation time is assumed to have the same symmetry as the energy band extremum. The limit of low magnetic fields is assumed. Fermi-Dirac statistics are assumed. Analytical expressions are presented for the thermoelectric power, the electronic (hole) contribution to the thermal conductivity, the Lorentz numbers, the zero magnetic field electrical resistivity, the Hall coefficients and the magnetoresistance coefficients.

1.4 BIBLIOGRAPHY

1. Paul H. Egli, I.R.E. Trans. P.G.M.I.T., 6, 27 (1962).

2. Maria Telkes, J. Appl. Phys. 18, 1116 (1947).

3. Maria Telkes, J. Appl. Phys. 25, 765 (1954).

4. Maria Telkes, "Materials for Solar Thermoelectric Generators", Vol. 5, Transactions on the Conference on the Use of Solar Energy, Univ. of Ariz., Tucson, 1955.

5. E. Justi, Proceedings of the International Conference on Semiconductor Physics, Prague, 1960, p. 1074.

6. Justi and Schneider, Z. Naturforsch, 16a, 628 (1961).

7. Emeljanenko, Justi, Schneider, Z. Naturforsch, 16a, 1108 (1961).

8. Justi and Newman, U.S. Pat. 3,021,378, Feb., 13, 1962.

9. Justi, Rasch and Schneider, Adv. Energy Conv., 4, 27 (1964).

10. A. Hruby and J. Kasper, Czech. J. Phys. 12, 799 (1962).

11. Hruby, Berankova and Miskova, Phys. Status Sol. 3, 289 (1963).

12. Pilat, Chizh and Voityshen, Sov. Phys. Tech. Phys. 3, 734 (1958).

13. Pilat, Borodinets, Kosyachenko, and Maiko, Sov. Phys. Solid State 2, 1381 (1961).

14. Miksovsky, Simrous, and Toman, Proceedings of the International Conference on Semiconductor Physics, Prague, 1960, p. 1087.

15. Kot and Kretsu, Sov. Phys. Solid State 2, 1134 (1960).

16. M.J. Stevenson, Proceedings of the International Conference on Semiconductor Physics, Prague, 1960, p. 1083.

17. Turner, Fischler, and Reese, Phys. Rev., 121, 759 (1961).

18. Turner, Fischler, and Reese, J. Appl. Phys. 32, 2241 (1961).

19. Silvey, Lyons, and Silvestri, J. Electrochem. Soc. 108, 653 (1961).

20. C. Hirayama, J. Electrochem. Soc. 110, 80 (1963).

21. M. Hansen, Constitution of Binary Alloys, McGraw Hill, N.Y., 1958, p. 1185.

22. R.L. Eisner et al., J. Appl. Phys. 32, 1833 (1961).

23. M. Zavetova, Phys. Status Sol. $\underline{5}$, K19 (1964).

24. Komiya, Masumoto and Fan, Phys. Rev. $\underline{133}$, A1679 (1964).

25. F.L. Carter and R. Mazelsky, J. Phys. Chem. Solids, $\underline{25}$, 571 (1964).

26. K.E. Almin, Acta Chemica Scandinavia, $\underline{2}$, 400 (1948).

27. K. Toman, Phys. and Chem. of Solids, $\underline{16}$, 160 (1960).

28. Y.A. Ugai et al., Zh. Strukt. Khim. $\underline{4}$, 250 (1963).

29. Frost, Corelli and Balicki, Adv. Energy. Conv. $\underline{2}$, 77 (1962).

30. V.E. Khartsiev, Sov. Phys. Solid State, $\underline{4}$, 721 (1962).

31. V. Frei and B. Velitski, Sov. Phys. Solid State, $\underline{5}$, 706 (1963).

32. R. Mazelsky and R. Eisner, Scientific Paper 23-929-8902-P5, Westinghouse Research Laboratories, Pittsburgh, Pa., 1961.

CHAPTER 2

SINGLE CRYSTAL AND MEASUREMENT SAMPLE PREPARATION

2.1 INTRODUCTION

ZnSb forms by a peritectic reaction from a stoichiometric melt[1]. Hence, it is difficult, if not impossible, to prepare large single crystals by the usual crystal growing techniques. The binary phase diagram[1] indicates that single crystals should be grown from an antimony-rich melt which has its liquidus temperature between the peritectic temperature, 546°C, and the eutectic temperature, 505°C.

Kot and Kretsu[2] were the first to grow large single crystals of ZnSb. They used a horizontal zone recrystallization technique with an antimony rich molten zone. Eisner, Mazelsky and Tiller[3] independently used the same technique to produce large single crystals. Justi et al. have recently reported the growth of large ZnSb single crystals by this technique[4].

Another way to produce large ZnSb single crystals is to pull them (Czochralski technique) from an antimony rich melt. Turner et al.[5], Hruby et al.[6] and Komiya et al.[7] have produced large single crystals of ZnSb by the Czochralski technique.

At the time that this work was begun (Spring 1963), the horizontal zone recrystallization grown crystals had significantly higher Hall mobilities than the Czochralski grown material. Hence, the horizontal zone recrystallization technique was used to prepare the single crystals which were used in this investigation.

This chapter describes the preparation, doping, growth, etching, and mechanical cutting of ZnSb single crystals. Methods for making electrical and thermal contacts to this material are also discussed.

2.2 EXPERIMENTS WITH THE BRIDGMAN CRYSTAL GROWTH TECHNIQUE

Crystal growth was attempted in a Bridgman furnace[8] with the intent of producing ZnSb seed crystals. These seed crystals were to be used to nucleate melts in a horizontal zone recrystallization growth process. The peritectic horizontal[1] on the Zn-Sb phase diagram was avoided by the use of antimony rich melts that had zinc concentrations that varied from 44 to 46.3 atomic per cent.

The melts were prepared from 99.999% pure antimony and zinc[9] in a manner that parallels the method described in Section 2.3.1. The constituent elements were inserted into a 11 x 13 mm vycor tube which was then evacuated to about 5×10^{-6} Torr. at room temperature and sealed off. The vycor tube was not carbonized. The ampoule was then placed in a rocking furnace ($T \simeq 650°C$) and the contents reacted and mixed for 5 hours. The ampoule was water quenched and then placed into the Bridgman furnace for crystal growth.

The various growth ampoules were lowered through a temperature gradient of 50°C/inch at speeds that varied (between ampoules) from 0.10 to 0.033 inch/hour. The ingots were typically 4 to 6" long. The following observations are made on the basis of 7 samples that were successfully prepared in this manner.

No large single crystal regions were obtained. The maximum size of the single crystal regions was on the order of 1 x 0.3 x 0.3 cm. Freezing tended to take place from the walls of the vycor ampoule inwards. This was evidenced by the formation of relatively large single crystal formations at the surface of an ingot while the core portion was made up of many small crystals. The ingots were badly cracked. Etching with water diluted CP-4[10] and a microscopic examination of these cracks showed that many of them contained a thin

sheet of a substance which had the same etching characteristics as the eutectic alloy of antimony and zinc (~ 33 At.% Zn content). This etchant colors ZnSb black and leaves a clean surface on the eutectic alloy.

The above observations are compatible with, but do not necessarily prove, the following remarks. Evidently, the single crystal regions were limited in size because of incomplete mixing conditions in the melt. The enchancement of the concentration of antimony at the freezing interface (or interfaces) led to the premature formation of the eutectic alloy. This limited the size of the single crystal regions. Furthermore, this situation is aggrevated as more of the melt freezes, since the melt becomes richer in antimony as ZnSb is formed. Also, it is felt that many of the ingot cracks were caused by mechanical stresses that were developed by the anisotropic thermal expansion characteristics of the individual single crystal regions.

Attempts at the Bridgman growth of large ZnSb single crystals were abandoned when it was found that larger single crystal regions could be obtained with unseeded melts in the horizontal zone recrystallization furnace. No significant physical measurements were made on the Bridgman grown crystals.

2.3 GROWTH OF LARGE SINGLE CRYSTALS WITH A HORIZONTAL ZONE FURNACE

2.3.1 Raw Materials and Preparation of the Various Components of the Crystal Growth Charge

ASARCO[9] 99.999+% zinc rods and 99.999% antimony cast bars were used as starting materials. Quantitative analyses supplied by the producer indicated that copper and arsenic were the principle impurities in the antimony and copper and cadmium in the zinc. These materials were used without any further attempts at purification.

All materials were stored in an evacuated (~ 50 to 100μ) dessicator until needed for use. High purity, TransistAR grade[11], reagents were used

for all chemical treatments. TransistAR grade hydrochloric, nitric and acetic acids as well as acetone and methyl alcohol were available. Distilled and demineralized water was used when appropriate.

Materials were weighed to 0.1 mg. accuracy on a Mettler Model B-5 electronic balance.

Zinc was prepared for use by etching away several millimeters of the surface with hydrochloric acid. The resulting zinc slug was then rinsed 6 times in room temperature water. The zinc slug was then dried on filter paper in air in an 80°C furnace for about 30 seconds. The zinc slug was then weighed. The desired amount of antimony was calculated from the following formulas:

A. Stoichiometric charges (50 At.% Zn-50 At.% Sb)

(Weight Sb) = 1.8622 (Weight Zn)

B. Zone leveling charge

(Approx. 39.9 At.% Zn-60.1 At.% Sb)

(Weight Sb) = 2.8 (Weight Zn)

The antimony was broken up in a mortar with a stainless steel chisel. Large pieces of antimony which had freshly cleaved faces were used to make up the desired weight of antimony.

General Electric Co. type 204 clear fused quartz tubing was used to process the alloys as well as to make containment ampoules for final crystal growth. 13 x 15 mm dia. tubing was used to contain the alloys. After glass working, the quartz tubes were etched for 10 minutes with hydroflouric acid and water and then soaked in nitric acid for 1/2 hour. After several water and methyl alcohol rinses, the tubes were outgassed at 750 to 900°C for 18 to 36 hours under vacuum. Ultimate pressures were less than 1×10^{-6} Torr. The vacuum processing equipment is shown in Figure 2.1.
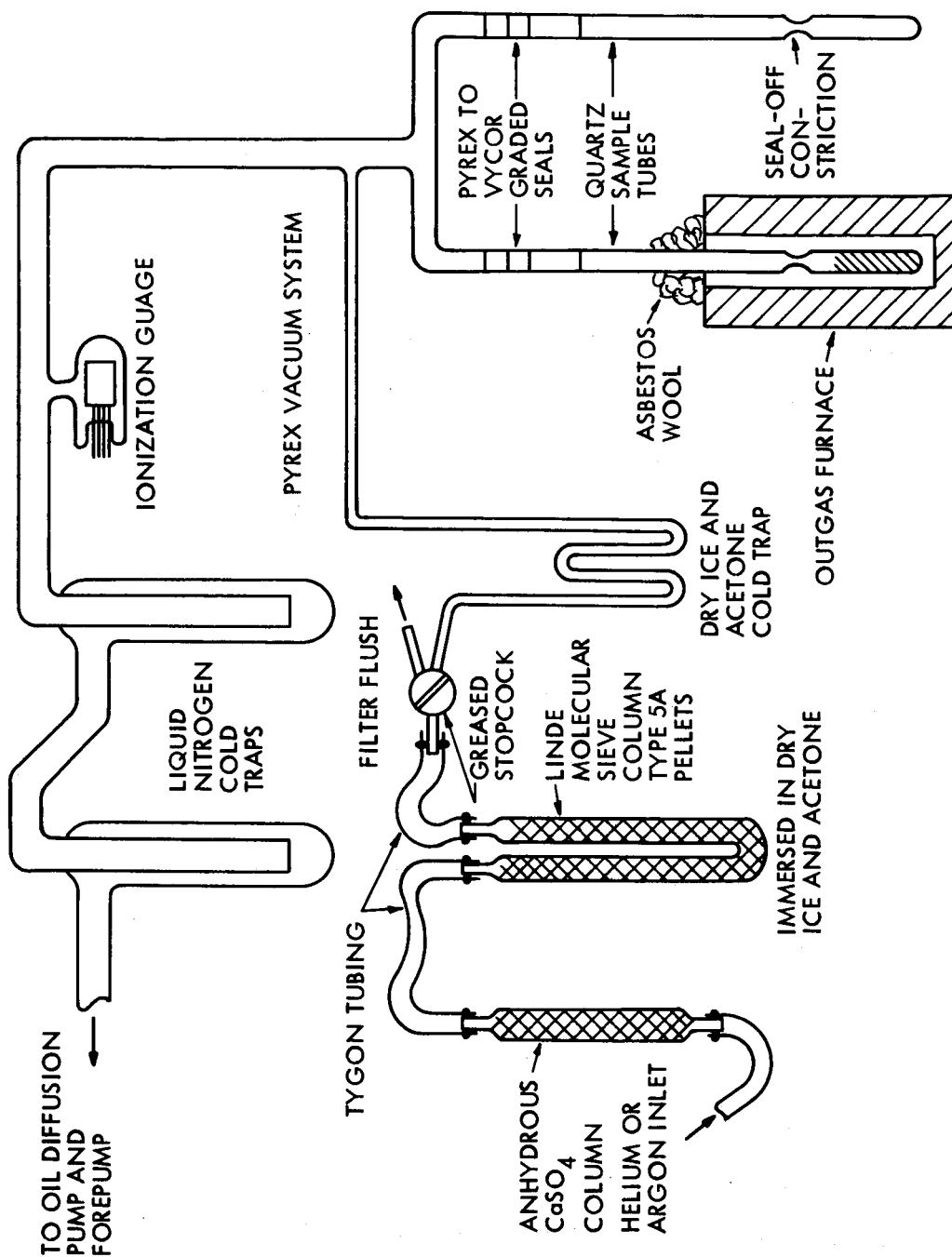
Fig. 2.1 Schematic Diagram of Vacuum Processing Equipment

After the proper amounts of antimony and zinc had been inserted and the tube evacuated, an outgas furnace was used to bake the tube and its contents at 125 to 175°C until the residual pressure dropped below 1×10^{-5} Torr. (usually 1 to 4 hours). Oil free helium was then admitted to the system and the quartz tube was constricted under one atmosphere pressure of helium. The alloy ampoule was then reevacuated and baked again as outlined above. The alloy ampoule was sealed off at a room temperature residual pressure which was less than 5×10^{-6} Torr.

The alloy (50-50 or 60-40) was then reacted in a rocking furnace for 4 to 6 hours at temperatures between 675 and 725°C. The molten alloy was water quenched. The ampoule was held horizontally for this operation. This gave long, thin bars which were of about the same cross section as the final crystal. The alloys showed no tendency to stick to the walls of the quartz ampoule.

2.3.2 Assembly of the Crystal Growth Charge

In the process of this investigation, 120 alloy charges were made up. The number of crystals grown was 80. The details involved in processing the several components of the crystal growth charge can be grouped roughly into two divisions:

A. Chemically etched components

B. Mechanically abraded components

All of the crystals upon which significant experimental data was obtained fall into the latter category. However, in order to clarify the decomposition problem - discussed in Section 2.3.5 - both types of surface treatments will be described.

Before continuing, it is of interest to note the geometry of the single crystal growth charge. This is shown in Figure 2.2. In essence the growth

APPROX. FULL SCALE SKETCH
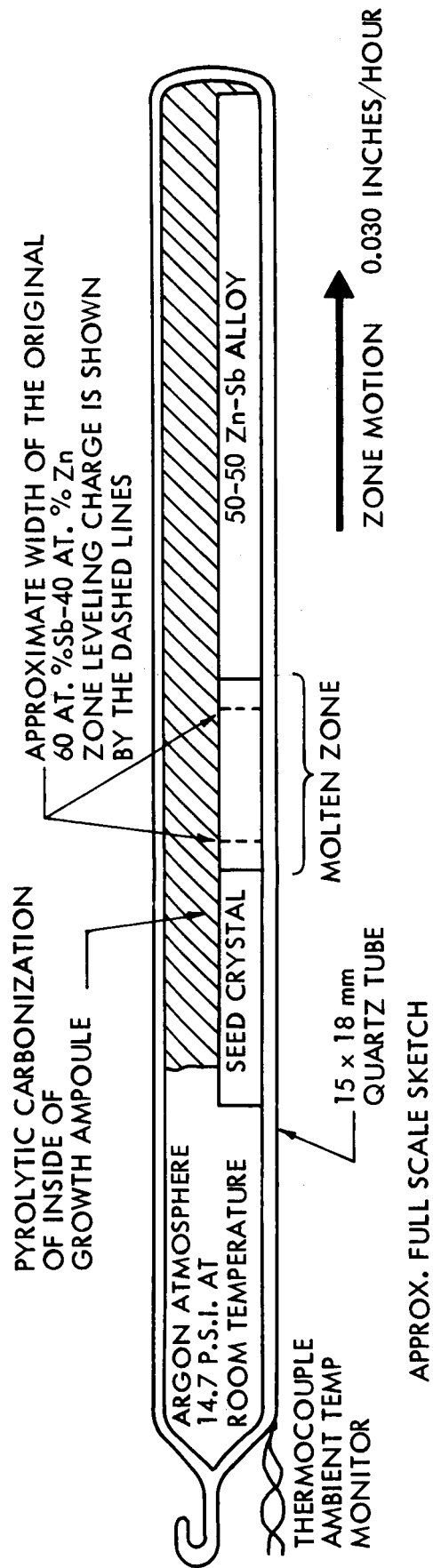
Fig. 2.2 Growth Ampoule For ZnSb Single Crystals

APPROX. 1/4 SCALE SKETCH
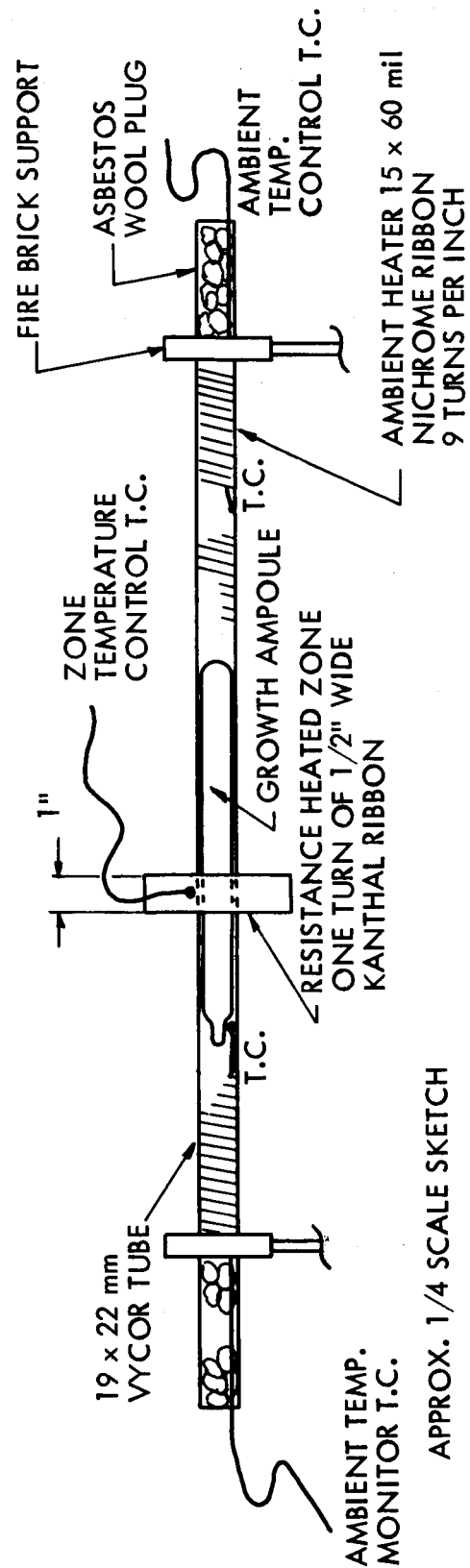
Fig. 2.3 Horizontal Zone Furnace Geometry

charge contains three components: a bulk stoichiometric charge, a zone level-ing charge and a seed crystal.

<u>2.3.2.1 Chemically etched component surfaces</u>

When preparing the growth charge for the earliest horizontal zone grown crystals, the surface of one, or more, of the three charge components was etched with:

<div align="center">

1 part HCl (36%)

1 part HNO_3 (70%)

1 to 8 parts CH_3COOH (glacial)

Rinse in HCl (36%) (1 second)

Rinse in distilled water.

All at room temperature.

</div>

A certain amount of success was obtained in growing a few large, mechanically sound ZnSb crystals. However, the above etch was not satisfactory in that it often formed grey films over all or part of the surface of the seed or an alloy charge. Quite often these films were not noticed until crystal growth had started. The appearance of these films was almost completely eliminated by substituting a room temperature rinse in:

<div align="center">

10 parts HBF_4 (50%)

1 part H_2O_2 (30%) rinse for 1 second

</div>

for the HCl rinse. However, when this was done, serious decomposition problems set in during the growth run. This decomposition was suppressed by adding an atmosphere of argon to the growth ampoule before sealing it. This point is discussed further in Section 2.3.5.

<u>2.3.2.2 Mechanically abraded component surfaces</u>

Consistently clean melts were obtained when the component surfaces were

cleaned, when necessary, by:

1. Rinsing in TransistAR purity grade acetone (bath 1).

2. Sandblasting all surfaces[16].

3. Soaking in acetone (bath 2).

4. Ultrasonically agitating the crystal or alloy slugs in acetone
   (bath 3).

5. Soaking in acetone (bath 4).

6. Drying on filter paper in a clean room.

Quite often, the water quenched alloy slugs were found to have very shiny and
clean surfaces when the carefully degreased (with trichloroethylene) quartz
ampoules were broken open in a clean room. In these cases, the alloy slugs
were used as is - with no further surface treatment. Single crystal components,
such as the seed crystal or a single crystalline bulk "50-50" charge (when
used), had to be surface treated as just outlined.

2.3.2.3 Preparation of the quartz growth ampoule

General Electric Co. type 204 clear fused quartz tubing (15 x 18 mm) was
used to make the crystal growth ampoules. After the chemical cleaning of the
worked quartz, the inside of the tube was rinsed with acetone. This acetone
was decomposed in an oxygen deficient atmosphere by heating the inverted tube
with a consumer gas - oxygen blowpipe flame. The pyrolytically decomposed
carbon surface film was then rinsed with more acetone while it was still hot.
This was repeated three times. The carbonized quartz tube was then outgassed -
under vacuum - at 750 to 900°C for 18 to 36 hours. Ultimate pressures were
less than 1×10^{-6} Torr.

2.3.2.4 Assembly and vacuum processing

The properly surface treated (Section 2.3.2.2) components of the crystal

growth charge were inserted into the outgassed, carbonized quartz tube in a clean room. The sample tube was then sealed back on to the vacuum system. The elapsed time of exposure to the atmosphere was 2 to 5 minutes for each component of the charge. The growth charge was outgassed, helium constricted, and outgassed again in the manner described in Section 2.3.1. After the final outgas cycle, argon[12] was flushed into the vacuum system and the growth ampoule was sealed off with an internal atmosphere of argon. The liquid nitrogen was removed from the two main vacuum system cold traps after the first argon was introduced into vacuum system. The argon was then flushed through the liquid nitrogen cold traps towards the pumps for 2 to 5 minutes. Figure 2.2 shows the growth ampoule.

2.3.3 Description of the Horizontal Zone Recrystallization Furnace

A sketch of the basic features of the horizontal zone recrystallization furnace is shown as Figure 2.3. The zone structure, itself consisted of a single turn of 1/2" wide Kanthal ribbon. This was encased in a firebrick and transite holder that cleared the ambient furnace tube by about one mm. The zone temperature control thermocouple was chromel – alumel and was inserted into a small diameter hole through the firebrick zone structure. It was cemented in place with the thermocouple bead viewing the back side of the Kanthal ribbon. A Minneapolis-Honeywell Pyrovane[13] controller was used to stablize the zone temperature. The a.c. output of a constant voltage transformer powdered the zone structure through a suitable impedance matching transformer. The estimated stability of the zone temperature control is $\pm$ 2°C.

A chromel – alumel thermocouple was also used to control the temperature of the ambient heater. It was cemented to the inside surface of the vycor ambient heater tube. A Minneapolis-Honeywell Electrovolt[14] controller was used to stablize the ambient temperature. It was used in conjunction with a magnetic

amplifier and saturable core reactor. The short term temperature stability of the ambient is estimated to be $\pm$ 1°C and the long term stability as $\pm$ 2°C.

The entire furnace was placed in a blocked-off fume hood to protect it from drafts. A d.c. motor drove a 20 threads/inch lead screw through a 1:6000 gear reduction to move the zone structure. A nominal growth rate of 0.030"/hr was used to produce the single crystals. This corresponds to a motor speed of 60 r.p.m. The motor was mounted independently of the zone furnace and fume hood. It drove the gear train through a nylon shaft and flexible couplings.

The temperature profile of the zone structure was determined by running a dummy sample through it. This sample was identical to a crystal sample except that aluminum oxide cement took the place of the zinc antimonide. Thermocouples were imbedded in the cement. By a measurement of this sort, the temperature gradient at the freezing interface is estimated to be about 75 to 100°C/inch and the maximum zone temperature about 580°C. The temperature gradient was measured for an ambient temperature of 415°C.

2.3.4 Single Crystal Growth Conditions

The use of an ambient heater with the zone furnace serves two purposes:

1. It helps to suppress crystal decomposition by keeping the residual vapor pressure of the volatile component (zinc) high.

2. In conjunction with the slow growth rate, the high ambient temperature subjects the as grown crystal to an annealing cycle. This tends to relieve strains and homogenize the distribution of impurities.

In summary, the crystal growth conditions were:

A. Argon atmosphere (14.7 p.s.i. at room temperature). Carbonized quartz ampoule walls.

B. Ambient heater temperature: 410 to 425°C-varying with the crystal.

C. Maximum zone temperature of about 580°C.

D. Crystal growth speed: 0.030 inch/hour.

E. Total zone travel of, typically, 15 cm in 200 hours.

To avoid thermal shock damage to the large single crystals, the zone furance was slowly cycled up to operating temperature before growth and back down to room temperature in the same manner (400°C were covered in 2 hours). This was accomplished by increasing or decreasing the a.c. input power with Variacs. This was done manually.

2.3.5 Decomposition During Growth and its Suppression

As the etching procedures (refer to Sections 2.3.2.1 and 2.3.2.2) were improved, a persistent and serious decomposition set in during crystal growth. This was especially noticed when alloy slugs were used without chemically etching their surfaces. This decomposition was evidenced by the condensation of considerable quantities of material on the cooler regions of the wall of the crystal growth ampoule. The recrystallized portion of the ingot would sometimes become severly warped and would actually curl up against the top of the growth ampoule. The resulting ingots were very polycrystalline, had poor mechanical strength, and had thermally etched surfaces. On the order of a gram of distillate (of a nominal total charge weight of 30 to 60 g.) condensed in the form of hundreds of small (0.1 to 2 mm dia.) droplets, which were fairly evenly distributed over the ampoule walls.

This extreme degree of decomposition was observed on seven crystal growth runs. Ambient temperatures were varied from 460 to 490°C in an attempt to stop this decomposition. The maximum zone temperature was on the order of 560 to 580°C. The nominal zinc content of the molten zone was varied between 40 to 46 At.%. Although all possible variations of these parameters were not

tried, the decomposition showed no sign of abating.

A quantitative ($\pm$ 1%) wet chemical analysis of samples of distillate from four decomposed crystals indicated the presence of both zinc and antimony with an average composition of 37 wt.% Zn and 63 wt.% Sb. This is a few percent to the zinc rich side of the ZnSb composition (34.9 wt.% Zn - 65.1 wt.% Sb).

It was found that this decomposition could be suppressed by backfilling the crystal growth ampoule with nitrogen or argon, at standard temperature and pressure, before sealing the ampoule from the vacuum system. Incandescent lamp grade argon[12] was used in preparing all of the crystals on which significant experimental data was obtained.

2.3.6 Preliminary Survey of Crystal Properties

The crystals described here were produced under the conditions outlined in Section 2.3.4. The horizontal zone recrystallized crystal ingots had a half-round cross section. They were typically 7 mm high, 13 mm wide and 10 to 15 cm long. The typical single crystal weighed 40 to 60 grams.

The crystal ingots had a good mechanical appearance. They were free of mechanical voids or inclusions. The free surface (during growth) of the crystal ingots occasionally displayed randomly scattered, scale-like patches. These occurred with a density of 2 to 20 per cm^2, were 0.1 to 1 mm in dia., had a convex cross section and typically extended 0.05 to 0.10 mm into the crystal. It is not known whether these patches are collections of decomposition products or collections oxidation products. Laue back reflection x-ray photographs of the single crystal region next to a mottled surface did not reveal any straining or low angle grain boundary formation which might be caused by these patches.

The crystal growth axis was within several degrees of the <001> direction for some of the crystals used in the thermal measurements. The majority of the crystals used for galvanomagnetic and thermal experiments were grown in the <316> direction.

All crystals were oriented with Laue back reflection x-ray photographs. The crystal axes are identified as follows:[15]

$$<100> = a = 1 = 6.20\overset{o}{A}$$
$$<010> = b = 2 = 7.74\overset{o}{A}$$
$$<001> = c = 3 = 8.10\overset{o}{A}$$

Low angle grain boundaries - on the order of 0.1° - could be visually detected on a sandblasted[16] crystal surface. Their presence was confirmed with the back reflection x-ray camera. Crystals grown in uncarbonized quartz ampoules had a definite tendency to form low angle grain boundaries. Three to ten would typically occur in an ingot. The frequency of occurrance of these low angle grain boundaries was greatly reduced by carbonizing the ampoule walls. The low angle grain boundaries tended to line up parallel to the c-axis of the crystal.

The fact that ZnSb was actually being produced was confirmed with a Debye-Scherrer powder camera x-ray photograph and by a quantitative wet chemical analysis ($\pm$ 1%) of two different crystals.

After sandblasting all surfaces, longitudinal profiles of electrical resistivity and thermoelectric power were taken with a four point probe and a hot probe. The resistivity and thermoelectric power was usually uniform to within at least $\pm$ 5% over the first 50 to 75% of the length of the ingot.

2.3.7 Degree of Crystal Perfection

Photomicrographs of etched surfaces and Laue back reflection x-ray photographs can be used to estimate the degree of perfection of a crystal surface. Illustrations of two relative extremes will be presented here.

The first set of illustrations, Figures 2.4, 2.5 and 2.6, were taken approximately on a (001) plane of crystal C-1061-A. This crystal was grown in an uncarbonized quartz ampoule. The crystal wafer was carefully final-polished with Linde B powder. It was etched, at room temperature for one minute, in 1 part HCl (36%), 1 part HNO_3 (70%), 8 parts CH_3COOH (glacial); rinsed in 10 parts HBF_4 (50%) and 1 part H_2O_2 (30%) for 1 second and then rinsed in water. The nature of the etch pit patterns did not change with repeated repolishing and re-etching. It is assumed that each individual etch pit corresponds to one edge dislocation in the bulk of the crystal. The photomicrographs, Figures 2.4 and 2.5, show how the dislocations tend to lie in the (100) and (010) planes of the crystal. Some of the linear dislocation arrays contain such a large number of dislocations, that they seem to form low angle grain boundaries. The Laue back reflection photograph, Figure 2.6, indicates that this crystal is actually a mosaic structure, made up of small single crystals regions. The fine structure pattern of the individual x-ray reflection spots indicates this. It should be noted that this severe degree of mosaic structure was not typical of all of the crystals which were grown in uncarbonized quartz ampoules. Some crystals had regions with much cleaner back reflection x-ray photographs. No physical measurements were made on crystal C-1061-A. Crystal C-1061-A was not doped.

Figures 2.7 and 2.8 present similarly observed results for the undoped crystal which was used in galvanomagnetic and thermal measurements, C-1081-C.
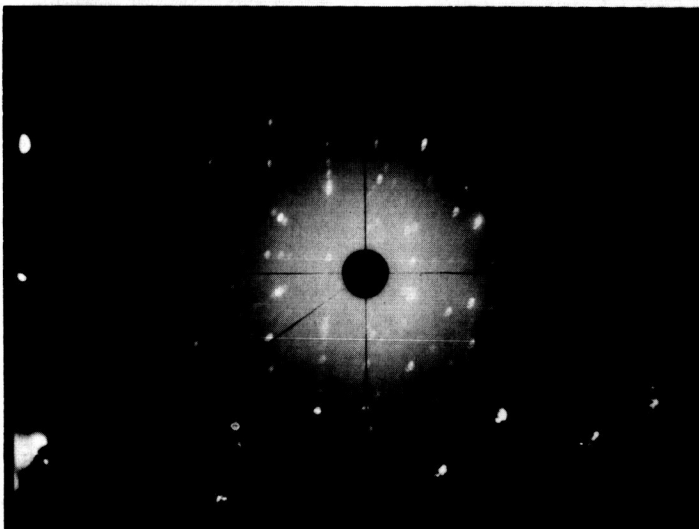
APPROX. ORIENTATION

$\langle 100 \rangle$ $\langle 010 \rangle$

Fig. 2.6   Laue Back Reflection X-Ray Difraction Photograph of the Surface of Fig. 2.4
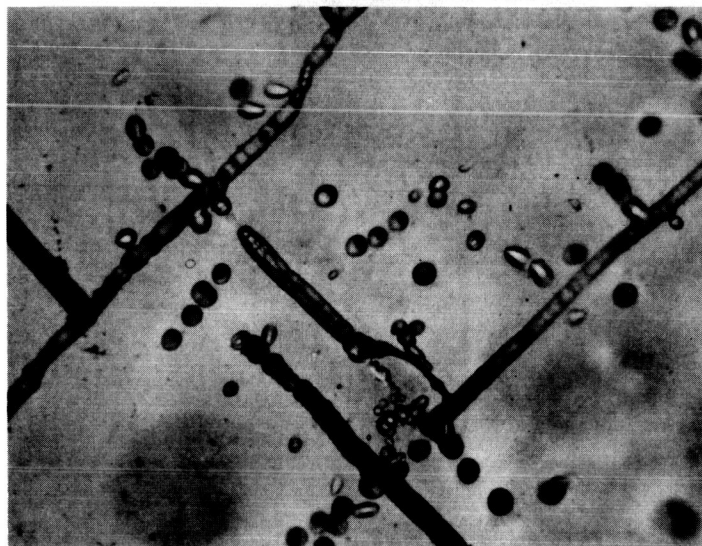
CRYSTAL   C-1061-A

500 X MAGNIFICATION

$\langle 100 \rangle$ $\langle 010 \rangle$

Fig. 2.5   Photomicrograph of an Etched (001) Surface

CRYSTAL   C-1061-A

100 X MAGNIFICATION

$\langle 100 \rangle$ $\langle 010 \rangle$

Fig. 2.4   Photomicrograph of an Etched (001) Surface

<010> <100>
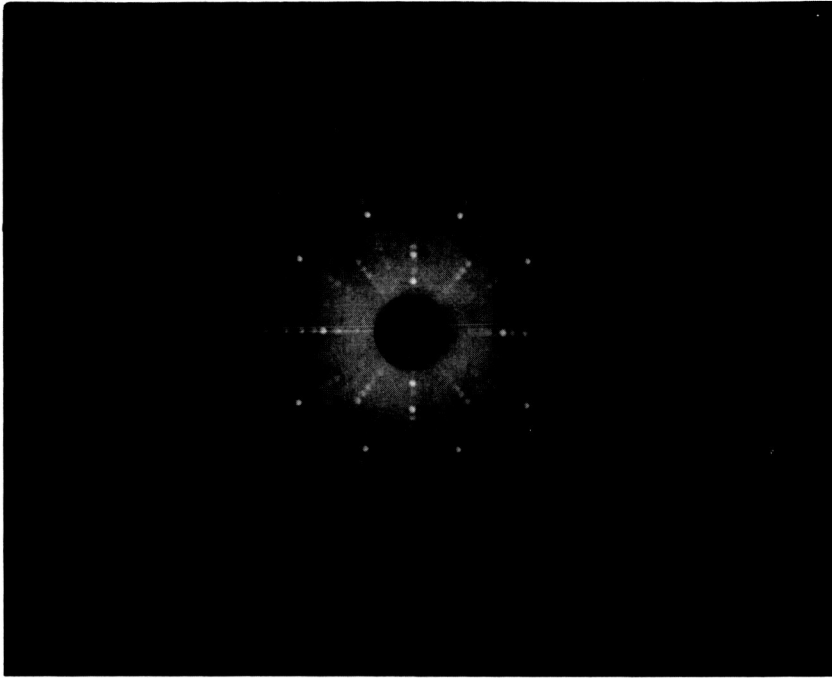
Fig. 2.8 Laue Back Reflection
X-Ray Photograph of
the Surface of Fig. 2.7
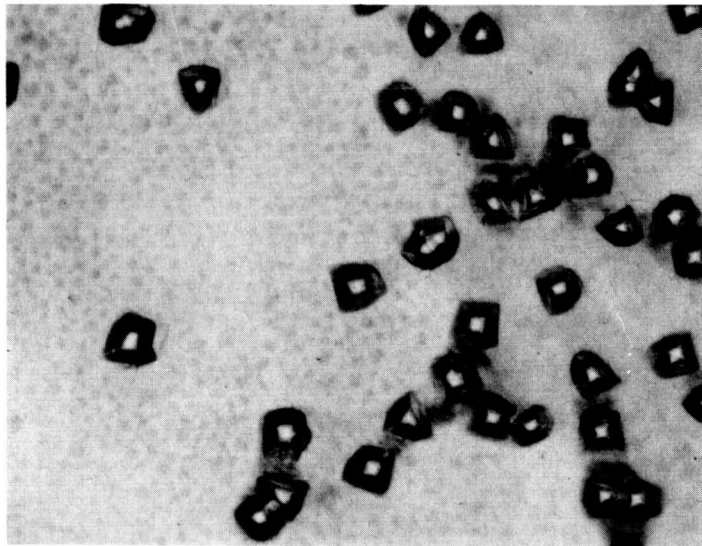
CRYSTAL C-1081-C
500 X MAGNIFICATION

<010> <100>

Fig. 2.7 Photomicrograph
of an Etched
(001) Surface

This crystal was grown in the <316> direction in a carbonized quartz ampoule. It is seen that the density of dislocations has been reduced. The etch pits are randomly scattered. The back reflection x-ray photograph has well defined reflections. This photograph was taken on a camera which had a beam collimator which was half the diameter of that of the camera used to obtain Figure 2.6. The etch pits shown in Figure 2.7 differ from the preceding in that they are approximately rhombohedral in shape. This is becasue this surface was etched differently from the preceding. An etch recommended by Hruby[17] was used. It consisted of 8 parts glycerol, 6 parts H_2O_2 (30%) and 3 parts HF (48%). It was used at room temperature. The crystal was etched for about 1 minute and rinsed in room temperature water. Similar etch pit figures (and comparible etch pit densities) were observed on crystal C-1078-C ($p \sim 4 \times 10^{17}$ copper doped) and C-1115-A ($p \sim 1 \times 10^{19}$ copper doped). Etch pit densities and distributions similar to that illustrated by Figure 2.7, were also obtained when the above described aqua regia etch was used.

2.4 CONTROL OF ELECTRICAL CARRIER CONCENTRATION

Undoped crystals were p-type as grown. Hole concentrations were on the order of 2×10^{16} cm^{-3}.

2.4.1 Acceptor Dopant

Copper was used as an acceptor dopant. The dopant was introduced by including a measured amount of a Cu-Sb alloy with the antimony which was used to make up a nominally 60 At.%Sb-40 At.%Zn zone leveling charge. For very heavily doped samples, small pieces of copper (99.999% purity) were directly added to the 60-40 charge before its encapsulation. No copper was added to the bulk alloy charge which was of stoichiometric (50-50) composition. The copper was then incorporated (from the molten zone) into the crystal during the normal crystal growth process.

This procedure will give a fairly uniform doping level over the length of a newly grown crystal if:

1. The portion of the crystal of interest (for experimentation) is small compared to the size of the molten zone.

2. The distribution coefficient[18] of the impurity atom is much less than unity.

Both conditions were met with the copper doped crystals used in this investigation. The molten zone length was about 3 cm long while the total length of the grown crystal was 8 to 15 cm. Only one or two centimeters of this was needed for any one set of experimental measurements. From Table 2.1 presented in the next section, the distribution coefficient (the ratio of the impurity concentration in the solid to its concentration in the melt) of copper in ZnSb can be estimated as being about $1/15 = 0.067$.

2.4.2 Donor Dopants

Justi et al.[4] have tried to produce n-type ZnSb by chemical doping with Te and Ga. They were unsuccessful. Al, Se and In were tried as donor dopants in the present work. These were introduced into the growth process in exactly the same way as copper in the above described copper doping process. Crystals were grown with molten zones containing approximately the following number densities of impurity atoms:

$$\text{Aluminum:} \quad 3 \times 10^{18} \text{ impurity atoms/cm}^3$$
$$4 \times 10^{19}$$
$$\text{Selenium:} \quad 5 \times 10^{18}$$
$$6 \times 10^{19}$$
$$\text{Indium:} \quad 8 \times 10^{19}$$

In all cases, the crystals showed p-type electrical conduction. This was determined at room temperature by measuring the thermoelectric power with

a hot probe.

2.5   SUMMARY OF PROPERTIES OF CRYSTALS USED FOR MEASUREMENTS

The basic differences in the electrical characteristics of the crystals used in the measurement phases this investigation are summarized in Table 2.1. Copper was used to control the hole concentrations in the doped crystals.

2.6   PREPARATION OF MEASUREMENT SAMPLES

2.6.1   Crystal Orientation and Cutting

Crystals were oriented with Laue back reflection x-ray photographs. On the basis of many orientation checks before and after cutting, the orientation and cutting procedures were found to be accurate within ± 2 degrees.

The single crystals were found to be far too brittle to be cut reliably with available diamond cut off wheels. Consequently, spark erosion cutting[19] was used to section the crystals and shape all surfaces of the measurement samples. 20 mil dia. and 5 mil dia. tungsten wires were used as cutting electrodes. The cuts were made under deodorized kerosene with working voltages of 30 to 40 volts and short circuit currents of about 20 ma. The cutting speed was set at about 1 cm/hr. Faster cutting speeds tended to produce thermally generated cracks in the crystal – especially in the higher resistivity crystals. The resulting surfaces were found to be very uniformly cut. Some surface damage (or deposits) was present, but this was removed by eroding away about 10 microns of the surface with an air brasive cutter.[16]

These sandblasted surfaces contained, of course, a damaged layer. The major portion of this damage was confined to the first 7 to 10 microns of the surface. This was determined by back reflection x-ray photographs. A sandblasted crystal surface generally had well defined x-ray reflection spots, but often faint, very diffuse spots and blotches also would appear. These

TABLE 2.1

SUMMARY OF PROPERTIES OF CRYSTALS USED FOR MEASUREMENTS

Crystal Number	Measurements Made	Doping Level in Molten Zone ± 20% (cm^{-3})	Resultant Measured Hole Concentration in Crystal at Room Temperature* (cm^{-3})	Approximate Room Temperature Electrical Resistivities (Ω-cm)	Measured Thermoelectric Power at 0°C ($\mu V/°K$)	Carbonized Walls on Growth Ampoule**
C-1081-C	Thermal & Galvanomagnetic	none	2×10^{16}	0.5	700	yes**
C-1078-C	" "	6×10^{18}	4×10^{17}	0.03	427	yes**
C-1073-B	" "	1.3×10^{19}	8×10^{17}	0.02	400	yes
C-1082-A	Thermal	1.5×10^{19}		0.01	346	no
C-1117-A	Thermal	5.5×10^{19}		0.003	250	yes**
C-1075-B	Thermal & Galvanomagnetic	1.5×10^{20}	1×10^{19}	0.001	175	no**
C-1115-A	Thermal	2.4×10^{20}		0.001	170	yes
C-1117-B	Thermal	1.3×10^{21}			100***	yes

*Hole concentration, $p \sim 1/Rq$, where R is the Hall coefficient and $q = 1.6 \times 10^{-19}$ coulomb.

**Undoped single crystals were used as the bulk, stoichiometric charge in the growth of these crystals.

***This measurement was made at room temperature with a hot probe. No further measurements were made on this crystal.

were absent from x-ray photographs of chemically etched surfaces.

2.6.2 Galvanomagnetic Samples

The typical galvanomagnetic sample geometry is shown as Figure 2.9. An effort was made to keep the (length to width) aspect ratio of the samples at least as high as 8 or 10. This was done to minimize the effects of the inhomogeneous electric current distribution in the vicinity of the current contacts. This precaution also minimized the disturbance of the magneto-resistance measurement which was introduced by the finite size of the voltage probe contacts. Because of crystal geometry, the <100> axis samples had a maximum length of 8 mm and had to be used with an aspect ratio of about 6 to 8. The samples which were used to carefully measure the degree of anisotropy in the Hall effect had transverse dimensions approaching 1.5 mm. These dimensions were increased to reduce the measurement perturbations introduced by the finite contact areas of the Hall probes.

2.6.3 Electrical Contacts

It was found that ordinary (60-40) lead-tin solder, applied with a rosin flux, wet zinc antimonide very well and produced excellent ohmic contacts.

Over a hundred contacts were specifically tested for ohmic behavior at room temperature and at 77.3°K. Contact current densities reached as high as 50 A/cm^2. No nonlinearity was ever observed.

Fine copper wires were soldered to the galvanomagnetic samples with a hot gas jet. A bit of rosin flux was applied to the freshly sandblasted surface of a sample bar. A pretinned copper wire, with a small solder bead at the end, was then positioned with a micromanipulator and butted against the surface. A second micromanipulator was then used to position the 15 mil dia. nozzle of a homemade, vycor enclosed, resistance heated gas jet

1.5 mil DIA.
COPPER WIRE
VOLTAGE PROBES

50-50 Pb-Sn
SOLDER DOTS

3.0 mil DIA. COPPER
WIRE CURRENT LEADS

D   C

h

G   A   t

F   B

L_E L_V L_E

LENGTH
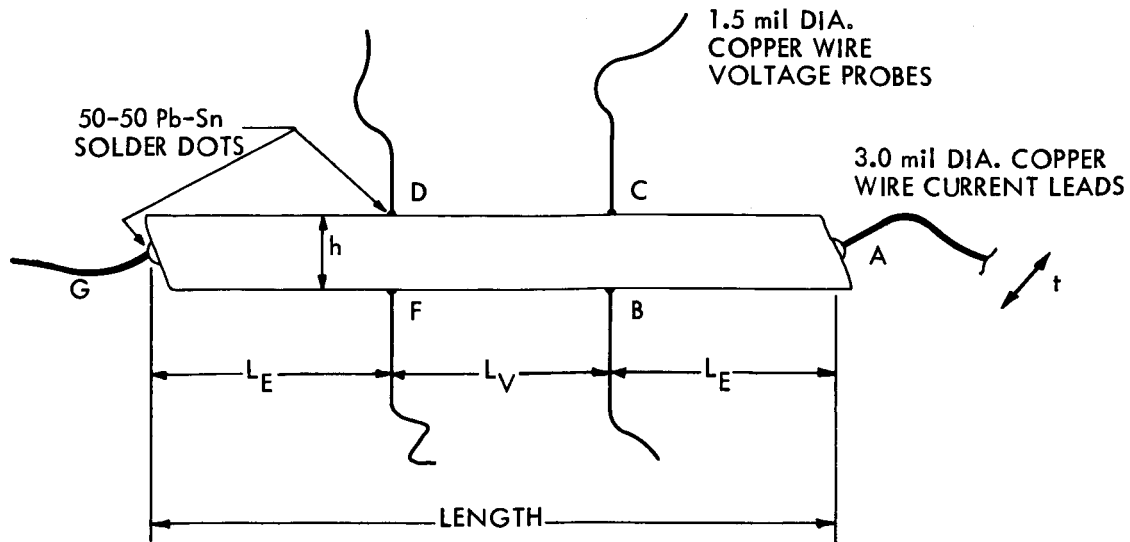
CURRENT CONNECTIONS AT LEADS A-G

RESISTIVITY MEASUREMENT AT LEADS B-F

HALL VOLTAGE MEASUREMENT AT LEADS C-B AND D-F

DIAMETERS OF SOLDER DOTS AT ELECTRICAL CONTACTS
TYPICALLY: 0.3 mm FOR CURRENT CONTACTS A-G
0.08 TO 0.10 mm FOR VOLTAGE PROBES

TYPICAL SAMPLE DIMENSIONS:

1. ELECTRICAL CURRENT ALONG <010> OR <001>

LENGTH = 9 TO 11 mm L_V = 3 mm

h = 1.2 mm L_E = 3 TO 4 mm

t = 1.0 mm

2. ELECTRICAL CURRENT ALONG <100>

LENGTH = 6 TO 8 mm L_V = 2 mm

h = 1.2 mm L_E = 2 TO 4 mm

t = 1.0 mm

3. ELECTRICAL CURRENT AT 45° TO A PRINCIPAL
CRYSTAL AXIS:

DIMENSIONS ARE IN BETWEEN THOSE
OF 1. and 2. ABOVE

Fig. 2.9   Galvanomagnetic Sample Geometry

heater. The fine jet of heated gas ($\sim$190°C) was then turned on and the bond made in 3 to 5 seconds. Either nitrogen or forming gas was used.

Voltage probes had contact diameters of about 0.1 mm. Current contacts had diameters of about 0.3 mm. The current contacts were not made with a larger area because of potentially dangerous, differential thermal expansion stress generation when the samples were cooled to 77.3°K.

2.6.4 Galvanomagnetic Sample Surfaces

In order to avoid carrier accumulation at the sample surfaces, the surface recombination velocity was increased by using sandblasted sample surfaces[20,22]. The use of chemically etched surfaces is noted in the text when such a case occurs in the measurements.

2.6.5 Thermal Samples

Thermal measurement samples, used for thermoelectric power and thermal conductivity measurements, were approximately cube shaped and measured 3 to 5 mm on a side. The cubes were cut so that they were bounded by the 3 principal crystallographic planes.

2.6.6 Thermal Contacts

The thermal conductivity measurement required large area contacts which were made to a brittle material which has an anisotropic thermal expansion[23].

A low temperature soldering technique was used. This minimized mechanical straining and crystal breakage due to differential thermal expansion between any two principle axes and the copper heat source or sink.

Two opposite faces of the thermal conductivity sample were sandblasted[16] and carefully plated with indium from a room temperature bath of indium sulfamate plating solution[21]. The copper heat source and sink of the thermal conductivity chamber (Section 3.2.2 and Figure 3.6) were tinned with gallium.

The ZnSb crystal was then raised to slightly above room temperature (to about 30°C) and the indium plated faces tinned with gallium. The crystal was then placed in contact with the heat source and heat sink and the whole assembly was cooled to about 15°C where the supercooled gallium solder froze. Thermal measurements were made at 0°C. Hence, only about a 15-20°C maximum temperature excursion was experienced by the solid gallium solder contacts.

This soldering technique also has the advantage that the crystal sample can be easily unsoldered, cleaned, and remounted with a different crystallographic orientation. It was often possible to run complete sets of thermal measurements on all three sets of faces of a given cube.

These indium plated and gallium soldered contacts were found to be ohmic up to the highest tested current level, which was 0.5 A/cm^2. For a further discussion of electrical contact resistance, refer to Section 3.2.2.

The measured thermal conductivities were found to be independent of sample length. Hence, the thermal resistance of the contacts was negligible also.

2.7 BIBLIOGRAPHY AND REFERENCES

1. M. Hansen, Constitution of Binary Alloys, p. 1184, McGraw Hill Inc.,
    New York, N.Y., 1958.

2. M.V. Kot and I.V. Kretsu, Sov. Phys. Solid State, $\underline{2}$, 1134 (1960).

3. Eisner, Mazelsky and Tiller, J. Appl. Phys., $\underline{32}$, 1833 (1961).

4. Justi, Rasch and Schneider, Adv. Energy Conv., $\underline{4}$, 27 (1964).

5. Turner, Fischler and Reese, Phys. Rev., $\underline{121}$, 759 (1961).

6. Hruby, Berankova and Miskova, Phys. Status Sol., $\underline{3}$, 289 (1963).

7. Komiya, Masumoto and Fan, Phys. Rev., $\underline{133}$, A1679 (1964).

8. W.D. Lawson and S. Nielsen, Preparation of Single Crystals, p. 14,
    Academic Press, Inc., New York, N.Y., (1958).

9. Zinc and Antimony obtained in bar and rod form from American Smelting
    and Refining Co., Central Research Laboratories, South Plainfield, N.J.

10. H.C. Gatos and M.C. Lavine, Chemical Behavior of Semiconductors: Etching
    Characteristics, Technical Report # 293, M.I.T. Lincoln Laboratory,
    Lexington, Mass., January 2, 1963.

11. TransistAR grade chemicals manufactured by the Mallinckrodt
    Chemical Works, New York, New York.

12. Incandescent lamp grade argon was generally used: Air Reduction Company
    99.8% argon, 0.2% N_2.

13. Mineapolis-Honeywell Pyrovane controller, model 105C4-P5-25.

14. Minneapolis-Honeywell Electrovolt Controller, model Y153R(11)-VG-(147)-
    K1-(27).

15. F.L. Carter and R. Mazelsky, J. Phys. Chem. Solids, $\underline{25}$, 571 (1964).

16. S.S. White Co., 10 East 40th St., New York 16, N.Y.; model C Industrial
    Airbrasive unit used with #1 powder-27 micron aluminum oxide.

17. A. Hruby and J. Kaspar, Czech. J. Phys. $\underline{12}$, 799 (1962).

18. W.G. Pfann, Zone Melting, p. 2., John Wiley & Sons, Inc., N.Y., (1958).

19. H.H. Ehlers and D.F. Kolesar, Specimen Preparation by Spark - Erosion
    Cutting, Technical Report #303, M.I.T. Lincoln Laboratory, Lexington,
    Mass., 14 March 1963.

20. E.H. Putley, the Hall Effect and Related Phenomena, Section 4.14, Butterworth, London, 1960.

21. Indium Sulfamate plating solution, Indium Corporation of America, 1676 Lincoln Avenue, Utica, New York.

22. A.C. Beer, Galvanomagnetic Effects in Semiconductors, p. 61, Academic Press, New York, N.Y., 1963.

23. R.Z. Bachrach, Measurement of the Principal Thermal Expansion Coefficients of Zinc Antimonide, S.B. thesis, Department of Physics, M.I.T., Cambridge, Mass., June 1964.

CHAPTER 3

MEASUREMENT INSTRUMENTATION

3.1 GALVANOMAGNETIC MEASUREMENTS

3.1.1 Introduction

Galvanomagnetic measurements should be made on isothermal samples. This eliminates thermal and thermomagnetic contributions to experimentally measured sample voltages. These points and methods for minimizing their influence have been discussed by many authors[1-3].

An a.c. measurement system was used in this investigation. A a.c. sample current, a d.c. magnetic field, and a frequency selective a.c. detection system were used. The use of frequencies above roughly ten cps. effectively eliminated the influence of both the Peltier heat generation at the current contacts and the Ettingshausen effect. Reasonable care in heat sinking the measurement sample and in using small sample currents minimized the influence of nonuniform Joule heating.

3.1.2 Galvanomagnetic Measurement Instrumentation

Figure 3.1 presents a block diagram of the instrumentation scheme. This figure is largely self explanatory. The primary a.c. signal source was the Hewlett-Packard model 200 CD audio oscillator. The frequency of operation was generally in the range of 150 to 230 cps - although frequencies as low as 18 cps were used on occasion. One of the Hewlett-Packard model 400 D VTVM's was carefully calibrated. It served as the secondary voltage reference for calibrating the measurement system by means of a precision resistance voltage divider. The other VTVM, connected in parallel with the first, reduced the possibility of a sudden VTVM malfunction spoiling a measurement run.
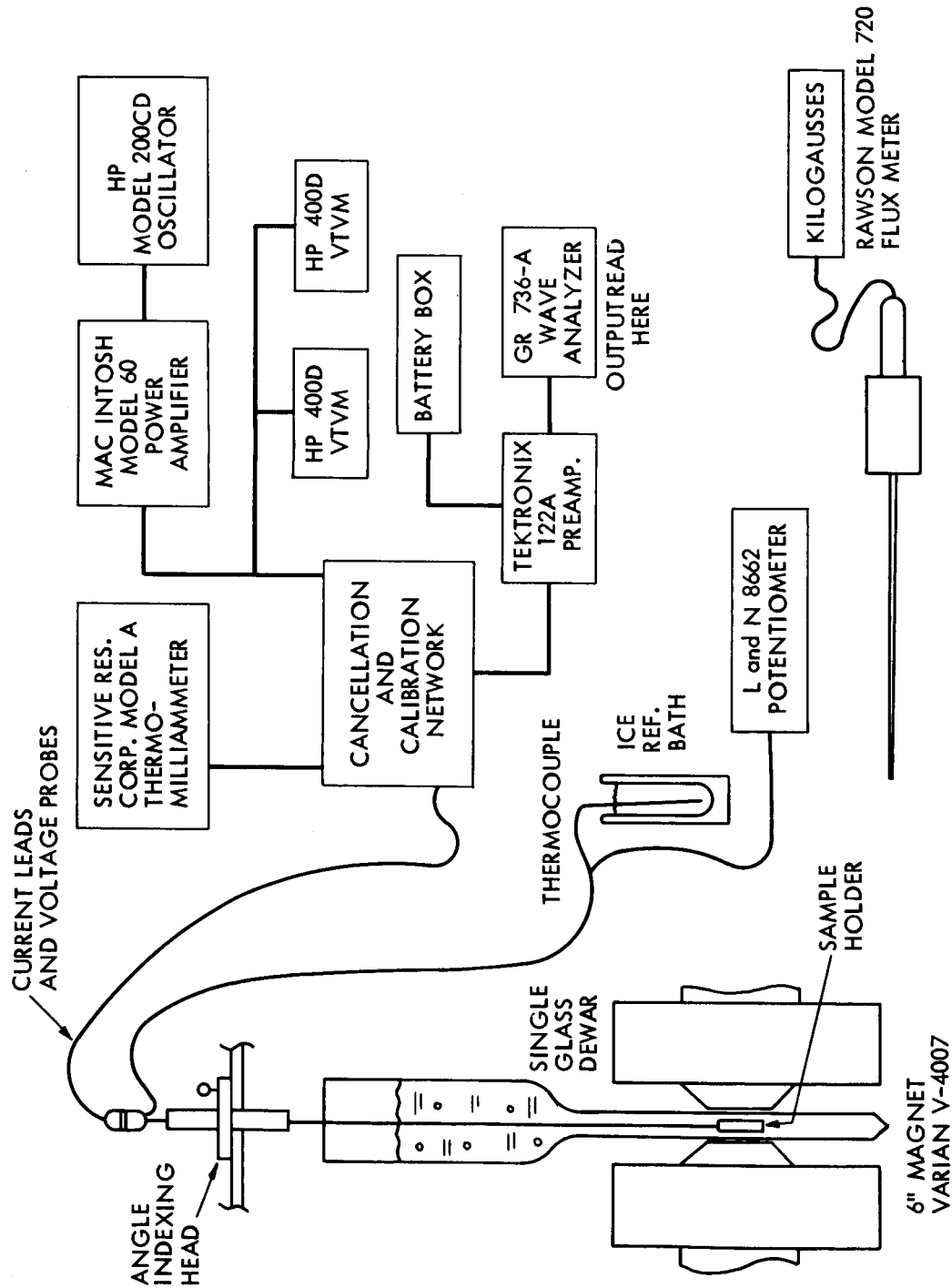
Fig. 3.1 Block Diagram of the Galvanomagnetic Instrumentation

The cancellation network is a simple R-C phase and amplitude shifting circuit, shown in Figure 3.2. It was used to provide a cancellation signal to null out the extraneous IR sample voltage picked up by misaligned Hall probes. This circuit was also used to null out the zero magnetic field IR voltage picked up by the sample voltage probes. When the magnetic field was then applied, the resulting measured voltage could be used directly to yield the magnetoresistance voltage, $\Delta V/V^\circ$. This voltage is equal to $\Delta\rho/\rho^\circ$ if the sample current remains constant when the magnetic field is applied. This is true here since the current limiting resistor, R_S, was 30 to 100 times higher than the sample resistance and also since $\Delta\rho/\rho^\circ$ was generally less than $\sim$ 1%.

R_S could be chosen from any one of seven resistance values in the range of 5 to 1000 ohms by a built in selector switch. The same is true of C_P and C_S - values from 0.001 through 1.0 μf could be selected by built-in switches. By deriving the cancellation voltage directly from the sample current, small amplitude and frequency fluctuations in the output of the audio oscillator-power amplifier excitation source did not have a first order effect on the stability of the voltage null.

IR sample voltage could be routinely nulled to 1 part in 10^6. The phase and amplitude adjustment potentiometers were 10 turn helipots. The cancellation network could be switched out to give a direct measurement of sample resistivity. The calibration network could be switched in and out within a few seconds to give a system calibration check at anytime. System calibration was checked often during a data taking run.

The Tektronix type 122-A low level preamplifier was battery operated. Its adjustable upper and lower half-power points were usually set at 80 and 250 cps respectively. The skirts on the passband fell off with a
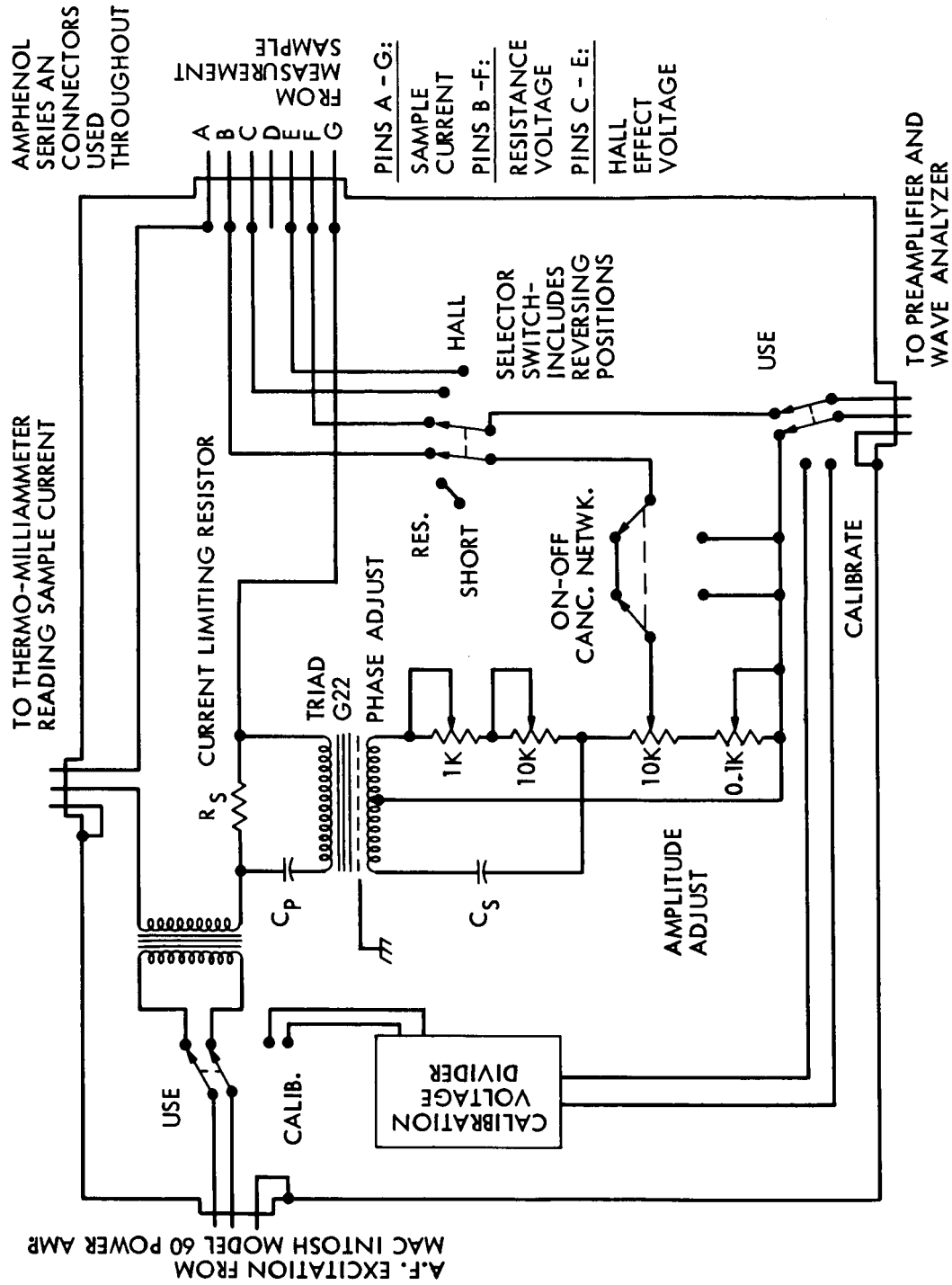
Fig. 3.2   Schematic Diagram of Voltage Cancellation and Calibration Network

limiting assymptote of 20 db/decade. Negligible distortion was introduced by this preamplifier for input voltages less than 5 mv with 1000 x gain and 50 mv with 100 x gain. The input impedance of this preamplifier was 10 megohms in parallel with 50 pf.

A General Radio Co. type 736-A wave analyzer was used as a tuned volt-meter. The 3 db width of the passband is rated as 6 cps and the passband width is rated as being about 30 cps at 40 db down. The top 80% of the meter deflection was found to be linear within 1%. The calibrated attenuators in this instrument were carefully checked for proper scaling. Full scale voltages of 0.3 μV to 100 mv could be quickly and accurately chosen by switching these internal attenuators.

The entire measurement system was carefully shielded. Ground loops were assiduously avoided. The frame of the Varian Associates electro-magnet was used as a common ground point. With a measurement sample in place, the residual 60 cps signal in the measurement system (wave analyzer tuned to 60 cps) was less than 5 μV.

The Sensitive Research Corporation Model A thermo-milliammeter was carefully calibrated against a 10.007 $\pm$ 0.05 Int.-ohm oil immersed precision resistor with a Leeds and Northrup type K potentiometer. The standard cell used was cross checked against several others to confirm its emf.

One test of the operation of the entire measurement system involved the measurement of known resistances in the range of 0.1 to 10Ω. These test resistances were mounted in the actual sample holders and could be con-sistently measured to within 1% over the frequency range of 20 to 300 cps.

The Rawson, Model 720 rotating coil fluxmeter was calibrated against a Varian Associates model F-8A nuclear magnetic resonance fluxmeter. No

calibration corrections had to be applied to the fluxmeter readings. It was limited to 1/2% absolute accuracy by reading precision only.

Three inch dia. tapered pole pieces were used on the 6" electromagnet - Varian Associates model V-4007. The pole spacing was 1-1/8". The magnetic field was measured to be homogeneous to within 1/2% over a diameter of 1-1/2 inches. The largest experimental sample dimension was less than 1/2 inch.

3.1.3 Galvanomagnetic Sample Mounting and Orientation

3.1.3.1 Sample holders and sample mounting

A sample holder with a mounted magnetoresistance sample is shown as Figure 3.3. The construction of these samples holders has been discussed by Blair[4] and Nelson[5]. The 1/8" thick platform and the body of the holder is machined from a single piece of aluminum. The aluminum is anodized (and dyed black) to provide a thermally thin yet electrically insulating layer. Seven #30 teflon insulated copper leads and a thermocouple pair are brought down a 3 to 4 foot length of thin wall, non-magnetic stainless steel support tube. The thermocouple bead is Pb-Sn soldered to a brass stud which is screwed through the sample platform. The electrical leads are terminated at soldering posts which are imbedded in a teflon terminal block. A similarly anodized aluminum can is screwed over the entire assembly. The can acts as an electrical and light shield and also serves to stablize the thermal environment of the sample. A small heater winding was added to the aluminum shield can when it was desired to make measurements at temperatures slightly above room temperature.

The galvanomagnetic sample, itself, was tied to the platform with cotton thread. All of the electrical leads (1.5 mil dia. copper voltage probes and 3.0 mil dia. copper current leads) were cemented to the platform with clear
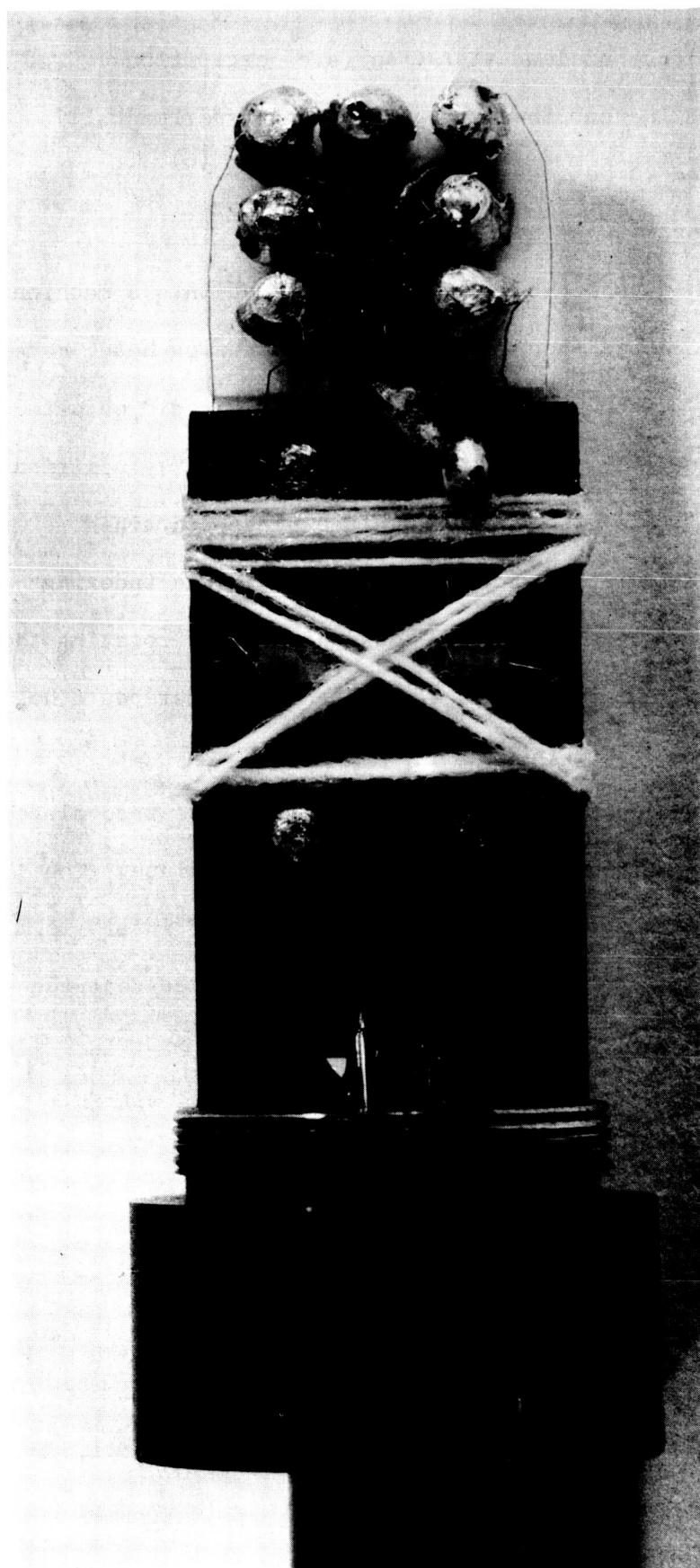
ABOUT 4 X MAGNIFICATION

0.5 cm

Fig. 3.3   Galvanomagnetic Sample Holder and Mounted Sample

fingernail polish. No evidence of lead vibration (a.c. excitation - d.c. magnetic field) was noticed in that the various types of experimentally measured voltages were found to be independent of frequency.[6]

3.1.3.2 Method of orienting mounted samples

The support tube of the sample holder was firmly taped into a machined groove in a specially constructed indexing head. This indexing head, made of brass, rotated in a 1/2" thick aluminum face plate which could be slid about on a table mounted over the dewar and magnet until properly positioned and then firmly clamped in place with dogs. The face plate contained indexing holes (3/32" dia.) every 15° on a 5" dia. circle. The indexing head had a sliding steel pin which mated with these holes. By rotating the head and mating the pin with the desired hole, the sample holder could be quickly, accurately and reproducibly indexed every 15°.

The angular zero reference was established by rotating the face plate until the Hall effect zero was found and then clamping it in place. The indexing head (and sample holder) could then be indexed at 15° intervals measured from the Hall effect zero orientation. It is estimated that the indexing head gave a relative orientation accuracy of $\pm$ 1° in azimuth. The angle of elevation of the sample current axis is estimated to be within $\pm$ 3° of the horizontal (or $\pm$ 3° of the vertical when appropriate).

3.1.3.3 Temperature and environment control

Room temperature measurements

Room temperature measurements were made in an empty (air filled) dewar. Electrical resistivity and the Hall effect were the only quantities extensively measured at room temperature. The time integral of Joule power dissipation over the elapsed measurement time resulted in a Joule heat

generated energy increment which was sufficient to raise the temperature of
the sample holder by 0.1°C in the most pessimistic case. This is a negligible
temperature change for resistivity and Hall effect measurements on an extrinsic
semiconductor. Some measurements were taken with the dewar filled with two
liters of unstirred kerosene. The same measurement results were obtained.
Room temperature was in the range of 26 ± 2°C.

Low temperature measurements

Extensive low temperature measurements were made at the temperature of
liquid nitrogen - 77.3°K. A single, glass walled dewar was used as a container
for the liquid nitrogen. The tail section of the dewar had an outside diameter
of about 1-1/8". The dewar had a capacity of 2-1/2 liters. Freshly prepared
liquid nitrogen was used for most of the measurement runs. Magnetoresistance
measurements runs were usually begun one hour after the sample holder had
reached liquid nitrogen temperature. The temperature of the sample holder
could be monitored with the internal thermocouple. It was found that the
bath temperature remained constant to within 0.2°C (which was the precision
of the thermocouple measurement at 77°K) over the period of time required
to make a complete measurement run - which was typically 3 hours. The neck
of the dewar was blocked off with a cloth plug.

Measurements as a function of temperature

Measurements of the Hall effect and electrical resistivity were made
as a function of temperature. This was done by letting the nitrogen evaporate
in the dewar and taking measurements as the sample holder drifted up in
temperature. The maximum rate of temperature change was about 1.5°C per
minute near 77°K. The rate of change decreased considerably as room
temperature was approached. Temperature, Hall effect, and the electrical

resistivity could all be measured within an elapsed time of about 15 seconds. Temperatures as high as 75°C were reached by using a small heater winding wound on the aluminum shield can.

3.1.3.4 Thermometry

Copper - constantan thermocouples were used to measure sample holder temperatures over the range 77.3°K to 350°K. Premium grade[7] #36 B&S gauge nylon insulated wire was used. Thermocouple beads were made with Pb-Sn solder. After mounting in the sample holders, the thermocouple voltages (referenced against an ice bath) were checked at room temperature (against a laboratory thermometer) and at liquid nitrogen temperature. Occasionally, a thermocouple would be checked at the temperature of a dry ice and acetone bath. The temperature read by the thermocouples were consistently found to be accurate within at least ± 0.5°C. Consequently, no corrections were applied to the thermocouple output voltage.

A tightly packed crushed ice and tap water reference junction bath was used. A temperature conversion table calculated from a National Bureau of Standards table was used[8].

3.1.4 Error Analysis-Galvanomagnetic Measurements

The various quanties - voltages, currents and dimensions - which are needed to calculate important transport parameters are listed in Table 3.1. The estimated accuracy of each measurement and the method of measurement are also indicated. When the probable errors of each experimentally measured contributing quantity are properly combined,[9] the following absolute accuracy estimates are obtained:

TABLE 3.1

ESTIMATED PROBABLE ERRORS OF MEASURED QUANTITIES
USED TO CALCULATE TRANSPORT COEFFICIENTS

QUANTITY	MEASUREMENT ACCURACY		METHOD OF MEASUREMENT
	Absolute:	Relative:	
Transverse Sample Dimensions	+0.003mm	same	Metric Micrometer
Spacing of Voltage Probes	+0.10mm	same	Vernier on a Traveling Stage Microscope
Electrical Currents	± 1/2%	same	Thermo-Milliameter
Magnetic Field	± 1/2%	same	Rotating coil fluxmeter
A.C. Sample Voltages-no Null	± 1-1/2%	± 1%	Preamplifier and Wave Analyzer
A.C. Hall Voltage-with Null	± 2%	± 1-1/2%	Same as above
A.C. Magneto-resistance voltage-with Null	± 3%	± 2-1/2%	Same as above
D.C. Voltages in Thermal Measurements	± 1/2%	± 1/2%	L&N type K Potentiometer
Temperature Differences in Thermal measure-ments	± 3%	± 3%	Type K Pot. and Copper Constantan Thermocouples

Electrical Resistivity $\pm$ 4.3%   ---- $\pm$ 1.2% Relative Accuracy

Hall Constant $\pm$ 2%

Hall Mobility $\pm$ 4.6%   ---- $\pm$ 2.1% Relative Accuracy

Magnetoresistance, $\frac{\Delta V}{V^o}$ $\pm$ 4% to $\pm$ 10%

(Depending upon the magnitude of the Hall effect voltage which is averaged out of the $\vec{B}(+)$ and $\vec{B}(-)$ magnetoresistance data).

Relative measurement accuracies have been indicated when they differ significantly from the absolute.

It should be mentioned that the above error estimates contain an inherent uncertainty. This is caused by the possible influence of sample inhomogeneities and departures from ideal galvanomagnetic sample geometry - mainly in the form of the finite diameters of the voltage probes. These points have been discussed to some extent in the literature[10]. The extent of these perturbations is difficult to estimate. The only available recourse is to use the best available crystals and the best possible sample preparation technology. Measurement reproducibility checks from sample to sample are of vital importance in this context.

3.2 THERMAL MEASUREMENTS

3.2.1 Thermal Conductivity and Thermoelectric Power Measurements

The thermal conductivity chamber is shown in Figure 3.4. The vacuum cryostat is shown as Figure 3.5. These figures are largely self explanatory. The monitoring thermocouple, TC-3, was sometimes taped to the outside of the thermal conductivity chamber. It essentially reproduced the reading of the cold junction thermocouple TC-2.

The hot junction, TC-1, and cold junction, TC-2, thermocouples were carefully soldered to the bottoms of their respective thermocouple wells

THERMAL AND ELECTRICAL CONTACT
IS MADE TO THE INDIUM PLATED CONTACT
AREAS OF THE CRYSTAL WITH GALLIUM. ALL
SOLDERING IS DONE AT ROOM TEMPERATURE
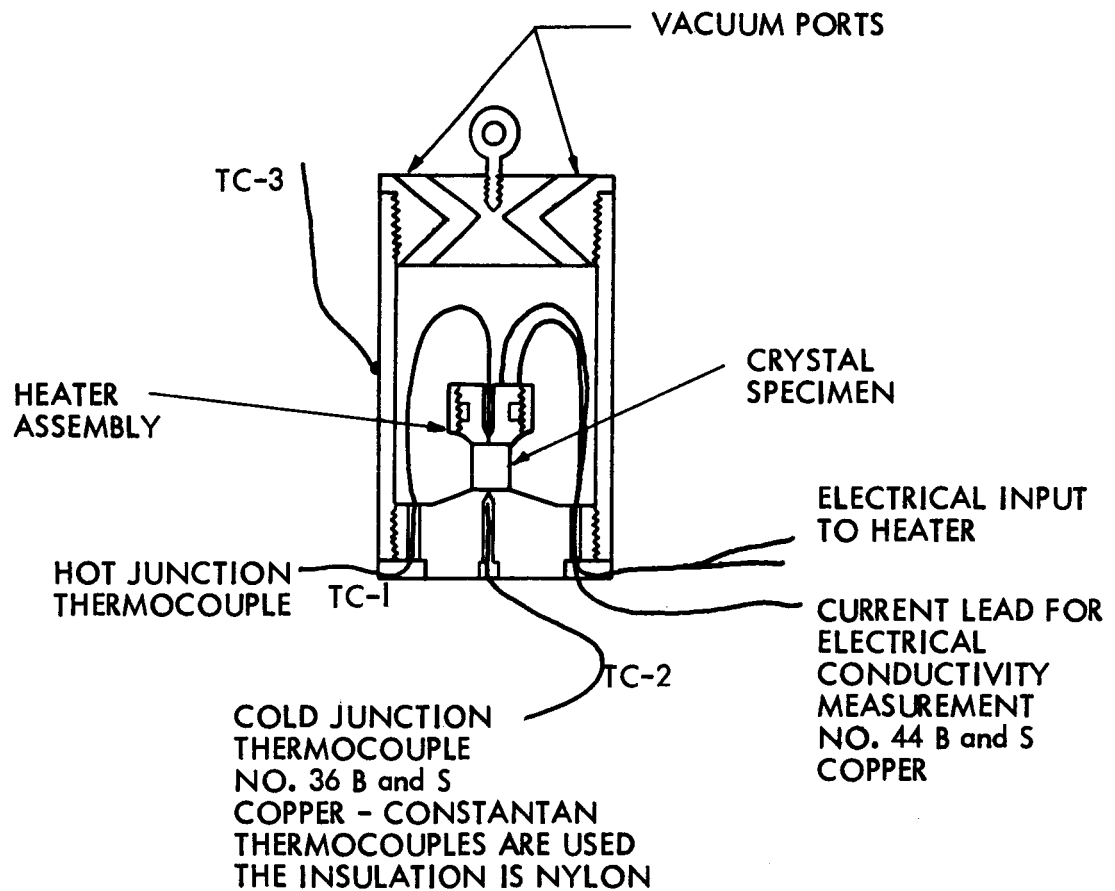
Scale: FULL SIZE   Material: GOLD PLATED COPPER

Fig. 3,4 Thermal Conductivity Chamber

CLAMPED (NOT SHOWN)
O-RING AND APIEZON
TYPE N GREASE SEAL

THERMOCOUPLE AND
ELECTRICAL LEADS

TUBE SEALED WITH
APIEZON TYPE W WAX

NO. 304-S.S.
PRESSURE FITTING
ASSEMBLY

PORT FOR AIR
BLEEDER VALVE

THERMOCOUPLE
VACUUM GAUGE

TO:
LIQUID NITROGEN
COLD TRAP AND
14 C.F.M. FOREPUMP

BRASS BLOCK

THIN WALLED
NICKEL-SILVER TUBING

NO. 321 THIN WALLED
S.S. TUBING

COPPER CHAMBER-

IMMERSED IN ICE-WATER
FOR THESE MEASUREMENTS

COMPRESSED
SPRING

PLASTIC HEAT
INSULATION

THERMAL
CONDUCTIVITY
CHAMBER

THERMOCOUPLE AND
ELECTRICAL LEADS

Approx. Scale:
1/2 FULL SIZE

Fig. 3.5 Vacuum Cryostat for Thermal
Conductivity Measurement

(0.040" dia.). The thermocouple beads are within 0.015" of the sample surfaces.

With a sample in place and the cryostat at 0°C, the thermal system would reach a steady-state condition in about 75 minutes after a change was made in the input power level to the heater.

The heat power conducted by the sample is equal to the electrical power input to the heater minus the stray power losses (lead heat conduction, radiation loss, residual gas convection losses). The stray losses were determined by cementing a polyfoam block - the same size as a thermal conductivity sample - in place and measuring the electrical power input required to maintain a given heater temperature. This loss was determined (on several ocassions) to be:

$$0.85 \pm 0.05 \ \frac{\text{milliwatts}}{°K}$$

over a temperature differential range of 2 through 8°C. The residual gas pressure in the cryostat was 4 to 8 μ for this calibration.

3.2.2 Thermal Measurement Instrumentation

The electrical instrumentation for the thermal measurements is shown in Figure 3.6. For electrical isolation, the reference junctions of the thermocouples were inserted into thin walled (1/2mm) glass tubes which were filled with Dow-Corning type 304 silicone heat sink compound. These tubes were then taped to the bulb of the bath temperature monitoring, mercury thermometer. This assembly was then inserted at least 6" into a dewar filled with well packed, finely crushed ice and water.

The electrical resistivity of the thermal samples was determined by a "two terminal" measurement. A d.c. electrical current was passed through the sample by means of a #44 B&S gauge copper wire attached to the heater
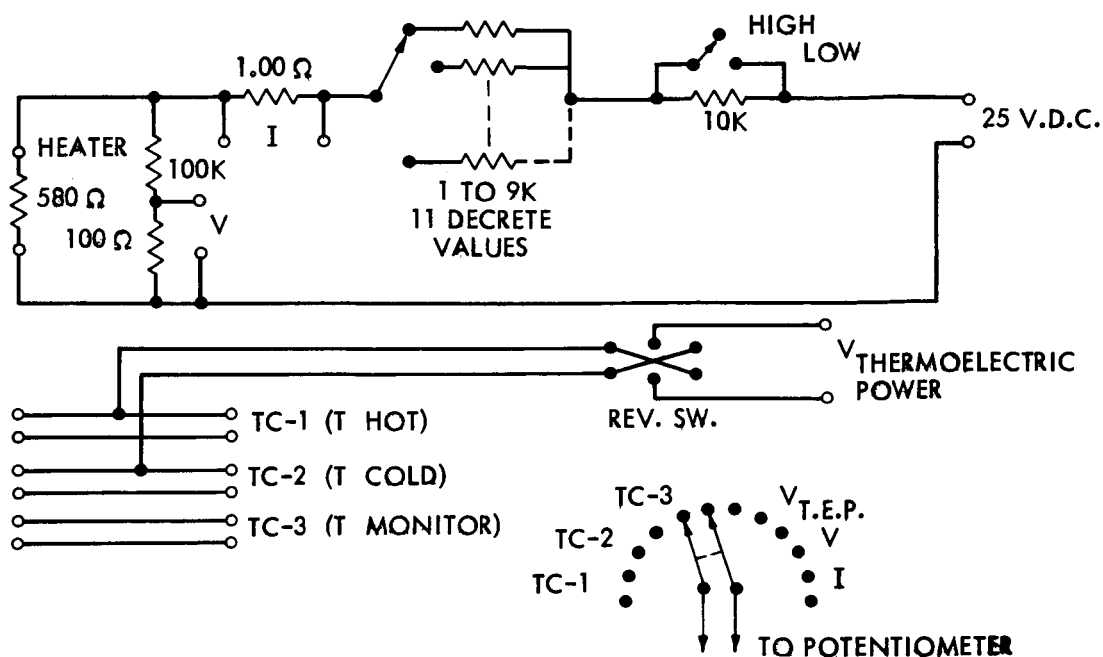
a) SWITCH BOX AND HEATER POWER CONTROL CIRCUITRY
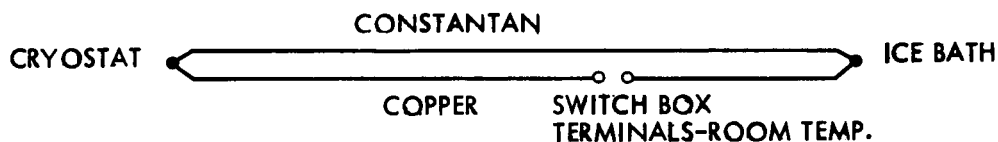
b) THERMOCOUPLE CIRCUIT
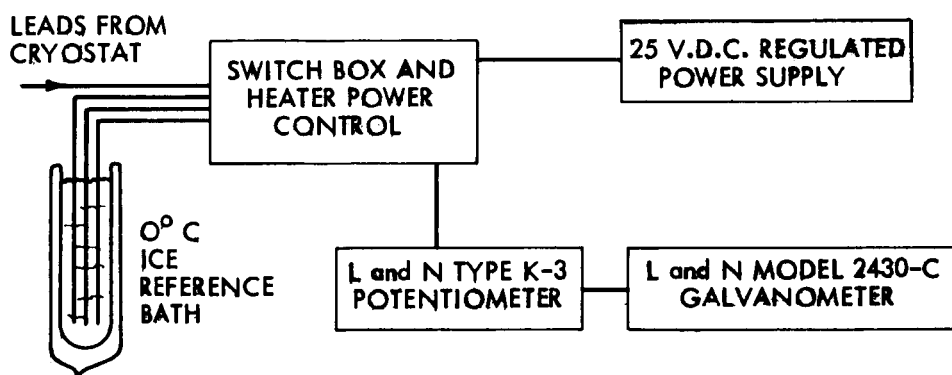
c) BLOCK DIAGRAM OF INSTRUMENTATION

Fig. 3.6   Thermal Conductivity Instrumentation

block. The thermal conductivity chamber served as the return path. This current was measured with the thermo-milliameter described in Section 3.1.2. The resulting voltage was measured with the copper leads of the thermocouple pair - TC-1 and TC-2. The L&N type K potentiometer was used for this measurement. This same pair of copper leads was also used to read thermoelectric power voltages. Readings were taken over roughly a decade variation of current levels and for both current polarities. No non-linear behavior was observed. Electrical resistivies determined in this manner were independent of sample length. They were also in good agreement with values measured on galvano-magnetic samples. Thus, the indium plated and gallium soldered contacts had negligible electrical resistance.

The measured thermal conductivities were found to be independent of sample length. Hence, the thermal resistance of the contacts was negligible also.

3.2.3 Thermometry

The premium grade of #36, nylon insulated, copper-constantan thermocouple wire described in Section 3.1.3.4 was also used in the thermal conductivity apparatus. After installation, the thermocouples were checked in the following way. The heat source was soldered directly to the heat sink. The monitoring thermocouple, TC-3 was taped to the outside of the chamber - as illustrated in Figure 3.4. The chamber was installed in the cryostat and evacuated. The cryostat was placed deep in a 7 liter dewar filled with tap water. After a 12 hour equilibration period, the three thermocouples were found to read the same temperature (about 21°C) to within one microvolt (40.5 μV/°C sensitivity at this temperature). The cryostat was then immersed in crushed ice and water. At 0°C, the outputs of the three thermocouples were found to agree within 2μV (38.7 μV/°C sensitivity at 0°C). On the basis of several experiments of this

sort, it is felt that the temperature differentials ($\Delta T = T_{hot} - T_{cold}$) were measured to an accuracy of at least 0.10°C. Thermal conductivity readings – usually three for each sample orientation – were taken with temperature differentials of 1.5 to 4°C. Occasionally, ΔT ranged as high as 8°C. The thermal conductivities calculated for the different temperature gradients were consistently found to agree to with at least ± 2%. This adds more confidence to the accuracy of the thermometry.

3.2.4 Error Analysis

Table 3.1 presents the quantities which are needed to calculate the transport parameters along with their estimated accuracies of measurement. The comments of Section 3.1.4 are pertinent here also. From these measurements estimates, the following *absolute probable error estimates* on the transport parameters are obtained:

<div align="center">

Thermal conductivity : ± 4%

Thermoelectric power : ± 3%.

</div>

3.3 BIBLIOGRAPHY

1. A.C. Beer, Galvanomagnetic Effects in Semiconductors, pp. 66-68,
    Academic Press, New York, N.Y., 1963.

2. E.H. Putley, The Hall Effect and Related Phenomena, pp. 48-52,
    Butterworth, London, 1960.

3. W.M. Bullis, Galvanomagnetic Effects in n-type Germanium, pp. 48-50,
    Ph.D thesis, Dept. of Physics, Mass. Inst. of Tech., Cambridge, Mass.,
    1956.

4. John Blair, Technical Report AFCRC-TN-60-753, DSR 7994, Contract
    AF 19(605)-4153 prepared for Electronic Research Directorate, Air
    Force Cambridge Research Center, Air Research and Development Command,
    USAF Bedford, Mass., June 15, 1960.

5. R.E. Nelson, Preparation and Electronic Transport Properties of Mercury
    Telluride, Sc.D. thesis, E.E. Department, Mass. Inst. of Tech.,
    Cambridge, Mass., 1962.

6. R.J. Schwartz, Thermal and Electronic Transport Properties of a Bi_2Te_3-
    Sb_2Te_3-Bi_2Se_3 Semiconducting Alloy, Sc.D. thesis, E.E. Department,
    Mass. Inst. of Tech., Cambridge, Mass., May, 1962.

7. Thermocouple Wire-Copper Constantan: Thermo-Electric Co., Inc.,
    Saddle Brook, New Jersey, Type NN-36-DDT.

8. S.P. Denker, "Low Temperature Thermometry and Copper-Constantan
    Thermocouple Calibration Table (4.2°K - 300°K)", unpublished report
    prepared by the Laboratory for Insulation Research, M.I.T., December, 1960.

9. Ernest Frank, Electrical Measurement Analysis, Ch.7, McGraw-Hill, Inc.,
    New York, N.Y., 1959.

10. A.C. Beer, op. cit., p. 57 and section 27.

CHAPTER 4

PRESENTATION AND DISCUSSION OF EXPERIMENTAL RESULTS

4.1 INTRODUCTION

This chapter presents and discusses the results of the following types

of experiments on p-type ZnSb:

1. Annealing experiments.

2. Thermal measurements - thermoelectric power and

   thermal conductivity.

3. Hall effect and electrical resistivity measurements

   between 77.3 and 325°K.

4. Anisotropy of the Hall effect.

5. Magnetic field dependences of the Hall and magneto-

   resistance effects.

6. Extensive magnetoresistance measurements at 77.3°K.

Pertinent comments on experimental procedure are included when this is

felt to be necessary.

The following convention is used to label the crystal axes:

$$1 = <100> = a = 6.20\overset{\circ}{A}$$

$$2 = <010> = b = 7.74\overset{\circ}{A}$$

$$3 = <001> = c = 8.10\overset{\circ}{A}$$

The following convention is used regarding the meaning of the subscripts

on the elements of the galvanomagnetic tensors:

1. Thermal conductivity: κ_{ij}

   κ(heat flux component) (temperature gradient component)

2. Thermoelectric power: α_{ij}

   α(electric field component) (temperature gradient component)

3. Electrical resistivity: ρ_{ij}

ρ(electric field comp.) (electric current density comp.)

4. Hall coefficient: $R_{ijk} = \rho_{ijk}$

ρ(elec. field comp.) (electric current dens. comp.)x

(magnetic field comp.)

5. Magnetoresistance coefficients: ρ_{ijkl}

ρ(elec. field comp.) (electric current density comp.)x

(magnetic field comp.) (magnetic field comp.)

Appendix 1 shows that the transport tensors have the following possible non-zero elements when they are referred to the principal coordinate system of the crystal:

1. Thermal conductivity (3):

$$\kappa_{11}, \ \kappa_{22}, \ \kappa_{33}$$

2. Thermoelectric power (3):

$$\alpha_{11}, \ \alpha_{22}, \ \alpha_{33}$$

3. Electrical resistivity (3):

$$\rho_{11}, \ \rho_{22}, \ \rho_{33}$$

4. Hall coefficients, $R_{ijk} = \rho_{ijk}$, (3):

$$\rho_{123} = - \rho_{213}$$

$$\rho_{312} = - \rho_{132}$$

$$\rho_{231} = - \rho_{321}$$

where Onsager symmetry requires the indicated equalities.

5. Magnetoresistance coefficients (12):

$$\rho_{1111} \quad \rho_{2211} \quad \rho_{3311} \quad \rho_{1212}$$

$$\rho_{1122} \quad \rho_{2222} \quad \rho_{3322} \quad \rho_{1313}$$

$$\rho_{1133} \quad \rho_{2233} \quad \rho_{3333} \quad \rho_{2323}$$

4.2 ANNEALING EXPERIMENTS ON UNDOPED CRYSTALS OF P-TYPE ZnSb

4.2.1 Introduction

As the measurements on undoped single crystals of p-type ZnSb progressed, several puzzeling occurrences were noticed.

1. Subjecting the crystals to temperatures of 50°C for 15 to 30 minutes in the course of Hall effect measurements would increase the apparent room temperature hole concentration by 5 or 10%. This "added" number of holes would slowly disappear with time.

2. Careful, d.c. potentiometer measurements ($\pm$ 1/2% relative accuracy) of the electrical resistivities of a set of samples indicated that the resistivities were increasing by a few percent over a period of several weeks.

Exposing a new crystal surface layer by sandblasting away 10 or 20 microns of the surface had no effect on the apparently changing hole concentration. Kot and Kretsu[1] and Mazelsky[2] also qualitatively observed that heating an undoped ZnSb crystal would increase the apparent hole concentration and that the hole concentration would then slowly decrease with storage at room temperature.

All of this provided motivation for the following annealing experiments. The following experiments serve as the first recording of a phenomena that has only been very briefly mentioned and never characterized in the literature[1,3,4]. A plausible model is proposed for the observed phenomena. However, this model must be regarded as being speculative, since needed basic information, such as the electrical effects of departures from the ZnSb stoichiometric composition and the magnitude of the self diffusion coefficients are not avilable for quantitative tests of the validity of the model.

4.2.2 Experimental Procedure

Galvanomagnetic sample bars were annealed in an open tube furnace. The ambient atmosphere was sometimes nitrogen but often argon at a flow rate of less than one s.c.f.h. A dry ice and acetone cold trap was used in the gas line. The results did not seem to depend upon which gas was used. Many of the sample bars were annealed with their electrical contacts and copper lead wires in place, since they had already been used for other measurements. In such cases, the annealing temperature did not exceed 175°C in order to avoid melting the contacts. The contact technology has been discussed in Section 2.6.3. In order to establish that the observed phenomena were not caused by contact diffusion, a number of bars were annealed without contacts - the contacts being applied just before electrical measurements were made. Contact-less bars were annealed at temperatures as high as 240°C. Temperatures were read with a chromel - alumel thermocouple that had been calibrated at 100°C and 0°C.

The Hall effect and the electrical resistivity were measured with the a.c. apparatus described in Section 3.1.2. Sample recovery was monitored at room temperature through periodic Hall measurements. After annealing, samples were stored in the ordinary room atmosphere under dust covers.

A typical experimental run consisted of measuring the room temperature electrical resistivity and Hall coefficient, demounting from the sample holder, washing in trichlorethlyene, acetone and methyl alcohol, annealing, quenching to room temperature (time required, 5 to 10 minutes), remounting in the sample holder, and monitoring the Hall effect as a function of time. The first electrical measurements were taken within 1/3 to 1 hour of the moment when the temperature dropped to end the annealing cycle.

After initial post annealing measurements had been made, the surfaces
of several of the samples were sandblasted. About 10 microns of the surface
was removed. This had no effect on the change in Hall coefficient or
resistivity which was caused by annealing. Thus, it seems as though a bulk
effect was observed. Annealing did not change the Hall mobility appreciably.

Equilibrium conditions, at a given annealing temperature, were established
in about 6 hours. This was established by reannealing several of the samples
(with contacts) for an additional 10 to 24 hours at their respective annealing
temperatures. Some annealing cycles ran for 72 hours. No change in the
corresponding experimentally measured hole concentration was noted.

With one exception, the samples which were annealed without electrical
contacts in place were provided with sidearms. The width of these sidearms
($\sim$2.0 mm) was equal to the width of the main body of the sample. The length
of a sidearm was equal to its width. This is a rather non-ideal sidearm
geometry, but it was necessitated by the brittle nature of ZnSb. Electrical
contacts were applied with a hand held soldering iron in the form of $\sim$1 mm dia.
solder dots at the end of the sidearms. The sidearm samples were subjected
to the same experimental procedure already outlined except that all traces of
lead-tin solder contact material were removed by sandblasting before an anneal-
ing cycle took place. The one exception, identified as C-1081-C AN-2, was a
simple bar (1.2 mm wide) which was annealed without contacts, had the above
described contacts applied directly to its surface, was measured and then
reannealed with these contacts in place. Thus, C-1081-C AN-2 had electrical
contacts that were from 5 to 10 times the diameter ($\sim$0.1 mm) of the usual
galvanomagnetic sample voltage contacts (described in Section 2.6.3).

4.2.3 Experimental Results

The apparent hole concentration was obtained by simply inverting the measured Hall coefficient, p = 1/Rq. The observed carrier concentrations are plotted as a function of the reciprocal annealing temperature in Figure 4.1. The slopes of the straight lines correspond to an apparent activation energy of 1.0 ev. The particular Hall coefficient which was measured for each sample is indicated along with each sample identification.

The points which were obtained for the contactless samples lie below the points which were obtained for the samples annealed with the contacts in place. It is believed that this is due to a difference in the gross geometries of the two types of samples. When one pair(of the two pairs) of sidearms was removed and replaced by the usual galvanomagnetic contacts (diameter ~0.1 mm – refer to Section 2.6.3), the measured hole concentration was about 30% larger than that measured with the remaining sidearm pair. This was found to be true in two checks of this sort. Thus, the curve for the sidearm samples might logically be translated upward to the position shown by the dotted line shown on Figure 4.1. It is felt that the remaining discrepancy between the curves can probably be explained in terms of further geometrical effects. This discrepancy is probably not due to contact diffusion effects since both straight lines have the same slope – a rather fortuitous happening if the upper curve was actually due to diffusion. Furthermore, checks such as annealing samples with one sidearm pair (no contacts) and one set of the usual contacts produced results which were entirely consistent within the framework of the geometry effect mentioned above. Finally, the point for crystal C-1081-C sample AN-2, annealed with contacts in place, actually lies closer to the lower curve (contactless

Fig. 4.1 Hole Concentration vs. Reciprocal Annealing Temperature – p-Type ZnSb

THE FRACTION OF EXCESS
CARRIERS WHICH HAVE
DISAPPEARED = W

$$W = \frac{p(t=0) - p(t)}{p(t=0) - p(t=\infty)}$$

CURVE Ⓐ $W = 1 - \exp(-K_1 t)$ FOR $t > 10$ HRS.

CURVE Ⓑ $W = 1 - \exp(-K_2 t^{2/3})$

SLOPE = 0.67

Ⓐ

Ⓑ

CRYSTAL C-1068-8 SAMPLE 1
NO CONTACTS IN PLACE
DURING ANNEALING
ANNEALING TEMP. = 240° C

AFTER ANNEALING –
TIME STORED AT ROOM TEMPERATURE

t = HOURS
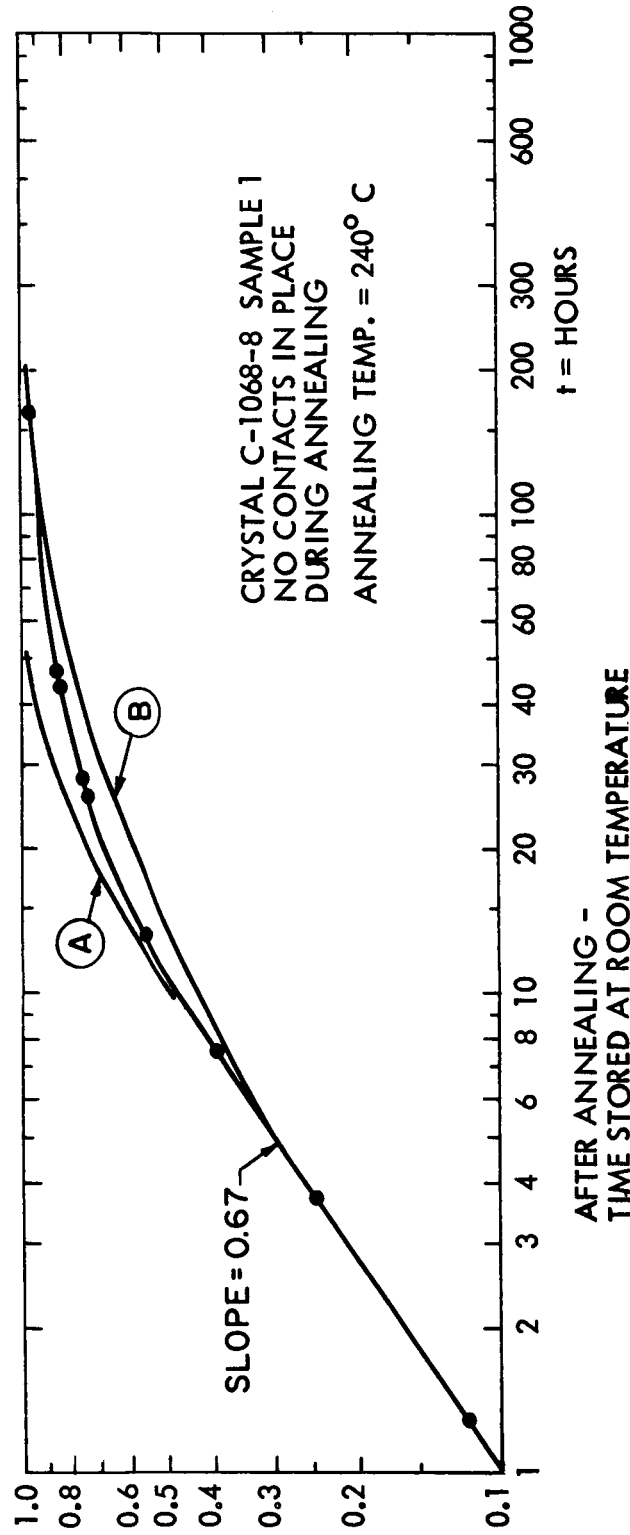
Fig. 4.2 Typical Recovery of P-Type ZnSb After Annealing

samples) than the upper.

All of the above points can be clarified by further, careful experiments. What has been established by Figure 4.1 is that the hole density can be changed by annealing in an inert atmosphere and that the resultant experimental points on a log p vs. $\frac{1}{T}$ plot indicate that the process has an activation energy of about 1.0 ev.

When the annealed samples were stored at room temperature, it was observed that the hole concentration decreased with increasing time. A typical observed result is shown as Figure 4.2. The ordinate, W, is equal to the fraction of excess holes (introduced by annealing) that has disappeared at a given time, t. It is seen that W approaches unity (complete sample recovery) assymptotically. The recovery is 90% complete in 100 hours. This was the fastest observed rate of recovery. At the opposite extreme, other samples would only reach 40% recovery in 100 hours and would seem to approach 90% recovery in 1000 to 3000 hours - as was estimated by extrapolating their recovery curves. This sort of recovery phenomena was explicitly observed in 8 samples. Once again, this phenomena was not changed by sandblasting a fresh surface on several of the annealed samples.

4.2.4 Discussion of Experimental Results

A tentative explanation of what may be happening can be briefly stated. This model is essentially the same as that advanced for the similar behavior of p-type lead telluride[5].

This model states that Figure 4.1 is essentially a representation of the ZnSb retrograde solidus line on the Zn-Sb phase diagram. The ZnSb lattice can be thought of as containing more antimony at the higher temperature. Of course, it is uncertain whether excess antimony or zinc is incorporated into

the lattice at higher temperatures. The nature of the electrically active point defect in the lattice is also open to speculation. At any rate, at higher temperatures, it is possible that additional antimony is supplied by crystal dislocations which act as a source or a sink for antimony depending upon the annealing temperature involved and the exact shape of the retrograde solubility line.

Hence when a crystal is annealed at an elevated temperature, a new concentration of electrically active antimony (or zinc) is incorporated into the lattice and the hole concentration increases. This new equilibrium is reached in a fairly short time - several hours. Afterwards, when the crystal is allowed to remain at room temperature, the antimony (or zinc) precipitates out on dislocation lines in the crystal as electrically neutral atoms. This room temperature precipitation process is slow-taking hundreds or thousands of hours. Ham[6] has presented a theory for diffusion assisted precipitation. The theory predicts a slope of $t^{2/3}$ for the initial portion of the precipitation curve and a long time limiting behavior of $(1-\exp K_1 t)$, where K_1 is a constant for a given sample and temperature.

The short time portion of the recovery curve, Figure 4.2, does have an initial slope of 0.67. It should be noted that the concentration of holes at zero time $p(t=0)$, is needed in order to calculate the precipitated fraction, W, accurately - especially for short times. Since the first Hall measurement took place from 1/3 to 1 hour after the annealing was stopped, $p(t=0)$ had to be approximated. This was done by assuming that $K=K_0 t^{2/3}$ initially (where K_0 is a constant for a given sample and temperature) and using the first two experimentally measured hole densities to compute $p(t=0)$. This value then was used to compute W at all later times. This procedure might be criticized

for the sample shown in Figure 4.2, since only two additional points lie near

the $t^{2/3}$ portion of the curve. However, when used with other samples -

especially those with slower recovery rates - as many as six additional points

were found to lie on the $t^{2/3}$ line. Hence the presence of a $t^{2/3}$ behavior

is reasonably well established for the short time recovery. The value for

$p(t=\infty)$ was assumed to be 1 x 10^{16} as was determined by an extrapolation of

the straight lines of Figure 4.2 to room temperature.

The long time behavior of the recovery was found to follow neither $(1-\exp K_1 t)$

nor the $(1-\exp K_2 t^{2/3})$ with which Harper[7] was able to fit the observed

precipitation of carbon and nitrogen in cold-worked alpha iron. The exact

form - but not the assymptotic nature - of the long time portion of the

recovery curve was found to vary slightly between samples. This is not too

surprising since Ham[6] has made the observation that the long term mathematical

form of the precipitation curve can mirror the type of systematic agglomeration

of dislocations present in the sample. His theory was developed for a uniform

array (etch pits forming a two dimensional square array) or a random array of

dislocations. The magnitude of the amount of recovery at a given time is

also sensitive to the dislocation density - being greater for higher dis-

location densities, as might be expected. The values of K_1 and K_2 used in

curves A and B of Figure 4.2 were determined by fitting the curves to the data

at t = 10 hrs and t = 1.25 hr respectively.

In summary, it has been established that the hole concentration in p-

type ZnSb can be changed by annealing at elevated temperatures in an inert

atmosphere. This phenomena does not basically originate as contact diffusion

or as a surface effect. The observed time recovery at room temperature

exhibits the general functional form expected for stress assisted precipit-

ation on crystal dislocations.

In order to more firmly establish the origin of this behavior and a more exact model, the following types of experiments are necessary:

1. The identity of the electrically active atomic species must be determined. This might be done by introducing departures from the ZnSb stoichiometry with vapor annealing experiments. This would establish the composition fine structure on the ZnSb solidus line - at least at elevated temperatures. This would also be a promising approach to try in attempting to produce n-type ZnSb.

2. The diffusion coefficients (3 in number) should be measured for the electrically active atomic species. This should be done at or near the temperature at which the sample recovery is monitored.

3. Careful determinations should be made of the density and geometrical grouping of the dislocations present in each crystal sample used in annealing experiments.

4. The method of monitoring the hole density should, ideally, be able to give a rapid hole density determination at any time during or after the annealing cycle. A suitable method must be found.

The phenomena observed above might possibly be the cause of the high temperature instabilities which have been observed in cast ZnSb thermo-elements (refer to Section 1.1'. It is also obvious that the above phenomena can have a profound influence on the results of electrical measurements on undoped ZnSb crystals. For example, crystals are usually cycled down to room temperature in a matter of hours after growth. But, the hole concentrations in a newly grown crystal may take weeks or months to equilibrate at room temperature. This complicates the determination of the anisotropy in the

galvanomagnetic properties of ZnSb.

4.3 THERMAL MEASUREMENTS

4.3.1 Introduction

The following measurements were made with the apparatus described in Section 3.2.2. The cold junction temperature was 0°C. The temperature differentials ($\Delta T = T_{Hot} - T_{Cold}$) used ranged between 1.5 and 4°C. On occasion ΔT was as high as 8°C. The reported results are independent of the temperature differential which was imposed. As explained in Section 3.2.2, the electrical conductivity of the thermal samples was determined by a two terminal resistance measurement. The thermal and electrical resistances of the sample contacts were found to be negligible.

4.3.2 Thermoelectric Power Measurements

Figure 4.3 presents the measured thermoelectric powers as a function of electrical conductivity. Good straight lines are obtained on the semi-logarithmic plot. Note that 4 determinations of the anisotropy of the thermo-electric power were made at 4 different doping levels. At a given doping level, the same single crystal cube was measured along three successive axes to reliably determine the anisotropy. The quoted thermoelectric powers are referenced to the thermoelectric power of copper, + 2.7 μV/°K at 0°C[8].

It is seen that the thermoelectric power of p-type zinc antimonide is isotropic to within the estimated experimental accuracy of ± 3%. Although the points do not appear on Figure 4.3 because the electrical conductivities were not determined, the thermoelectric power of undoped p-type ZnSb ($\alpha = + 680$ μV/°K) was found to be isotropic also.

Using the results of Appendix 2, Section A.2.7, Eq. A.2.84, the thermo-electric power for a single general ellipsoid valence band (anticipating the

Fig. 4.3 α vs. Log σ
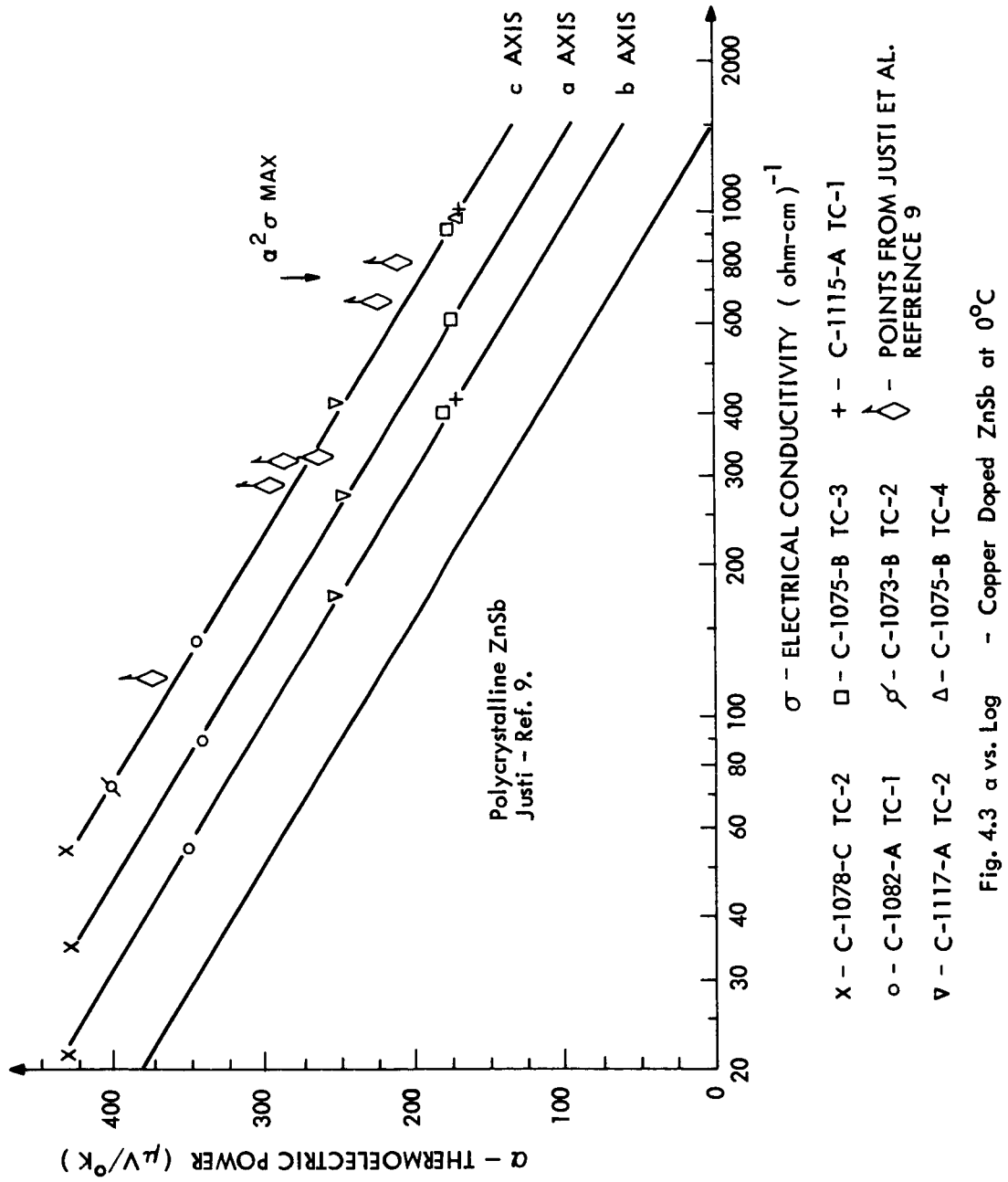
discussion of Chapter 5) can be written as:

$$\alpha_{ij} = \frac{1}{Tq} \frac{<(E-E_F)\tau_{ii}>}{<\tau_{ii}>} \delta_{ij} \qquad (4.1)$$

The notation is explained in Appendix 2. Thus, it is seen that the thermoelectric power does not depend upon the mass anisotropy of the valence band. The thermoelectric power will be isotropic if:

1. The relaxation time, τ_{ii}, is a scalar – in particular a scalar function of energy:

$$\tau_{ii} = F(E)$$

2. The relaxation time tensor, which is assumed to be diagonal in the same coordinate system as the valence band effective mass tensor, can be expressed as a diagonal matrix of constants times some function of energy:

$$\tau_{ij} = \begin{pmatrix} \tau^{\circ}_{11} & 0 & 0 \\ 0 & \tau^{\circ}_{22} & 0 \\ 0 & 0 & \tau^{\circ}_{33} \end{pmatrix} F(E)$$

Assuming that $F(E) = E^r$, Eq. 4.1 can be evaluated to give:

$$\alpha_{ii} = \frac{k}{q} [(r + 5/2) - \frac{E_F}{kT}] \qquad (4.2)$$

where nondegenerate statistics are assumed. Energy is measured from the edge of the valence band. Hence, E_F is numerically negative in the above. Assuming that lattice scattering predominates at 0°C (refer to Section 4.3), $F(E)=E^{-1/2}$ and $r = -1/2$ in Eq. 4.2. Hence:

$$\alpha_{ii} = 8.63 \times 10^{-5} [2 - \eta] \qquad \text{volts/°K} \qquad (4.3)$$

where, η is the reduced Fermi level, E_F/kT. This equation indicates that the Fermi level of crystal C-1078-C lies in the energy gap, about 3kT from the

valence band edge. Hence, conduction processes in this crystal – on which the major portion of the magnetoresistance data was taken – could be described with classical statistics.

Using the exact, Fermi-Dirac function, evaluation[10] of Eq. 4.1 with the assumption that lattice scattering dominates, Table 4.1 was constructed:

TABLE 4.1

APPROXIMATE FERMI LEVEL LOCATIONS AT 0°C

Crystal	Thermoelectric Power	Location of Fermi Level – Negative Values are in the Energy Gap
C-1081-C	680 μV/°K	-6kT
C-1078-C	430	-3
C-1082-A	345	-2
C-1117-A	250	-0.7
C-1075-B	175	+0.5

Anticipating the discussion of Section 4.3.4, the maximum of $\alpha^2\sigma$ (thus, for practical purposes, the maximum thermoelectric figure of merit) occurs at $\sigma_{33} = 740$ $(ohm-cm)^{-1}$ which corresponds to $\alpha = 195$ μV/°K. At this doping level, the Fermi level is located at about + 0.1 kT into the valence band.

4.2.3 Thermal Conductivity Measurements

Figure 4.4 presents the results of thermal conductivity measurements on p-type ZnSb at 0°C. The published data point of Just et al.[9] is included for comparison. This is for an unspecified orientation.

There is about a 12% anisotropy in the thermal conductivities. It seems reasonable to order the thermal conductivities as:

$$\kappa_{33} > \kappa_{22} > \kappa_{11}$$
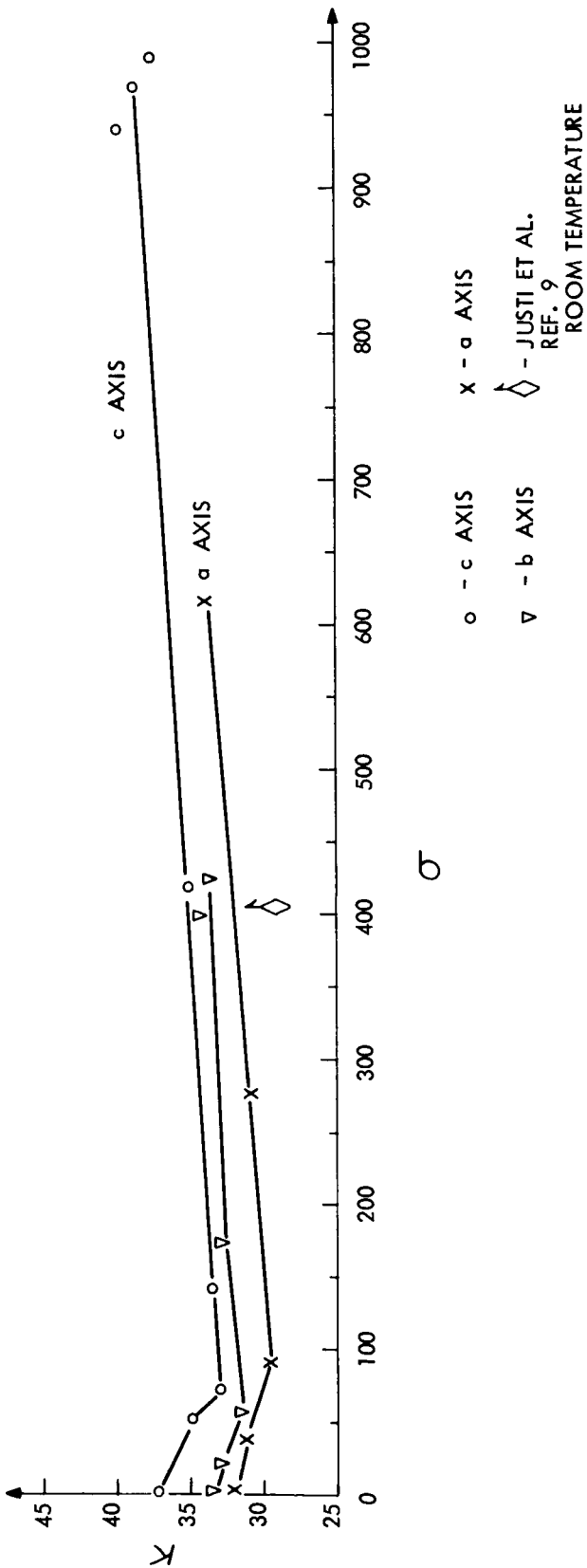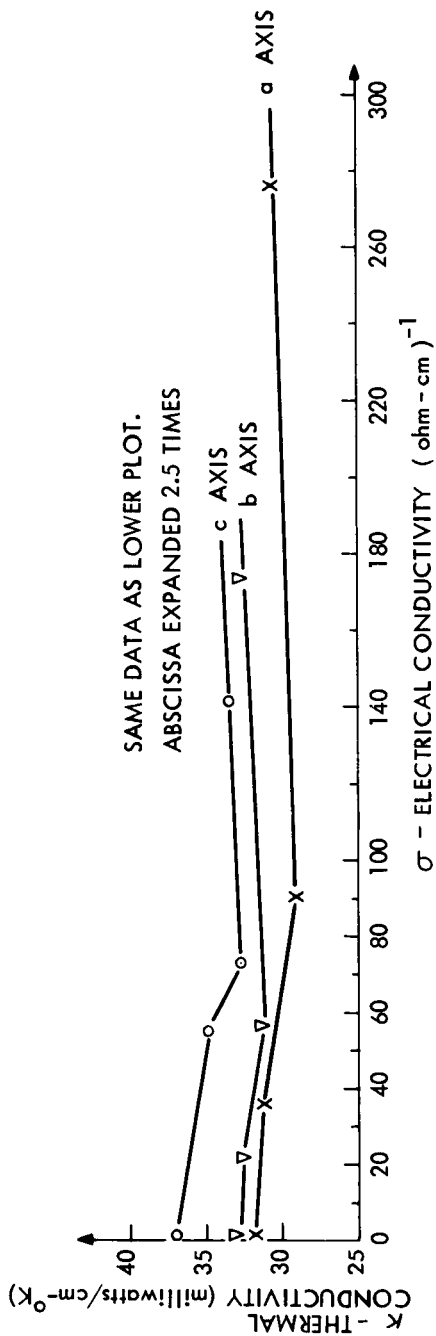
Fig. 4.4 Thermal Conductivity vs. Electrical Conductivity Copper Doped ZnSb - Measured at 0°C

even though the anisotropies are close to the estimated limits of probable experimental error.

Evidently, almost the entire amounts of the observed thermal conductivities are due to the lattice (phonon) component. The approximately 10% upswing in the curves as the electrical conductivity approaches 1000 $(ohm-cm)^{-1}$ is probably due to increasing heat conduction by holes. Due to the large lattice component, it is not possible to estimate the Lorentz numbers from this data. As is shown in Appendix 2 (Eq. A.2.86), these are given by:

$$L_{ii} = \frac{\kappa_{ii}}{\sigma_{ii}T} = \frac{1}{T^2q^2} \left\{ \frac{<(E-E_F)^2\tau_{ii}>}{<\tau_{ii}>} - \frac{<(E-E_F)\tau_{ii}>^2}{<\tau_{ii}>^2} \right\} \qquad (4.4)$$

and are isotropic under the same conditions that were outlined for isotropy in the thermoelectric power (Section 4.2.2).

The upswing in the curves as they approach the data points for the undoped crystal, C-1081-C, $\sigma \sim 2$ $(ohm-cm)^{-1}$, may be due to the onset of ambipolar heat transport[13]. However, the observed changes are close enough to the probable limits of experimental error to make any further discussion very speculative.

4.3.4 Thermoelectric Figure of Merit for p-Type ZnSb

Also shown on Figure 4.3 are the data of Justi et al.[9] for single crystals and polycrystals of ZnSb. Their measurements were probably made at room temperature. No orientations were reported for the single crystal specimens.

Notice that the c-axis gives the highest figure of merit[11] for thermoelectric applications:

$$Z = \frac{\alpha^2\sigma}{\kappa} \qquad (°K)^{-1} \qquad (4.5)$$

This is due to the large anisotropy in the electrical conductivity. This is

seen to be $\sigma_{33} \simeq 1.5 \ \sigma_{11} \simeq 2.5 \ \sigma_{22}$.

The c-axis data of Figure 4.3 has the following analytical representation:

$$\alpha = 795 - 210 \ \log_{10}\sigma \quad \mu V/°K \tag{4.6}$$

where σ has the units of $(ohm-cm)^{-1}$. The maximum of $\alpha^2\sigma$ can be found by differentiation. The result is:

$$\alpha^2\sigma \bigg|_{\substack{0°C \ maximum \\ at \ \sigma = 741 \\ (\Omega-cm)^{-1}}} = 2.74 \times 10^{-5} \ \frac{watts}{cm-(°K)^2}$$

The thermal conductivity data of Figure 4.4 indicates that

$$\kappa_{33} \simeq 0.037 \ \frac{watts}{cm-°K}$$

at $\sigma_{33} = 740 \ (ohm-cm)^{-1}$. Thus:

$$Z_{maximum} = 0.74 \times 10^{-3} \ (°K)^{-1}$$

for p-type ZnSb at 0°C.

Our analysis of the data presented by Justi et al.[9] yields a

$$Z_{maximum \ (Justi \ Ref. \ 9)} = 1.18 \times 10^{-3} \ (°K)^{-1}$$

Evidently, this is a room temperature result. The only thermal conductivity value quoted by Justi et al. was 0.029 watt/cm-°K which apparently corresponded to an electrical conductivity of 400 $(ohm-cm)^{-1}$. This is about 20% below the 0°C result measured for the c-axis in this work. This difference in thermal conductivities accounts for most of the difference in these two maximum thermoelectric figure of merits. Justi et al.[9] quote a maximum figure of merit of $Z \simeq 1.0 \times 10^{-3} \ (°K)^{-1}$ for polycrystalline material.

In conclusion, it is seen that even though the $\alpha^2\sigma$ product is appreciably higher in single crystals of ZnSb, the factor of ~ 2 increase in thermal

conductivity results in a figure of merit which is about that of polycrystalline material.

In this context, it is seen that the thermoelectric figure of merit of ZnSb single crystals might be greatly improved if their thermal conductivity can be reduced without affecting the electrical properties. This might be done by alloying a third atom into the ZnSb crystal lattice to decrease phonon mean free paths by mass fluctuation scattering[12].

4.4 HALL EFFECT AND ELECTRICAL RESISTIVITY MEASUREMENTS AS A FUNCTION OF TEMPERATURE

4.4.1 Introduction

These measurements were made with the galvanomagnetic samples mounted in sample holders in exactly the manner shown in Figure 3.3. An aluminum cover was screwed on the sample holder to complete the thermal and electrical shielding of the mounted sample. The electrical measurements were made as the sample holder drifted up from the temperature of liquid nitrogen, 77.3°K, to room temperature. A small heater, mounted on the shield cover, was used to reach temperatures slightly above room temperature - viz. up to 325°K. This has been explained in Section 3.1.3.3.

4.4.2 Measurements on Undoped ZnSb

Figure 4.5 shows the majority of the results which were obtained with the undoped, p-type crystal, C-1081-C. The majority of the samples were not measured far into their intrinsic regions. This was because of the annealing phenomena which has been discussed in Section 4.1. It was desired to preserve the nearly constant (with time) hole densities in these samples so that reproducible magnetoresistance measurements could be made. The probable mechanism for the annealing phenomena was not recognized until after the
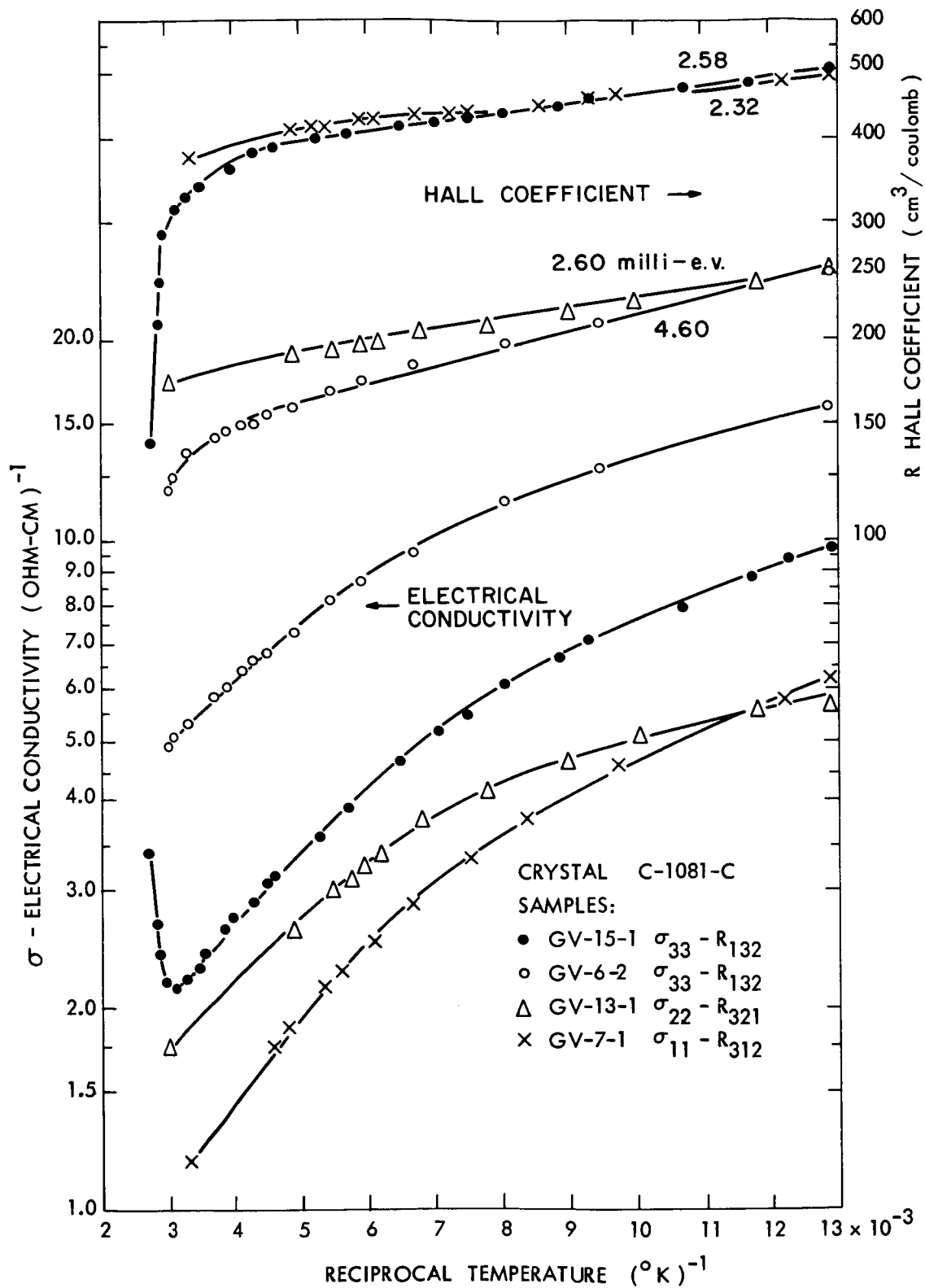
Fig. 4.5 Hall Coefficient and Electrical Conductivity
vs. 1/T. Undoped p – Type Zn Sb

galvanomagnetic measurement program was focussed on the copper doped samples.

In addition to R_{132} (sample GV-15-1 on Figure 4.5), R_{231} was measured in the intrinsic range on a sample from an earlier undoped crystal. Neither R_{132} or R_{231} was found to undergo inversion in the intrinsic range. This implies that holes have higher mobilities than electrons - at least in the "3" direction[14]. Komiya, Masumoto and Fan[14] have presented a plot of R_{213} in the intrinsic region. No inversion was observed. The data of Kot and Kretsu[1] on three different Hall coefficients, referred to a coordinate system defined by the planes of easy crystal cleavage, also shows no inversion in the intrinsic range. Thus, it is probable that the hole mobilities are greater than the electron mobilities in the "1" and "2" directions, also.

The slopes of the Hall coefficient curves (Figure 4.5) indicates that the acceptor level which is responsible for the p-type conduction has an activation energy, E_A, of about 4.6×10^{-3} electron volt. Komiya, Masumoto and Fan[14] also have presented a curve which has a slope which corresponds to 4.6×10^{-3} electron volts. Measurements of this sort can yield E_A or $E_A/2$ depending on the concentration of compensated donor centers which are present[15]. The slopes in the neighborhood of 2.3 to 2.6×10^{-3} ev. apparently correspond to $E_A/2$, while sample GV-6-2 - being more heavily compensated than the rest - has a slope which corresponds to E_A.

Figure 4.6 presents Hall mobility curves which have been calculated from the data of Figure 4.5. Clearly, $\mu_c > \mu_a > \mu_b$. Figure 4.7 presents the same information, but also includes two additional curves for the b and c axes. The slopes of the Hall mobility curves of Komiya, Masumoto and Fan[4] are also indicated. There is about at 10% variation in the slopes of the drafted straight lines between samples with the same current axis (including the samples
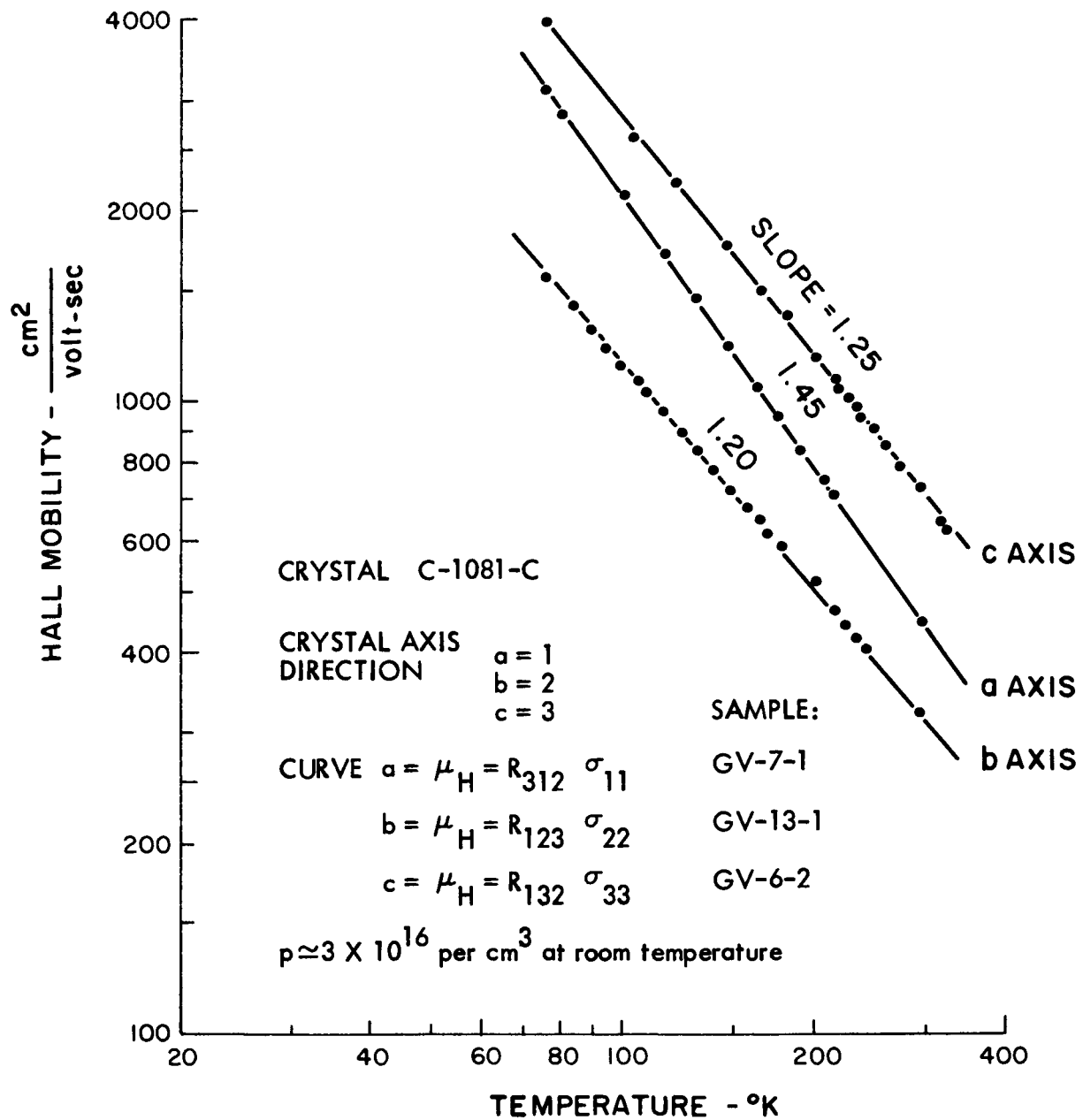
Fig. 4.6 Hall Mobilities of Undoped p-type ZnSb
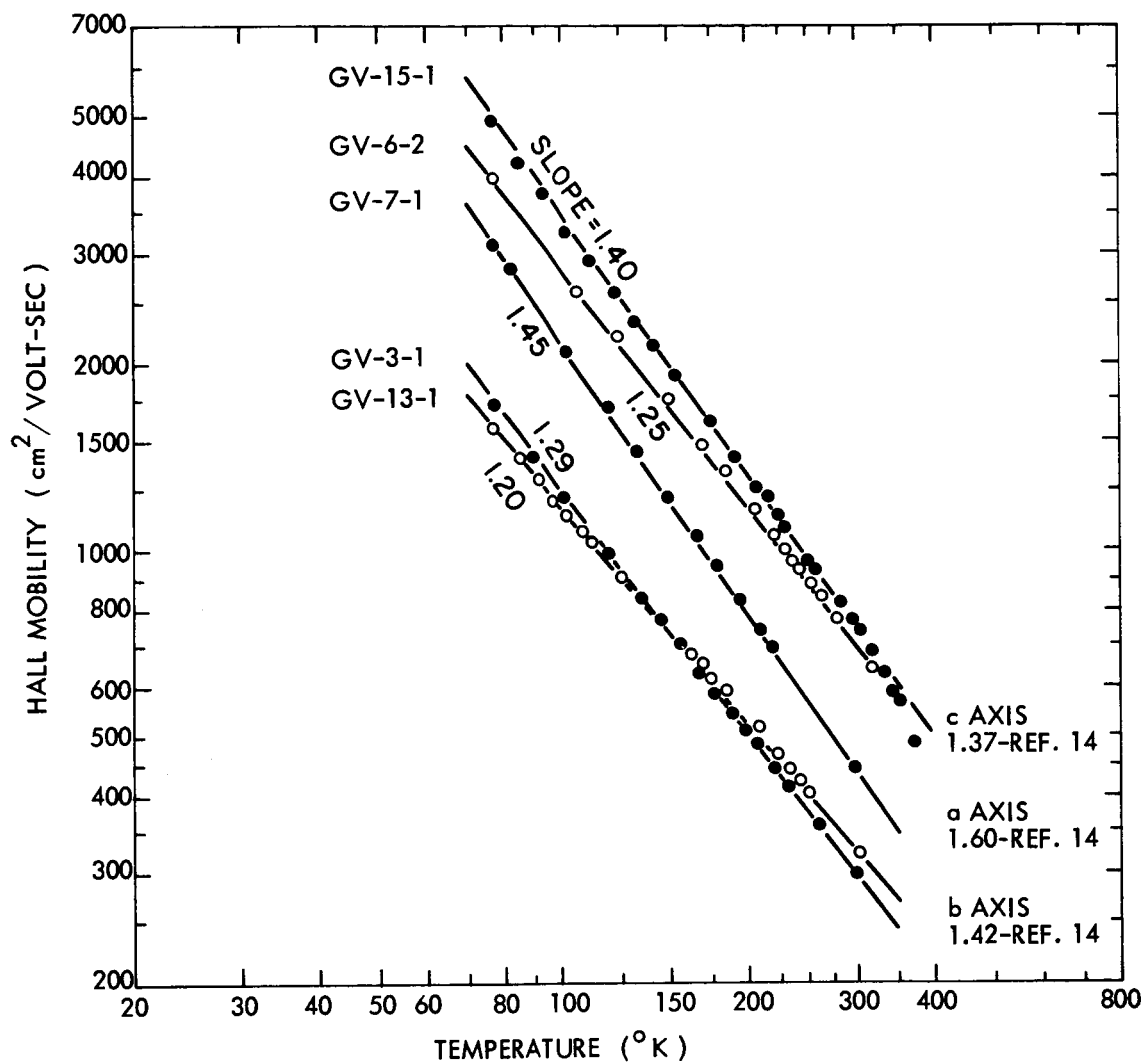
Fig. 4.7 Hall Mobilities vs. Temperature
Undoped p - Type Zn Sb

of ref. 4). The small table included on Figure 4.7 indicates that this variation can be correlated with the apparent density of acceptors. At higher hole concentrations, a bit more ionized impurity - charge carrier scattering is present, especially near 77.3°K. This decreases the observed mobility in the low temperature region. The experimental temperature range (77 to 300°K) has a limited geometrical length on the abscissa of the mobility plot. The data points can, therefore, be fit fairly well with straight lines - but these straight lines have decreased slopes.

The results presented on Figures 4.6 and 4.7 indicate that lattice scattering is the dominant charge carrier scattering mechanism in undoped ZnSb

The dates of measurement are included on Figure 4.7. They seem to indicate that, with the exception of sample GV-13-1, the hole concentration in crystal C-1081-C (removed from the crystal growth furnace on 7-10-64) was slowly decreasing with time. The crystal may have been recovering after growth ($T_{ambient}$ = 425°C) in the manner discussed in Section 4.2.

4.4.3 Measurements on Copper Doped ZnSb

Figures 4.8 and 4.9 present results for crystal C-1078-C, which had a hole concentration of about 4×10^{17} cm^{-3}. The Hall curves show a slight slope - corresponding to an apparent activation energy of 0.9×10^{-3} ev. This probably does not represent a single energy level activation process. The doping level is high enough so that the discrete acceptor energy level may have dispersed into a band of levels of different energies[16]. This is especially true for crystal C-1075-B ($p \simeq 1.1 \times 10^{19}$ cm^{-3}), which is shown by Figure 4.10. For this crystal, the Hall coefficient appears to be independent of temperature in the range of 77.3 to 325°K.

The Hall mobility curves, Figure 4.9 and 4.11, indicate that ionized impurity
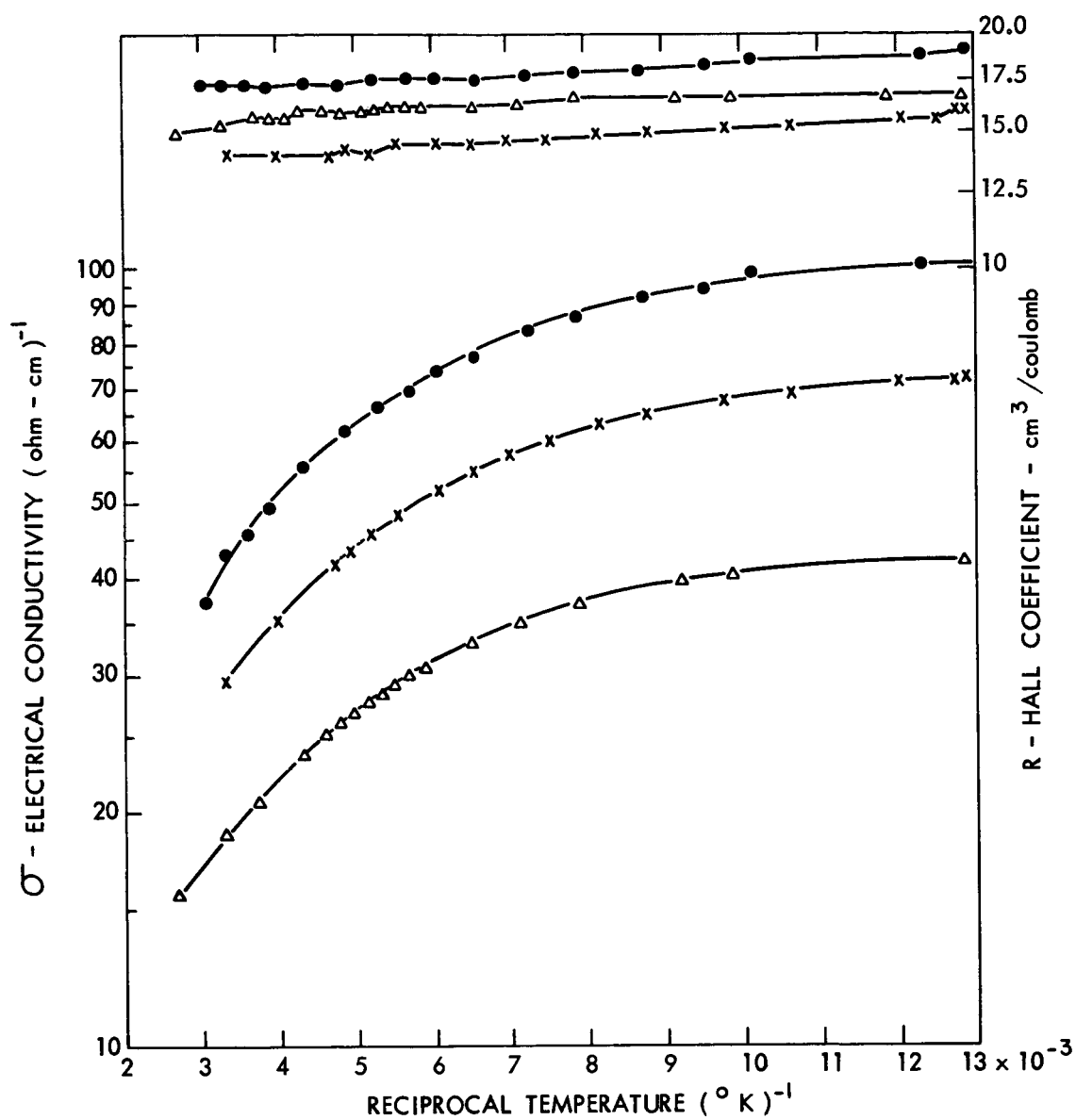
Fig. 4.8 Hall Coefficient and Electrical Conductivity
vs 1/T Copper Doped p-Type ZnSb
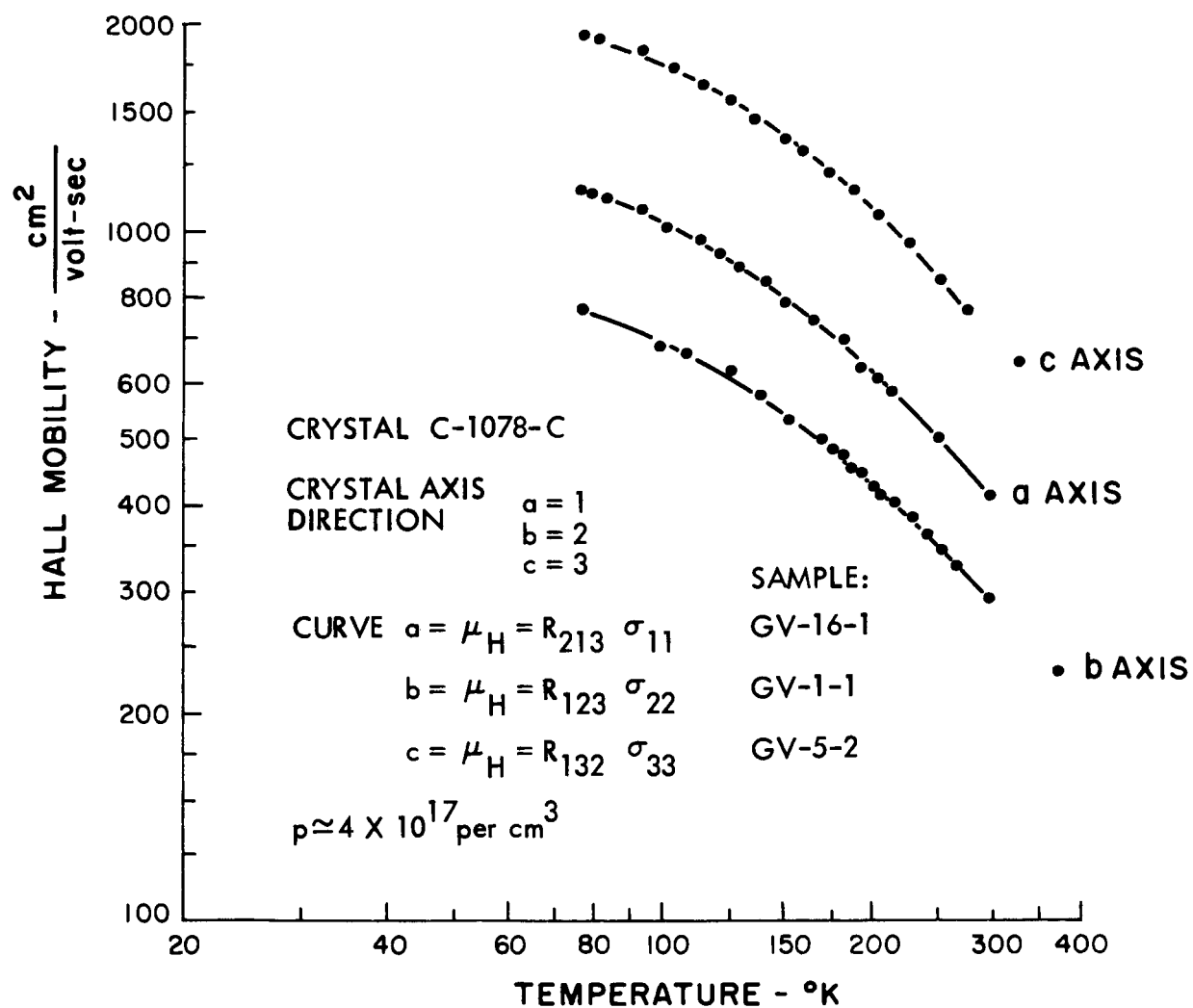
Fig. 4.9 Hall Mobilities as a function of Temperature
p-type ZnSb-Copper Doped
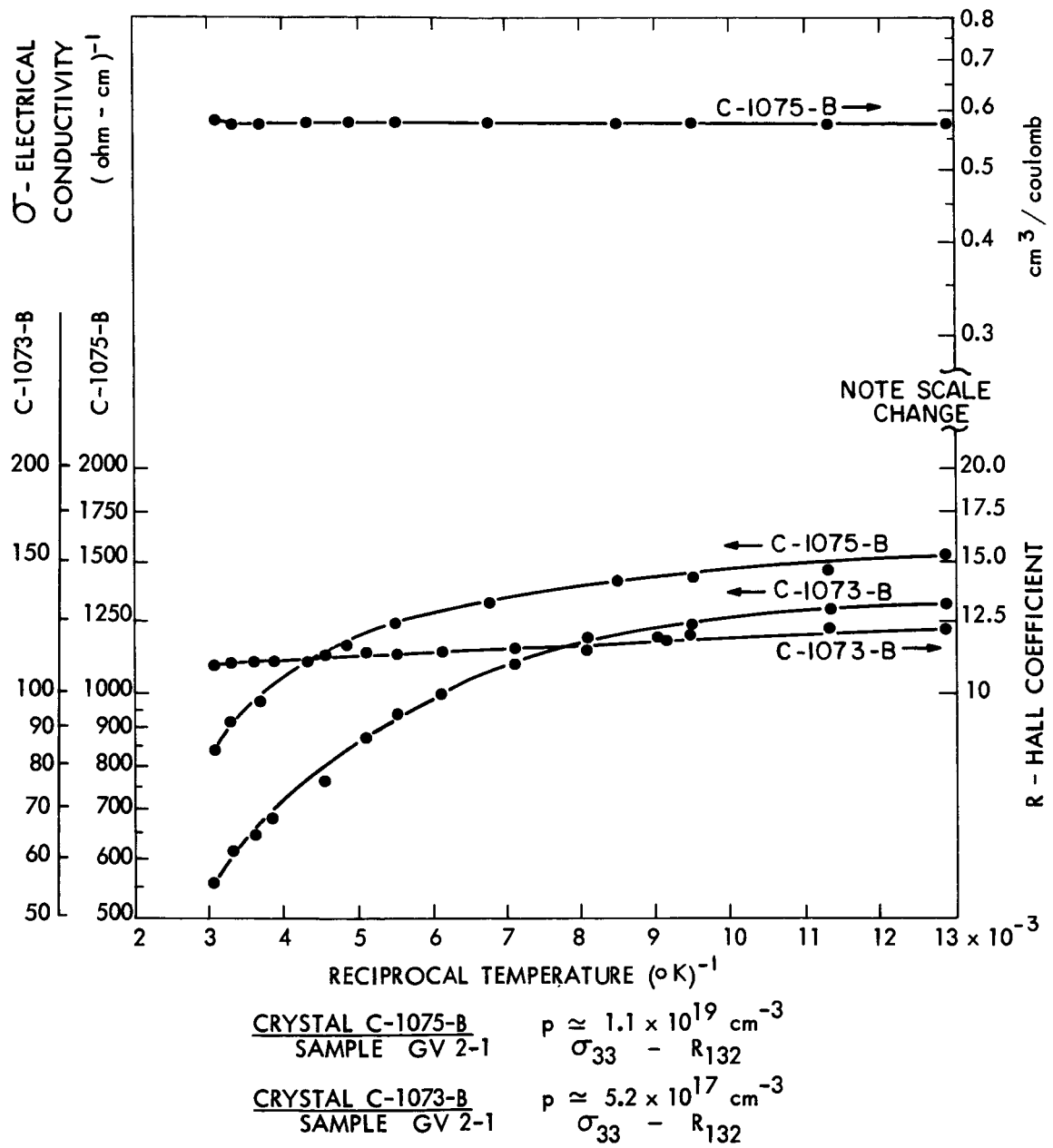
Fig. 4.10 Hall Coefficient and Electrical Conductivity
vs 1/T Copper Doped p-Type ZnSb
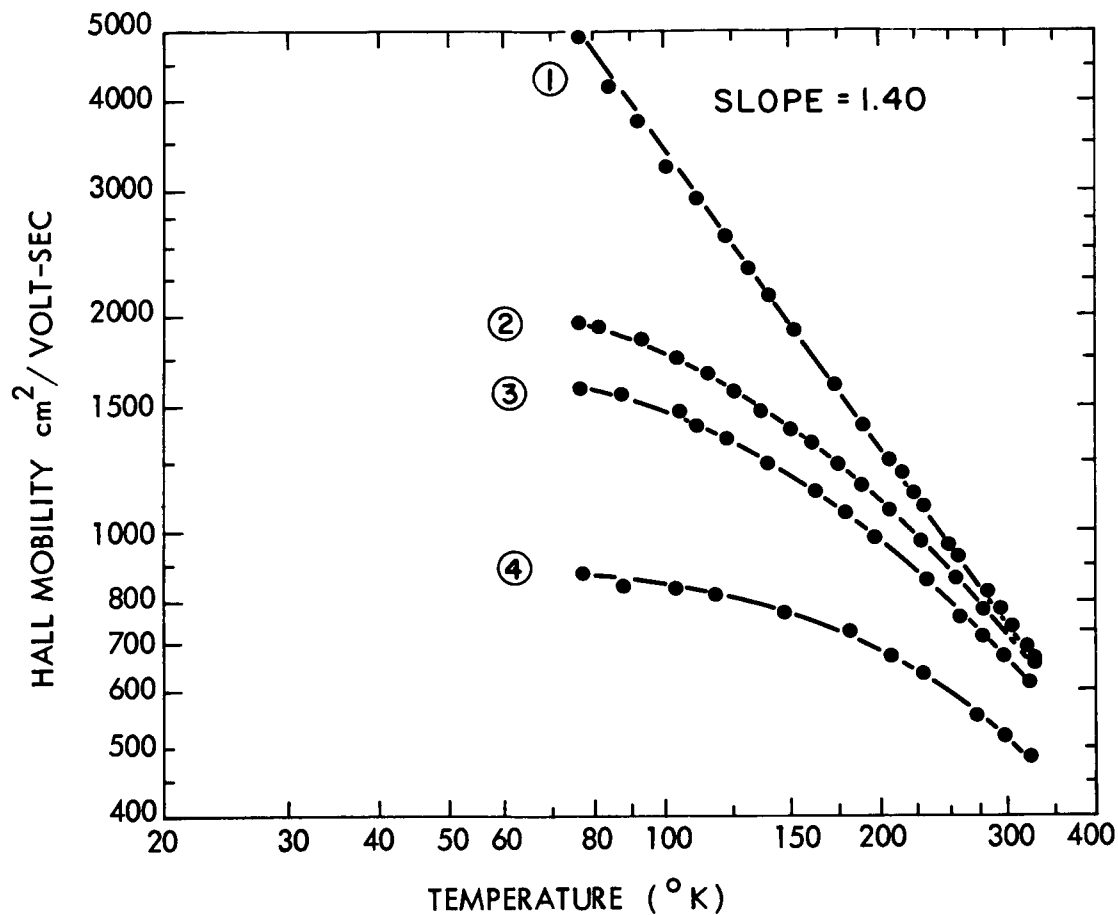
ALL CURVES: $\mu_H = \sigma_{33}\,R_{132}$

CURVE:		CRYSTAL		SAMPLE		
①	CRYSTAL	C-1081-C	SAMPLE	GV-15-1	$p \simeq 2 \times 10^{16}\,cm^{-3}$	
②	"	C-1078-C	"	GV-5-2	3.3×10^{17}	
③	"	C-1073-B	"	GV-2-1	5.2×10^{17}	
④	"	C-1075-B	"	GV-2-1	1.1×10^{19}	

Fig. 4.11   Comparison of Temperature Variations
of Hall Mobilities at Several Doping Levels

scattering is important at low temperatures. The most lightly doped crystal, C-1078-C, is seen to have just about the same room temperature Hall mobility as the undoped crystal, C-1081-C (Figure 4.11). It is also interesting to note that the anisotropy in the Hall mobilities of crystal C-1078-C (Figure 4.9) is just about independent of temperature.

4.5 ANISOTROPY OF THE HALL COEFFICIENT

4.5.1 Introduction

There are three possible independent Hall coefficients in a crystal which has orthorhombic symmetry. These are:

$$R_{123} = - R_{213}$$
$$R_{312} = - R_{132}$$
$$R_{231} = - R_{321}$$

The indicated equalities are those which are required by Onsager symmetry. Any experimentally observed anisotropy between these Hall coefficients must be accounted for in terms of the band structure and charge carrier scattering models which are assumed for p-type ZnSb. Consequently, it is important to experimentally determine these Hall coefficients.

4.5.2 Measurements on Undoped P-Type ZnSb

The measurements of Kot and Kretsu[1] on undoped ZnSb ($p \sim 5 \times 10^{16}$ cm^{-3}) indicate that as much as a 50% anisotropy might be present in the Hall co-efficients (refer to their Figure 2). The observations of this work - presented in Figure 4.5 - show a similar variation in the measured Hall coefficients. How-ever, the indicated 50% difference between R_{132} and R_{321} is as large as the 50% difference in two different determinations of R_{132} (samples GV-6-2 and 15-1). This illustrates the difficulty involved in drawing conclusions about the

anisotropies in any of the galvanomagnetic coefficients from measurements on undoped crystals. Unless the measurement samples have exactly the same thermal histories, the carrier precipitation phenomenum, which was discussed in Section 4.2, can lead to significant variations in hole concentration between sample bars cut from the same, homogeneous portion of an undoped crystal. For this reason, data taken on undoped p-type crystals is difficult to interpret. In fact, the Kot and Kretsu[1] paper is the only published account of the probable anisotropies in any transport parameter that directly depends on the electrical carrier concentration.

4.5.3 Measurements on Copper Doped Crystal C-1078-C

Hall coefficients were measured along with the magnetoresistance effect in a number of galvanomagnetic samples cut from crystal C-1078-C. This sample had a hole concentration ($p \simeq 1/Rq$) of about 4×10^{17} cm^{-3} at room temperature. Thus, the explicitly introduced acceptor doping level was 15 to 20 times higher than the residual acceptor concentration level in undoped crystals. As a result, carrier precipitation effects (Section 4.2) could cause only a maximum of 5 to 7% change in the net hole concentration. The average results which were obtained are presented in Table 4.2.

TABLE 4.2

HALL COEFFICIENTS AT $p \sim 4 \times 10^{17}$ cm^{-3}

Crystal C-1078-C

300°K

R_{123} (R_{231}) = 14.1 $\pm$ 1 cm^3/coulomb   (4 samples)

R_{132} (R_{312}) = 16.3 $\pm$ 1   (6 samples)

R_{231} (R_{321}) = 13.9   (1 sample)

<u>77.3°K</u>

$$R_{123} \quad (R_{231}) \quad = \quad 15.7 \pm 1 \quad cm^3/coulomb \quad \text{(4 samples)}$$

$$R_{132} \quad (R_{312}) \quad = \quad 18.4 \pm 1.5 \quad \text{(6 samples)}$$

$$R_{231} \quad (R_{321}) \quad = \quad 16.6 \quad \text{(1 sample)}$$

The approximate scatter in the measurement results is indicated by the given

limits. Data for R_{ijk} and R_{jik} were averaged together. The a.c. measurement

system indicates only the magnitude of a galvanomagnetic voltage – not the sign.

The results of Table 4.2 indicate that the Hall coefficient of p-type ZnSb

is isotropic. Kawasaki and Tanaka[15] have obtained the same result for p-type

CdSb.

4.5.4 Measurements on More Heavily Doped Crystals

The following experiments were explicitly designed to more carefully

determine the degree of anisotropy between the Hall coefficients of p-type ZnSb.

Single crystal bars were cut in the form of rectangular parallelepipeds.

These bars had the "2" and "3" crystallographic directions as electric current

axes. Hall probes were mounted on each of the two pairs of longitudinal faces

of a bar. With the current axis mounted vertically, the sample could be rotated

so that two independent Hall coefficients could be measured at one time. In

this way, R_{123} and R_{321} were measured on the "2" axis bar and R_{231} and R_{132}

on the "3" axis bar. Onsager symmetry requires that R_{321} and R_{231} in absolute

magnitude. Hence, all three independent Hall coefficients were measured and

a homogeneity check between the two sample bars was obtained. The observed

results are presented in the tables which follow.

TABLE 4.3

HALL COEFFICIENTS AT $p \sim 5.5 \times 10^{17}$ cm^{-3}

Crystal C-1073-B

<u>300°K</u>

R_{123} = 11.9 cm^3/coulomb

sample GV-1-1

R_{321} = 10.5

R_{231} = 11.6

sample GV-2-1

R_{132} = 11.0

<u>77.3°K</u>

R_{123} = 12.9

sample GV-1-1

R_{321} = 11.4

R_{231} = 13.2

sample GV-2-1

R_{132} = 13.3

TABLE 4.4

HALL COEFFICIENTS AT $p \sim 1.1 \times 10^{19}$ cm^{-3}

Crystal C-1075-B

<u>300°K</u>

R_{123} = 0.594 cm^3/coulomb

sample GV-1-1

R_{321} = 0.576

R_{231} = 0.550

sample GV-2-1

R_{132} = 0.568

<u>77.3°K</u>

R_{123} = 0.609 cm^3/coulomb

sample GV-1-1

R_{321} = 0.593

R_{231} = 0.560

sample GV-2-1

R_{132} = 0.570

Except for the approximately 10% low value for R_{321} measured on crystal C-1073-B sample GV-1-1, the relative scatter in the above results is $\pm$ 4%. It is concluded that the Hall effect is isotropic in p-type ZnSb. It is interesting to note that this isotropy prevails even though there is appreciable ionized impurity - charge carrier scattering present at the lower temperature. This point is used in the discussion which appears in Chapter 5.

4.6 MAGNETIC FIELD DEPENDENCES OF THE HALL AND MAGNETORESISTANCE COEFFICIENTS

4.6.1 Introduction

In order to determine the region of applicability of the low magnetic field solution of the Boltzmann equation (Appendix 2), it is important to check the magnetic field dependences of the measured effects.

4.6.2 Hall Effect

The Hall effect has been measured in undoped ($p \sim 3 \times 10^{16}$ cm^{-3}) and copper doped ($p \sim 4 \times 10^{17}$ cm^{-3}, $p \sim 5.5 \times 10^{17}$ and $p \sim 1.1 \times 10^{19}$ cm^{-3}) ZnSb at room temperature and at liquid nitrogen temperature for magnetic fields between 250 gauss and 12.5 kilogauss. The measured Hall voltages were linear in B, showing only an apparently non-systematic $\pm$ 2 percent maximum deviation from a linear field dependence. These fluctuations are within the experimental accuracy of the measurement. Typical results are shown in Figure 4.12. Undoped crystals - having the highest mobilities - would be expected to be the first to show high field departures from a linear behavior.

4.6.3 Magnetoresistance

Magnetoresistance has been measured in the undoped and the lightly copper doped samples referred to above at liquid nitrogen temperature for magnetic field densities between 8 and 12.5 kg. The magnetoresistance follows a simple B^2 magnetic field dependence within $\pm$ 5 percent. This is within the experimental
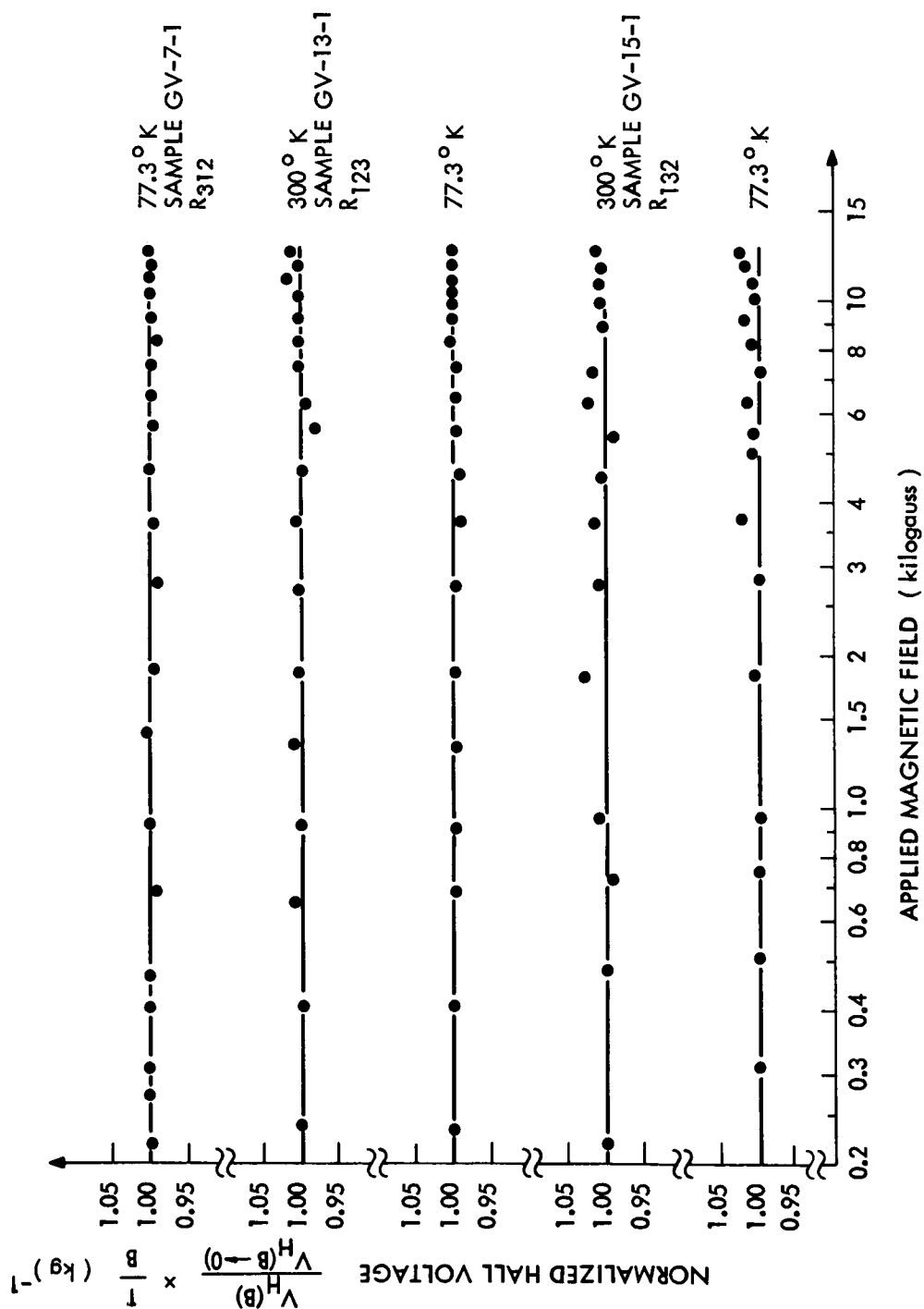
Fig. 4.12 Typical Field Dependences of the
Measured Hall Voltages

accuracy of the measurement. No systematic deviations from a B^2 dependence are observed in the magnetic field range of 8 to 12.5 kg. Figure 4.16 shows the field dependence of the magnetoresistance voltage of crystal C-1081-C (undoped) sample GV-15-1. It is seen to be quadratic in B from 1.00 to 12.55 kg.

4.7 MAGNETORESISTANCE MEASUREMENTS ON P-TYPE ZnSb

4.7.1 Introduction

Magnetoresistance measurements are used as a method of exploring the symmetry of the valence band of ZnSb.

The galvanomagnetic measurement instrumentation has been described in Section 3.1.2. The 12 independent magnetoresistance coefficients to be measured are:

$$\rho_{1111} \quad \rho_{2211} \quad \rho_{3311} \quad \rho_{1212}$$
$$\rho_{1122} \quad \rho_{2222} \quad \rho_{3322} \quad \rho_{1313}$$
$$\rho_{1133} \quad \rho_{2233} \quad \rho_{3333} \quad \rho_{2323}$$

Four measurements on each of three bars are required to measure all 12 of these coefficients. For instance, by suitably changing the mounted position of the sample, ρ_{1111}, ρ_{1122}, ρ_{1133} and ρ_{2121} can be measured on one sample with the electric current along the <100> direction. ρ_{2121} is measured with "Hall effect" probes on the <010> faces of the sample as the magnetic field is moved about in the (001) plane of the sample.

The sample geometry which was used here has been described in Section 2.6.2 (and Figure 2.9) and the method of making electrical contacts described in Section 2.6.3. Figure 3.3 is a photograph of crystal C-1081-C, sample GV-15-1 mounted for measurements. The longitudinal homogeneity of the magnetoresistance samples was checked by measuring the Hall coefficient at two positions along the sample axis (Figure 2.9). Occasionally, a three point probe resistivity profile was

taken along the sample axis. These checks indicated that the sample which were used had axial variations in hole density of less than 3 to 5%.

No attempt was made to directly measure the planar Hall coefficients[17], ρ_{1212}, ρ_{1313}, and ρ_{2323}. The magnitudes of these coefficients are inferred from the usual type of magnetoresistance measurements on samples cut so that their current axis was not along a principal crystallographic direction. These are called "off-axis" samples in the following sections. This was done becuase the very small magnetoresistance of p-type ZnSb makes the detection of a magneto-resistance effect at "Hall probes" just about impossible with the measurement techniques used here.

At 12.5 kg, the electric field component which gives rise to the Hall voltage is roughly two orders of magnitude larger than the change in the longitudinal component of the electric field which is caused by the magnetoresistance. As a result, the slightest departures from ideal galvanomagnetic sample geometry will introduce a spurious Hall voltage component into the voltage measured at the magnetoresistance probes. In practice, the measured magnetoresistance voltage contains roughly an equal amount of spurious Hall voltage at 12.5 kg. By suitably averaging voltages measured for both directions of the magnetic field, the actual magnetoresistance voltage can be obtained. However, especially below 10 kg, this procedure can amount to taking the difference of two large numbers and can possibly introduce considerable error into the magnetoresistance results. The absolute accuracy of the magnetoresistance measurement, $\Delta\rho/\rho^\circ B^2$, is estimated to be between 5 percent and 10 percent, depending upon the numerical magnitudes involved.

The experimentally observed angular dependence (angle between $\vec{B}$ and $\vec{J}$) of the magnetoresistance is presented in the 17 separate figures which follow.

On these figures, brackets have been drawn that represent the total scatter
for all of the data points that correspond to a given angle between the magnetic
field and current axis of the sample. Except when the experimental points at a
given angle become too dense, horizontal hash marks locate the experimental value
of $\Delta\rho/\rho^\circ B^2$ for each magnetic field strength used. Data was usually taken with
magnetic flux densities between 8 and 12.5 kilogauss. Figure 4.16 presents
the observed magnetoresistance voltage of an undoped sample over the magnetic
field range of 1.0 to 12.55 kg.

The scatter of the individual data points within a given bracket seens to
bear no correlation to magnetic field strength. Hence, it must be concluded
that the observed magnetoresistance is quadratic in magnetic field strength.
The scatter of the individual data points mainly arises from the fact that the
magnetoresistance effect is so small in ZnSb. For instance, at 77.3°K in a
12.55 kg magnetic field, the largest observed changes in resistance are 2.1
percent and 0.3 percent for the undoped and copper doped samples, respectively.

Extensive magnetoresistance measurements were made at 77.3°K only. At
room temperature, the resistance changes were of the order of 0.01% and less.
These were too small to measure accurately with the equipment which was used.

4.7.2 Magnetoresistance Measurements on Undoped P-Type ZnSb

Figures 4.13, 4.14 and 4.15 present magnetoresistance results for the
electric current directed along the <100>, <010> and <001> crystal axes,
respectively. These results are included to give a qualitative picture of
the angular symmetry of the magnetoresistance measurements in p-type ZnSb,
$p \sim 2 \times 10^{16}$ cm^{-3}.

The data which is presented indicates a longitudinal magnetoresistance
effect which is so small that it is reasonable to regard it as being residual.

$p \sim 1.1 \times 10^{16}$ cm^{-3} 77.3°K   Crystal C-1081-C   Sample GV-7-1 $\vec{B}$ Rotated in (001) Plane

Brackets Enclose Data Points For B = 12.50, 11.10, 9.36 kg.

Fig. 4.13   Magnetoresistance in Undoped P-Type ZnSb

$p \sim 2.3 \times 10^{16}$ cm^{-3} 77.3°K   Crystal C-1081-C   Sample GV-13-1 $\vec{B}$ Rotated in (100) Plane

Brackets Enclose Data Points For B = 12.50, 11.00, 10.00, 8.00, 7.00 kg.
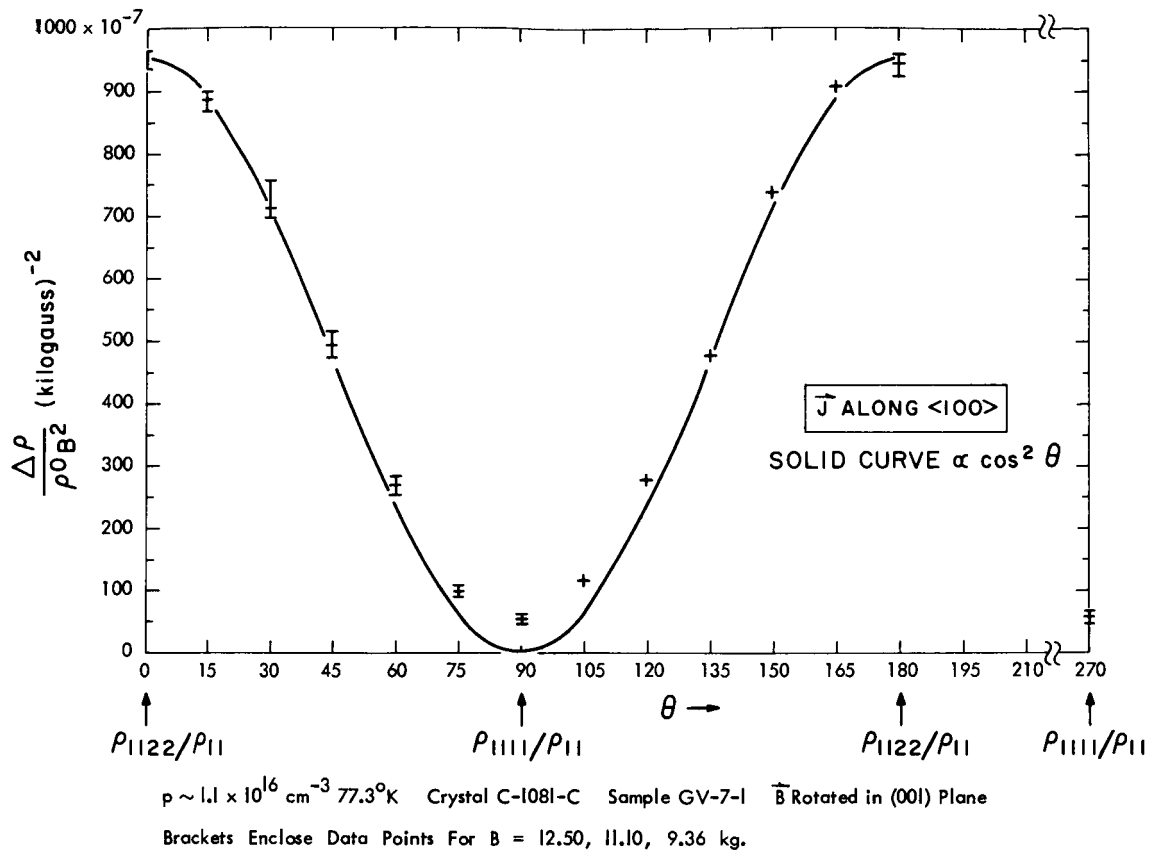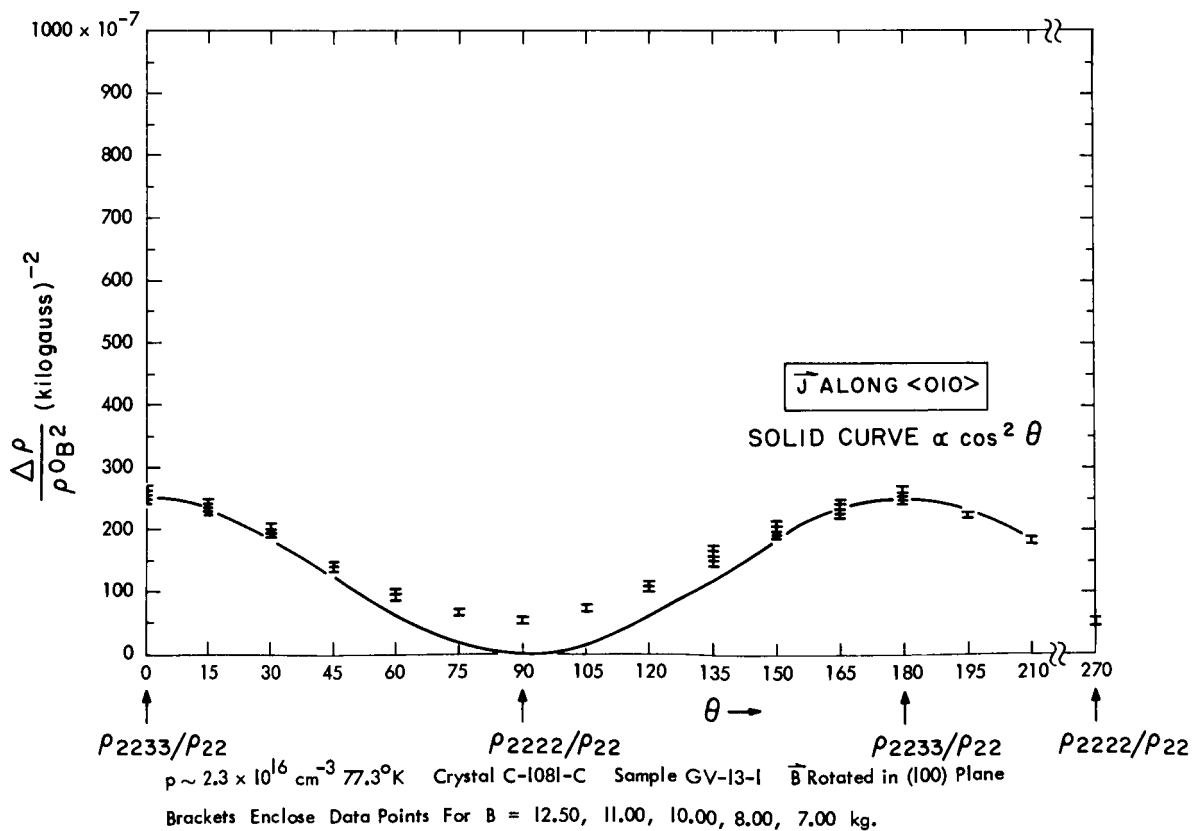
Fig. 4.14   Magnetoresistance in Undoped P-Type ZnSb
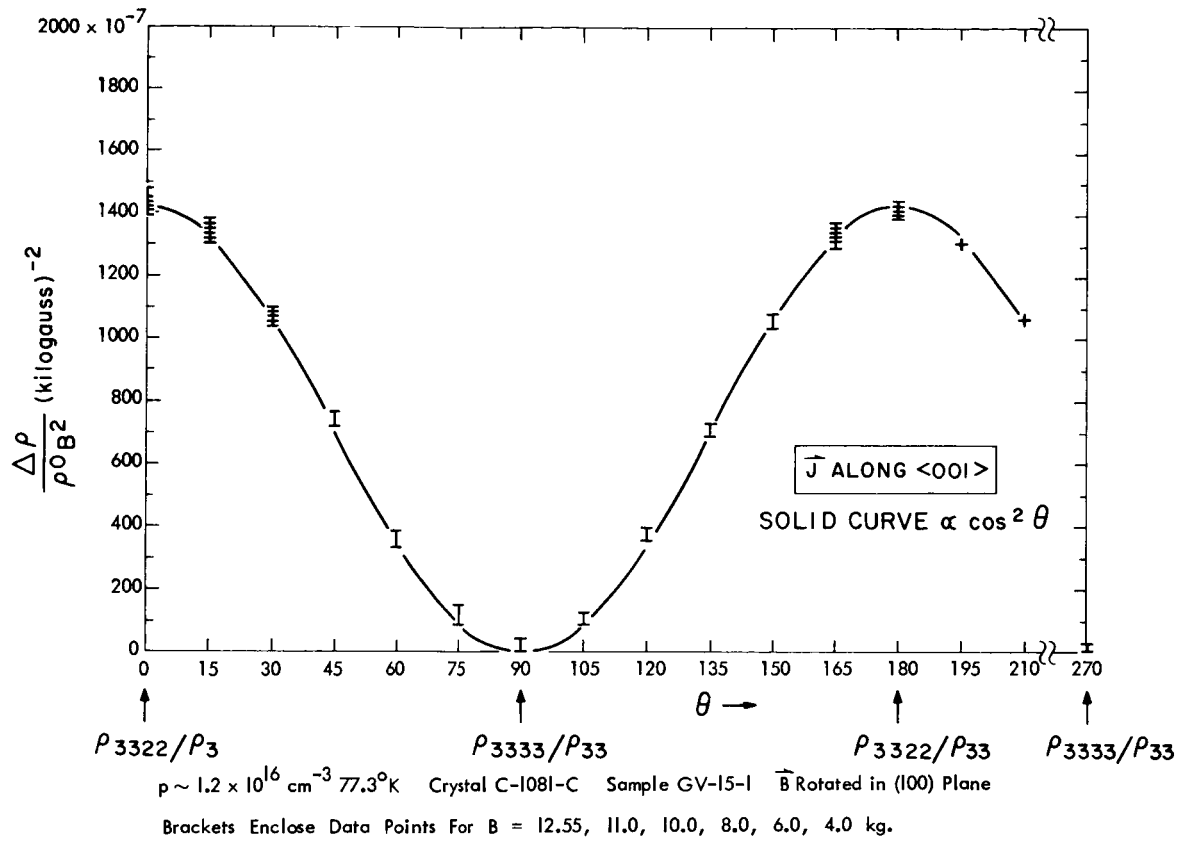
Fig. 4.15 Magnetoresistance in Undoped P-Type ZnSb

Fig. 4.16   Magnetic Field
            Dependence of the
            Magnetoresistance
            of an Undoped Sample
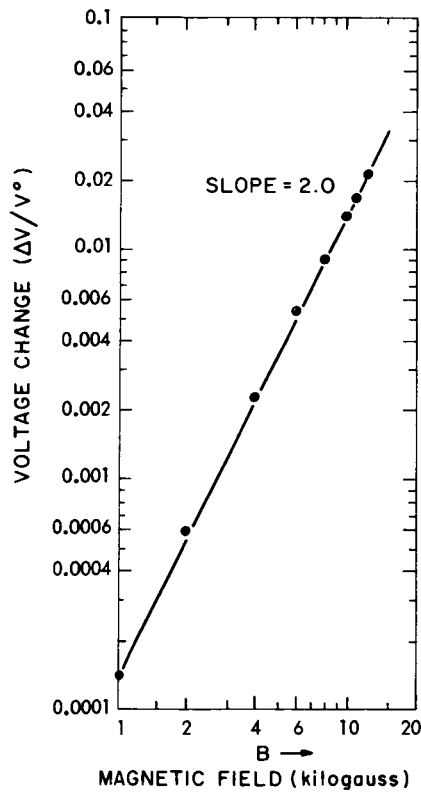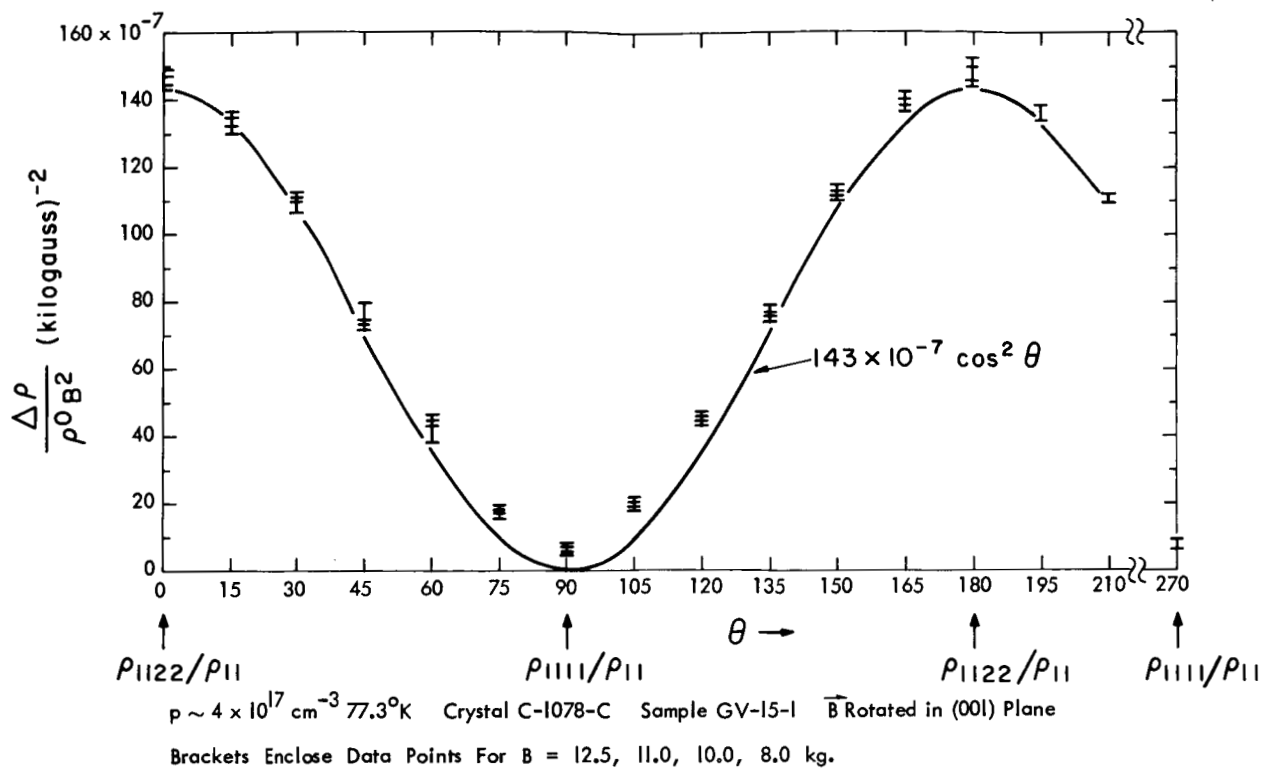
Fig. 4.17   Magnetoresistance in Copper Doped ZnSb
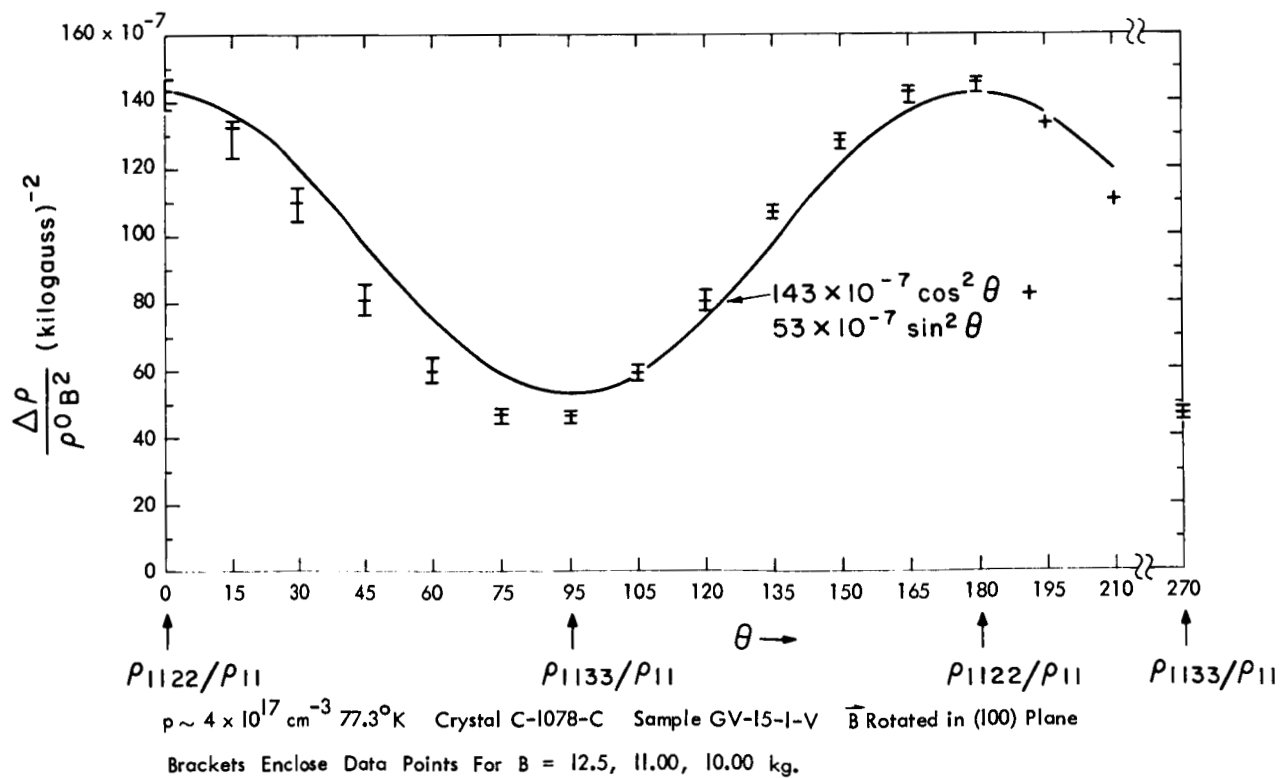
Fig. 4.18 Magnetoresistance in Copper Doped ZnSb
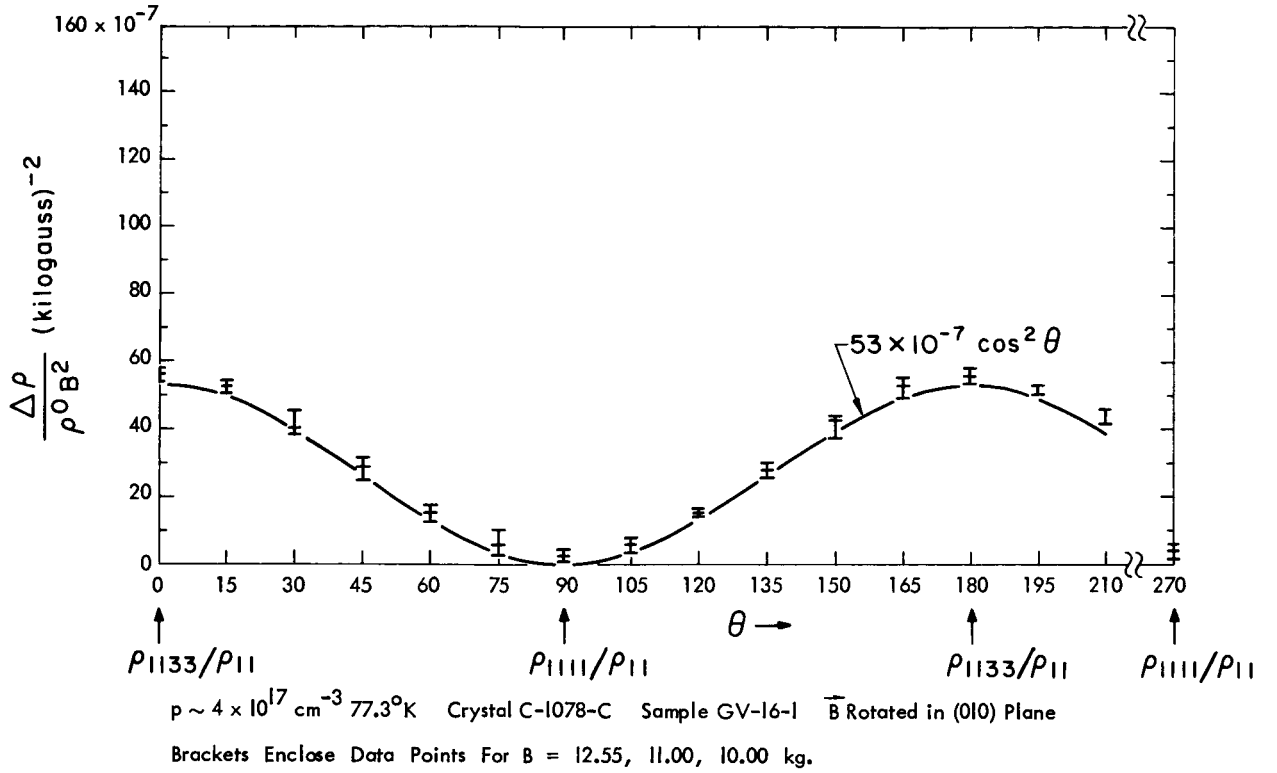
Fig. 4.19 Magnetoresistance in Copper Doped ZnSb

Fig. 4.20 Magnetoresistance in Copper Doped ZnSb

$p \sim 4 \times 10^{17} \, cm^{-3}$ 77.3 °K   Crystal C-1078-C   Sample GV-1-1 $\vec{B}$ Rotated in (100) Plane

Brackets Enclose Data Points For B = 12.5, 12.5, 10.5, 8.00 kg.
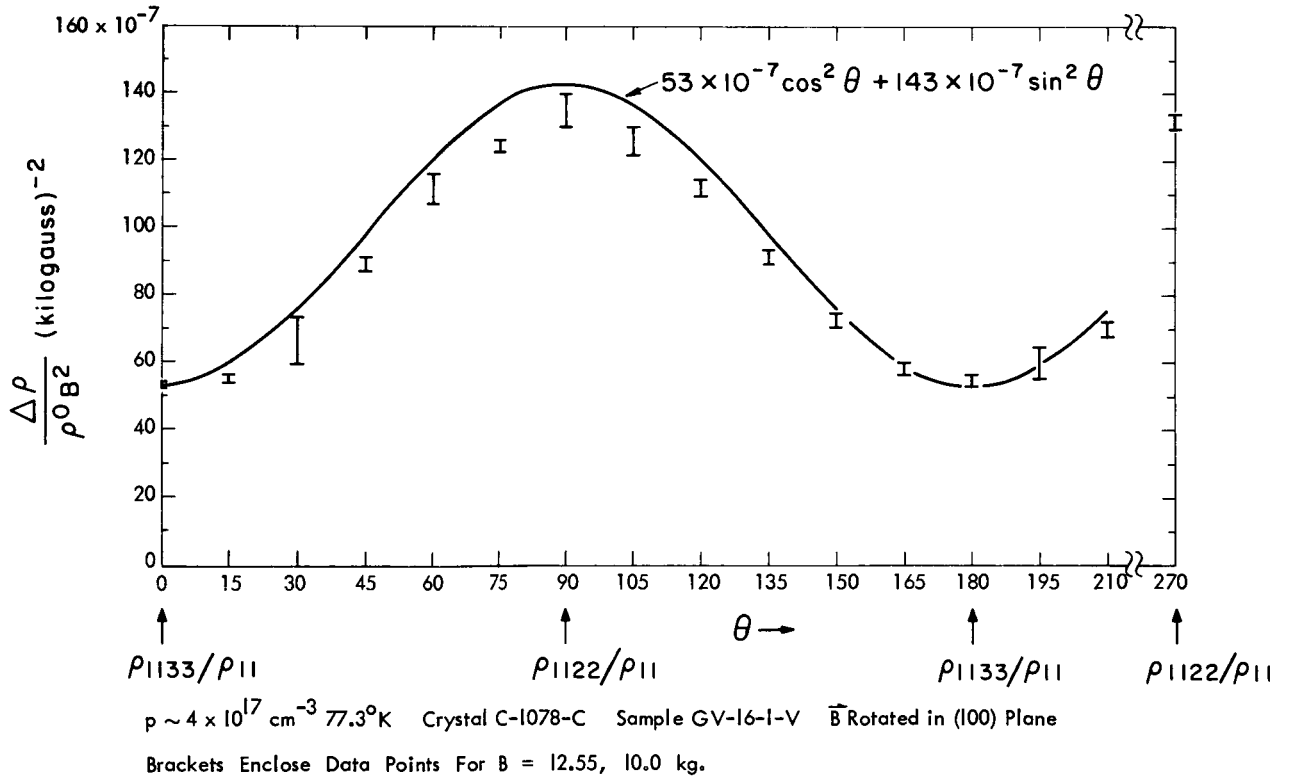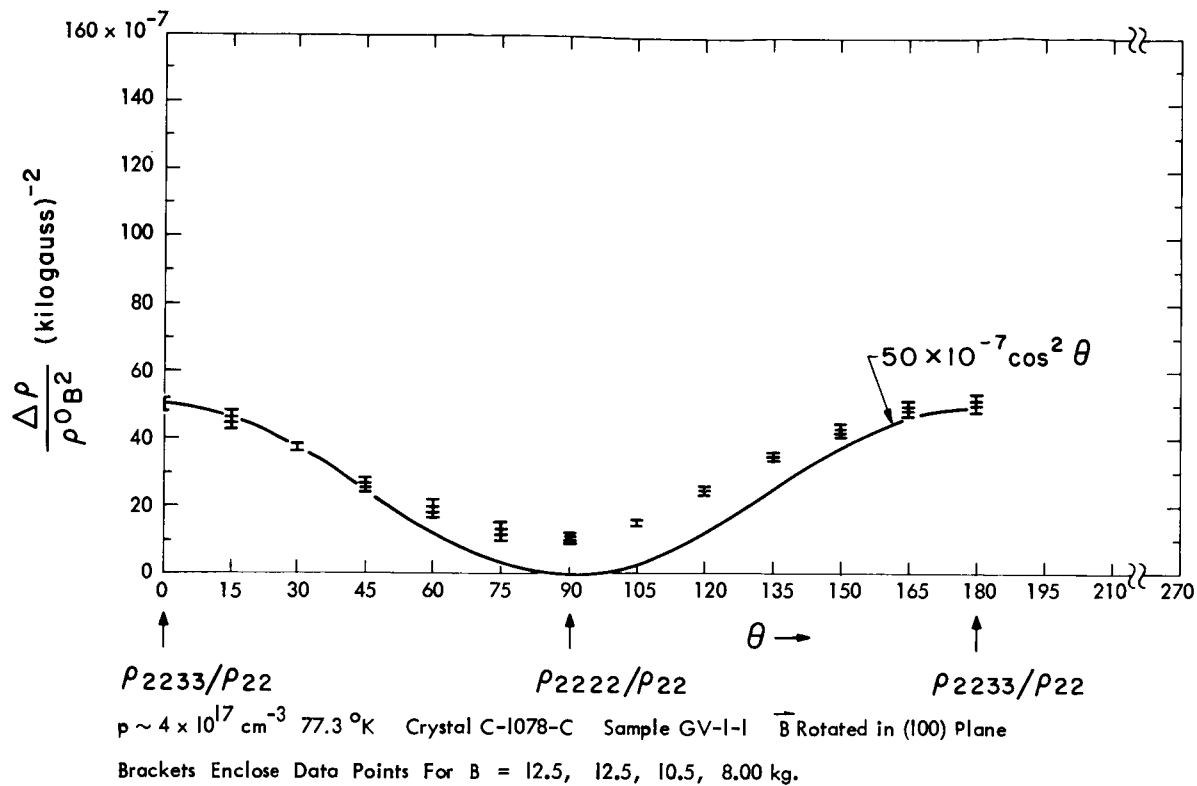
Fig. 4.21   Magnetoresistance in Copper Doped ZnSb

$p \sim 4 \times 10^{17} \, cm^{-3}$ 77.3 °K   Crystal C-1078-C   Sample GV-13-1 $\vec{B}$ Rotated in (100) Plane

Brackets Enclose Data Points For B = 12.55, 11.00, 10.00 kg. This Sample Chemically Etched Surfaces
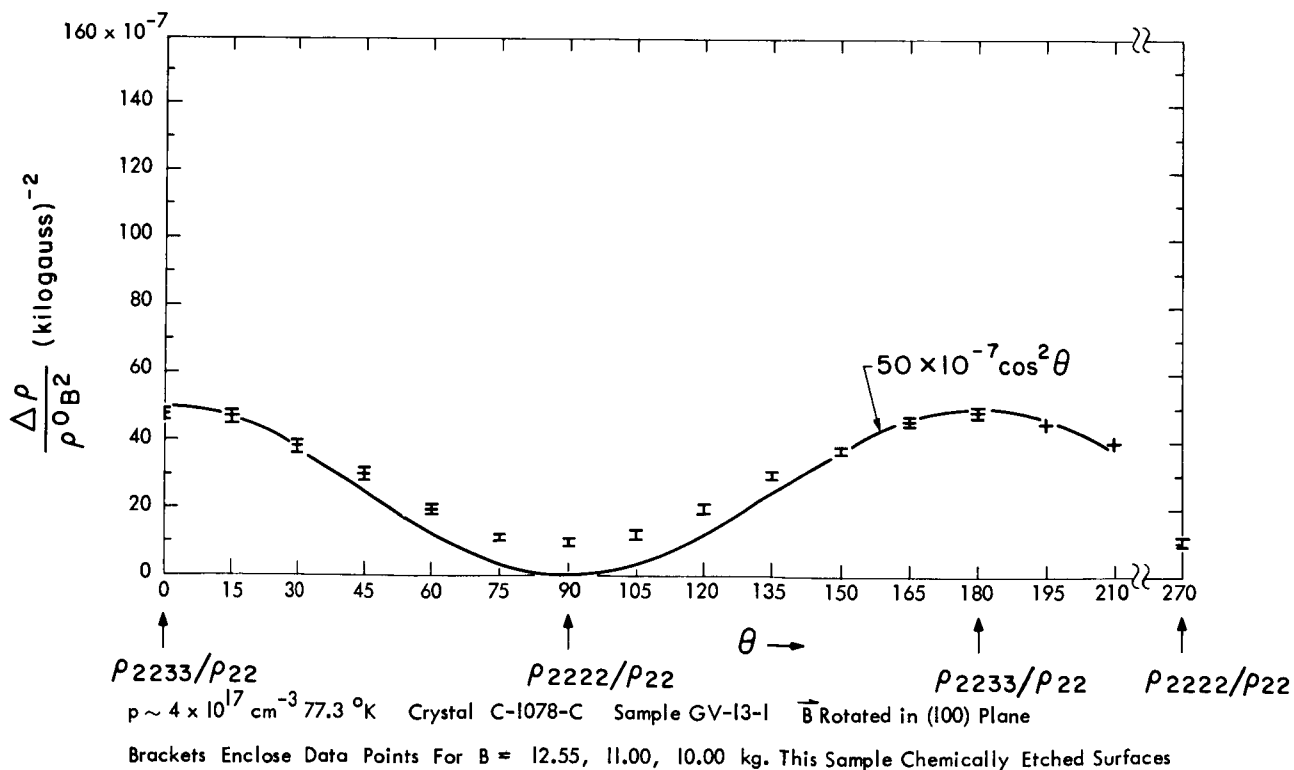
Fig. 4.22   Magnetoresistance in Copper Doped ZnSb
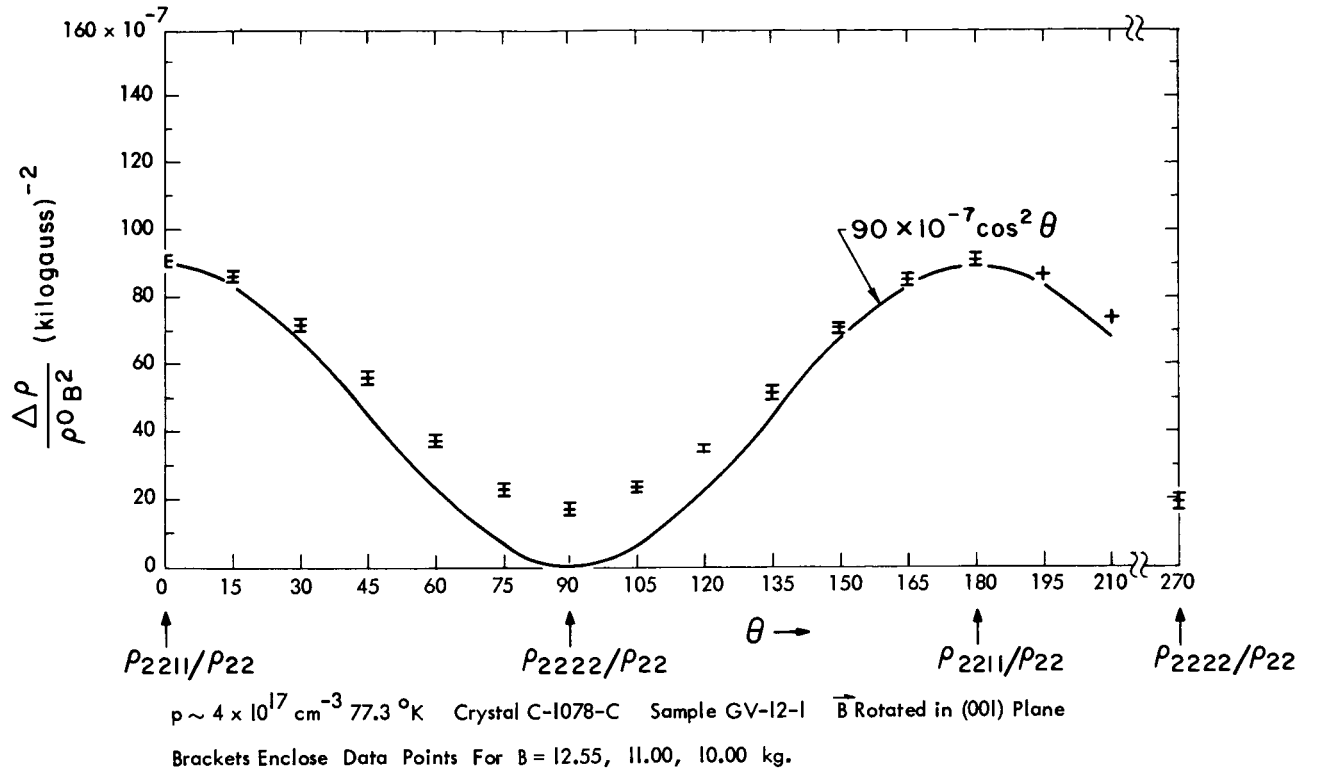
Fig. 4.23   Magnetoresistance in Copper Doped ZnSb
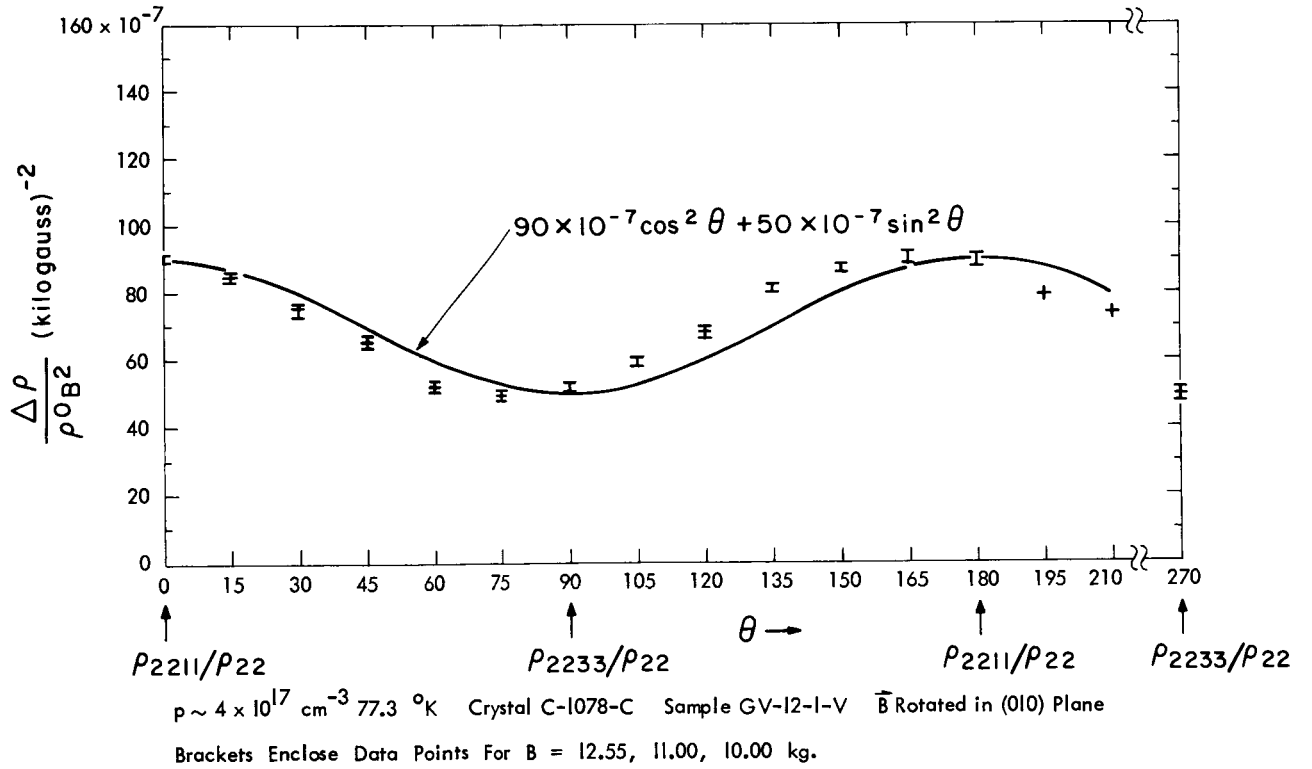
Fig. 4.24   Magnetoresistance in Copper Doped ZnSb
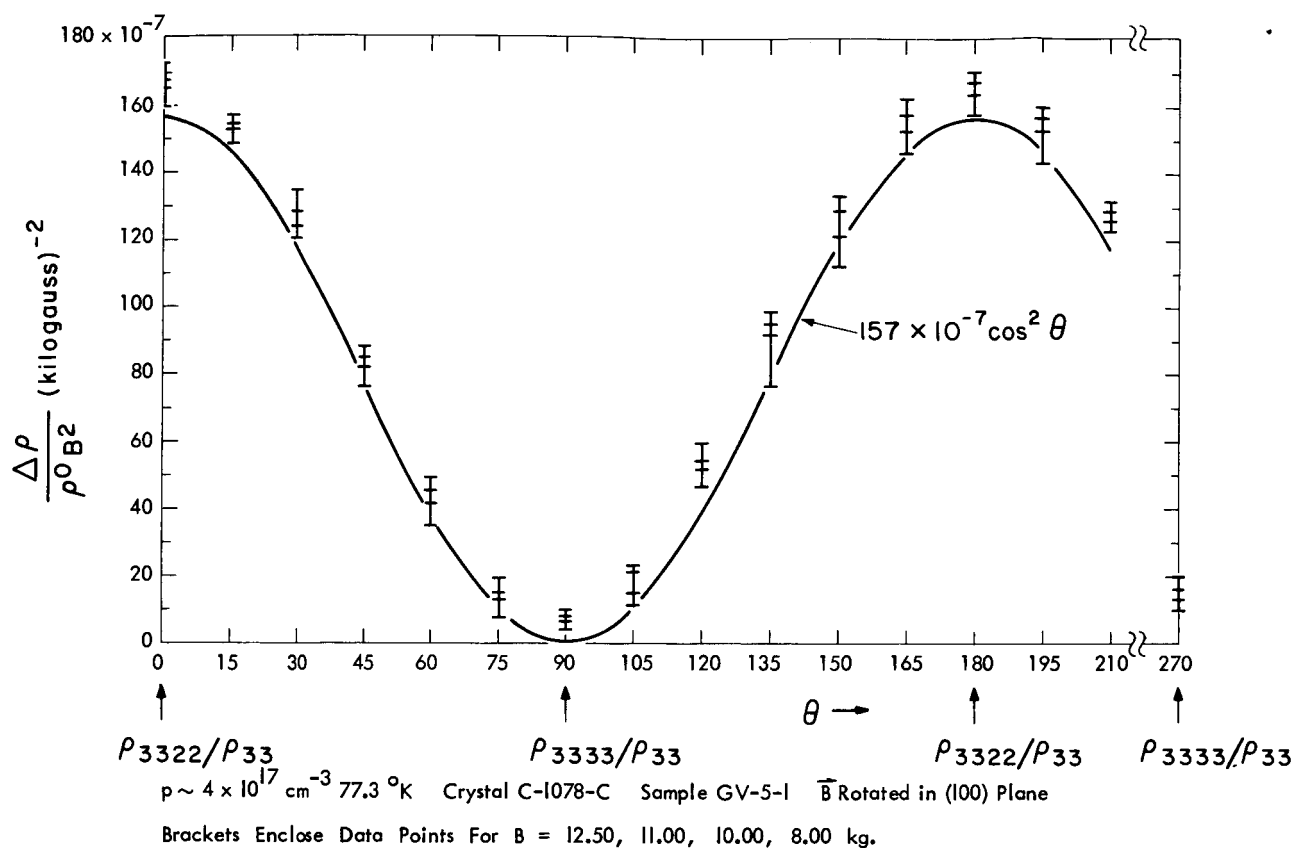
Fig. 4.25   Magnetoresistance in Copper Doped ZnSb
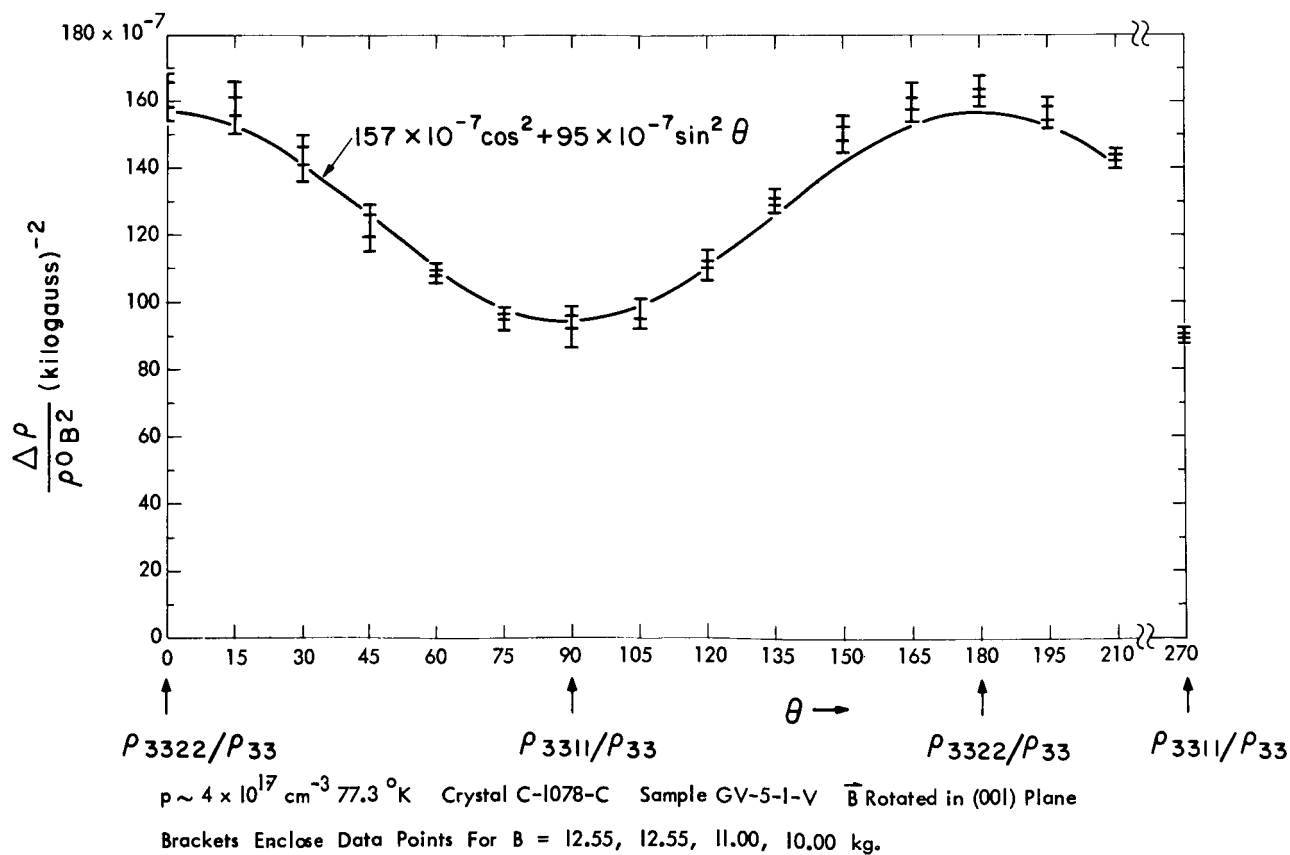
Fig. 4.26   Magnetoresistance in Copper Doped ZnSb
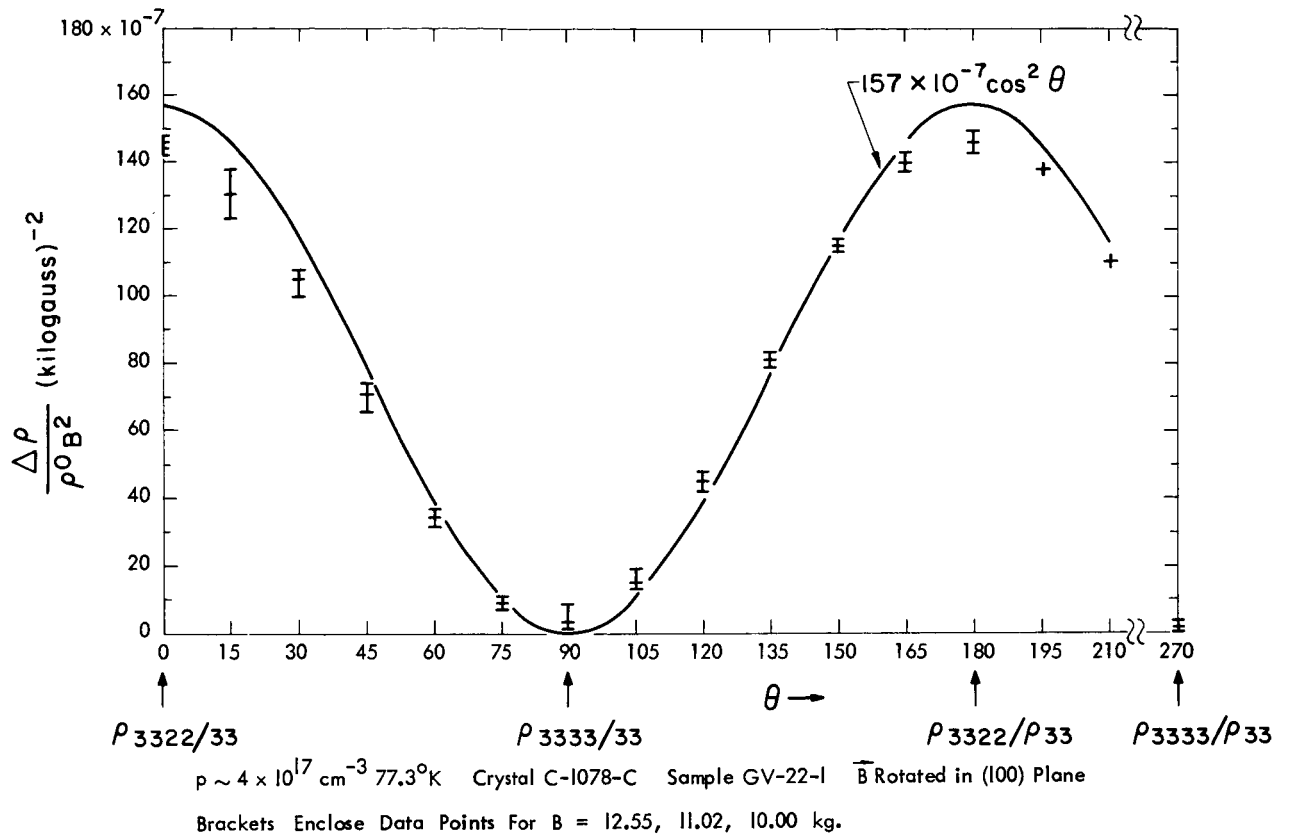
Fig. 4.27   Magnetoresistance in Copper Doped ZnSb
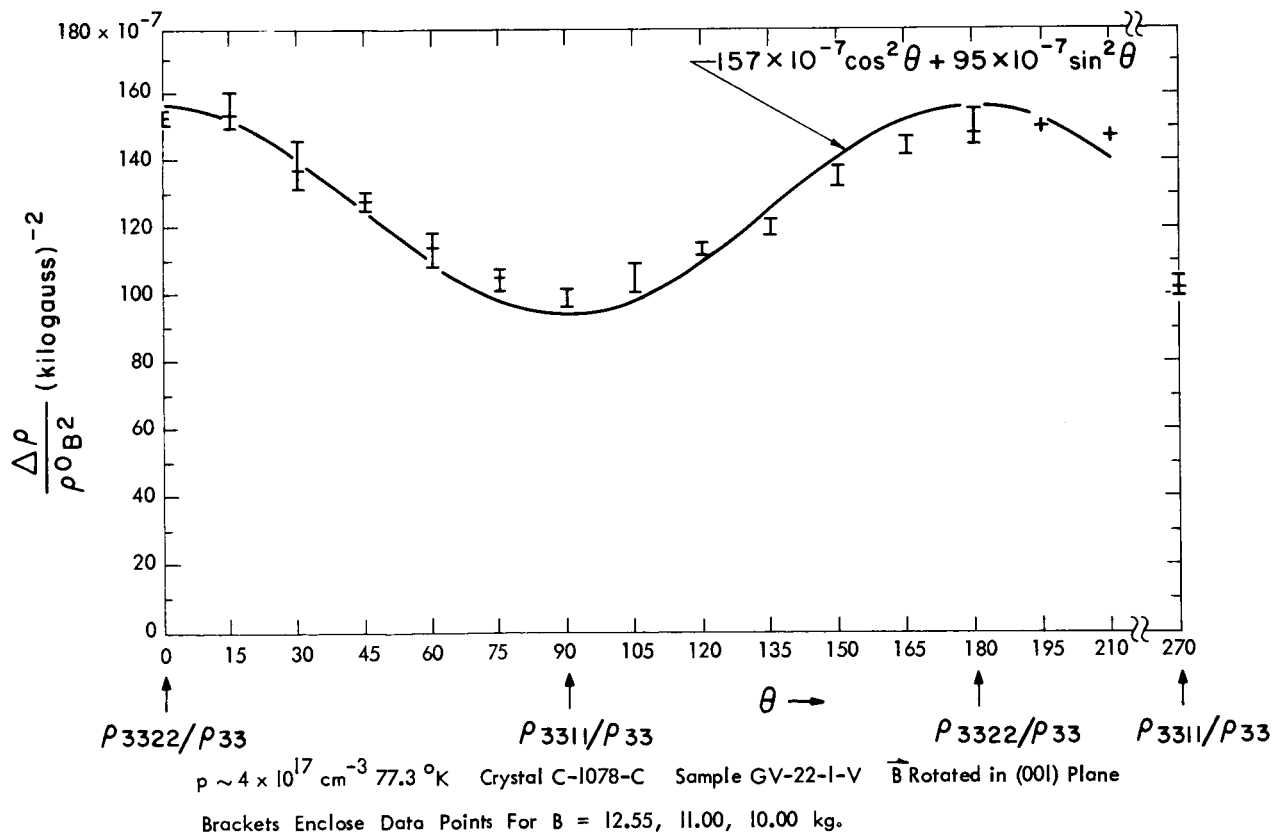
Fig. 4.28   Magnetoresistance in Copper ZnSb

$$\frac{\Delta\rho}{\rho^0 B^2} \ (kilogauss)^{-2}$$

<001> IS NORMAL TO
DIAGRAM WHEN θ = 0

$\overrightarrow{B}$ DIRECTED
ALONG <001>

$\overrightarrow{B}$ PARALLEL TO $\overrightarrow{J}$

$\overrightarrow{B}$ DIRECTED
ALONG <001>

$\overrightarrow{B}$ PARALLEL
TO $\overrightarrow{J}$
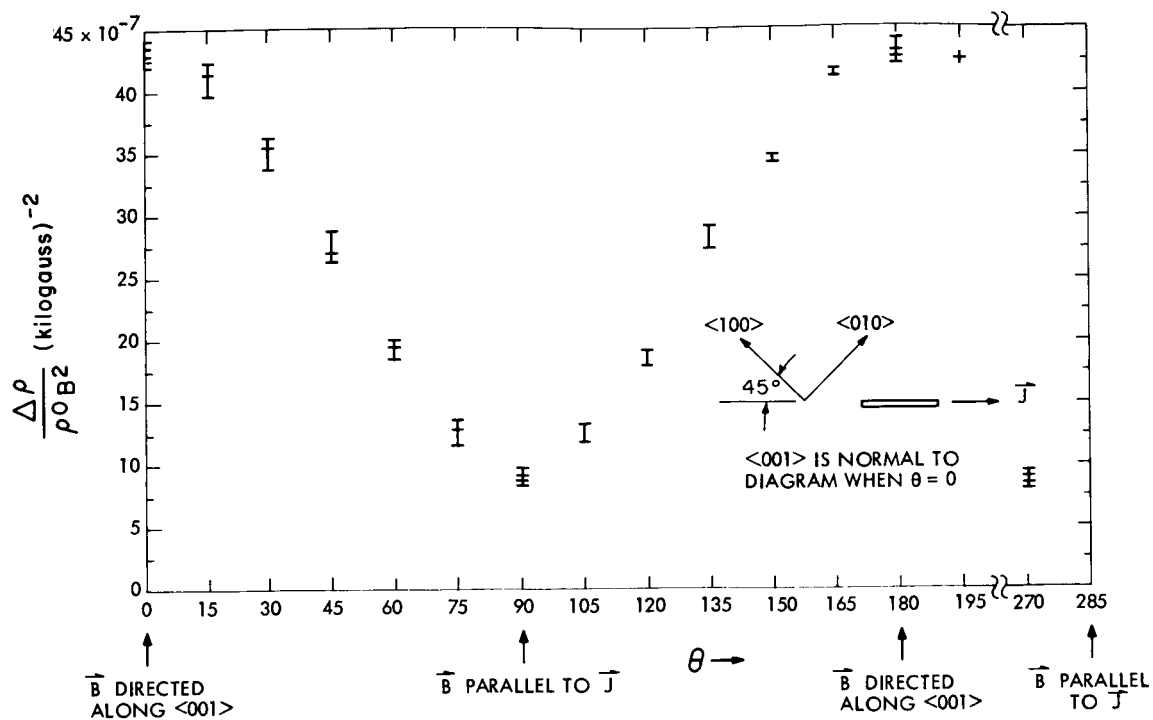
$p \sim 4 \times 10^{17} \ cm^{-3} \ 77.3^\circ K$ Crystal C-1078-C   Sample GV-26-1

Brackets Enclose Data Points For B = 12.55, 12.55, 11.00, 10.00 kg.

Fig. 4.29   Magnetoresistance in Copper Doped ZnSb

$$\frac{\Delta\rho}{\rho^0 B^2} \ (kilogauss)^{-2}$$

[ENCLOSES DATA POINTS FOR SAMPLE GV – 24 – 1

] ENCLOSES DATA POINTS FOR SAMPLE GV – 24 – 1

<010> IS
NORMAL TO
DIAGRAM
WHEN θ = 0

GV – 25 –1

GV – 24 –1

$\overrightarrow{B}$ DIRECTED ALONG <010>

$\overrightarrow{B}$ PARALLEL TO $\overrightarrow{J}$

$\overrightarrow{B}$ DIRECTED ALONG <010>

$\overrightarrow{B}$ PARALLEL TO $\overrightarrow{J}$
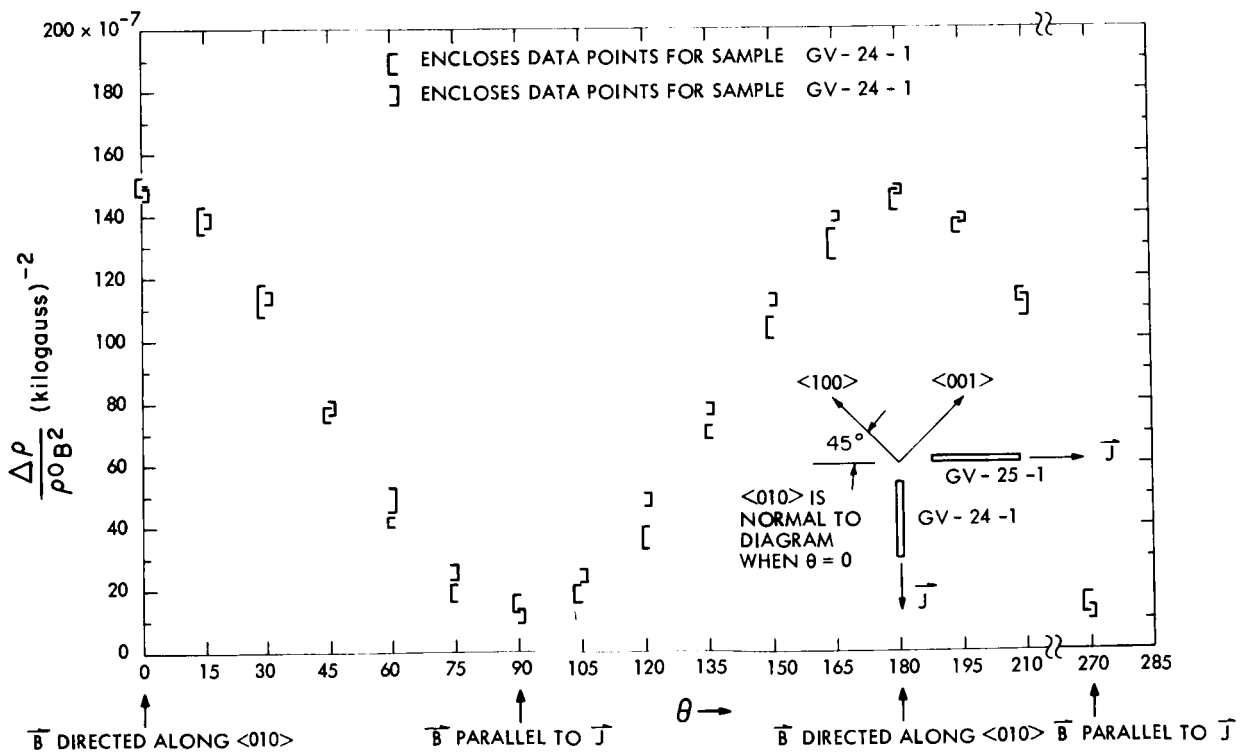
$p \sim 4 \times 10^{17} \ cm^{-3} \ 77.3^\circ K$ Crystal C-1078-C   Samples GV-24-1 and GV-25-1

Brackets Enclose Data Points For B = 12.55, 11.00, 10.00 kg.

Fig. 4.30   Magnetoresistance in Copper Doped ZnSb

The observed longitudinal effects probably arise from local departures from sample uniformity. These nonuniformities are principally local crystalline imperfections and the finite size of the voltage contacts on the samples. Similar amounts of residual longitudinal magnetoresistance appear in published data for n-type GaAs[19] and n-type Si[18].

The magnitudes of the illustrated transverse magnetoresistance effects are not to be regarded as being quantitatively accurate. The observed transverse effects would vary by as much as 50% between samples in the few reproducibility checks that were made on these undoped samples.

Because of the apparent carrier precipitation effects which have been discussed in Section 4.2, the carrier concentration in crystal C-1081-C was slowly changing with time. This made the determination of the anisotropy in the electrical resistivity and Hall effect impossible – since they depend directly on the hole concentration, p. $\Delta\rho/\rho°$ does not depend directly on p. However, changing carrier concentrations do affect $\Delta\rho/\rho°$ through the value of the relaxation time, τ, which is sensitive to the amount of ionized impurity scattering which is present[20]. For these reasons, the major part of the measurement effort was concentrated on a copper doped crystal.

4.7.3 Magnetoresistance Measurements on Copper Doped P-Type ZnSb

4.7.3.1 Electrical current directed along principal crystallographic axes

Figure 4.17 through 4.28 present the observed data. This data indicates that the measurement results are reproducible to within 10% from sample to sample. These measurements were made on samples cut from crystal C-1078-C which was copper doped – $p \sim 4 \times 10^{17}$ cm^{-3}.

This data has the same qualitative features as the results which have been presented for the undoped crystal in the preceding section. In particular,

the longitudinal effects, ρ_{1111}/ρ_{11} and ρ_{3333}/ρ_{33} are very close to zero and the corresponding angular variation curves follow a good $\cos^2\theta$ dependence. As with the undoped crystal, ρ_{2222}/ρ_{22} is about 20% of the corresponding transverse effect. However it is still of the same absolute value as ρ_{1111}/ρ_{11} and ρ_{3333}/ρ_{33} – it only looks larger on a relative scale compared to the small transverse effect, ρ_{2233}/ρ_{22}. Evidently, these residual effects are characteristic of the degree of crystal uniformity and perfection. They are also characteristic of the degree to which the ideally vanishingly small areas of the voltage probe contacts have been approached in this work.

In an attempt to see if the sandblasted sample surfaces were responsible for the residual value of ρ_{2222}/ρ_{22}, sample GV-13-1 had 15μ of its surface removed in an aqua regia etch. As Figure 4.22 shows, this had no appreciable effect on the observed results. The Hall mobility vs. temperature curve for this etched sample also coincided with that of sample GV-1-1 (sandblasted surfaces) which has been shown in Figure 4.9.

If the valence band of ZnSb is characterized as a single ellipsoid, then the fact that ρ_{1111}/ρ_{11} and $\rho_{3333}/\rho_{33} \simeq 0$ requires that two of the principal axes of this ellipsoid lie along the <100> and <001> crystal axes. Thus, the third axes of the ellipsoid must lie along the <010> crystal axis. Hence, it is concluded that the approximately zero longitudinal magnetoresistance for electric currents directed along each of the principal crystal axes indicates that the energy surfaces of p-type ZnSb might be characterized by one or more general ellipsoids which are oriented with their principal axes parallel to the edges of the orthorhombic Brillouin zone.

The results of the magnetoresistance measurements are summarized in Table 4.5 The given values are arithmetric averages of 6 or more experimental values. These

TABLE 4.5

MEASURED GALVANOMAGNETIC COEFFICIENTS FOR COPPER DOPED P-TYPE ZnSb

Crystal C-1078-C   77.3°K

$$p \sim 4 \times 10^{17} \; cm^{-3}$$

$$\rho_{11} = 1.40 \; (\pm \, 0.10) \times 10^{-2} \; (ohm\text{-}cm)$$

$$\rho_{22} = 2.20 \; (\pm \, 0.15) \times 10^{-2}$$

$$\rho_{33} = 0.95 \; (\pm \, 0.07) \times 10^{-2}$$

$$\rho_{123} = \rho_{312} = \rho_{231} = 16.9 \pm 1.3 \; cm^3/coulomb$$

In units of $(kilogauss)^{-2}$ and with a probable error of $\pm \, 10\%$.

$\dfrac{\rho_{1111}}{\rho_{11}} \sim 0$ (5.8×10^{-7})	$\dfrac{\rho_{2211}}{\rho_{22}} = 90 \times 10^{-7}$	$\dfrac{\rho_{3311}}{\rho_{33}} = 95 \times 10^{-7}$
$\dfrac{\rho_{1122}}{\rho_{11}} = 143 \times 10^{-7}$	$\dfrac{\rho_{2222}}{\rho_{22}} \sim 0$ (14×10^{-7})	$\dfrac{\rho_{3322}}{\rho_{33}} = 157 \times 10^{-7}$
$\dfrac{\rho_{1133}}{\rho_{11}} = 53 \times 10^{-7}$	$\dfrac{\rho_{2233}}{\rho_{22}} = 50 \times 10^{-7}$	$\dfrac{\rho_{3333}}{\rho_{33}} \sim 0$ (6.8×10^{-7})

$$\rho_{1313} = - \; 24 \; (\pm 6) \times 10^{-9} \; (ohm\text{-}cm)/(kilogauss)^2$$

refer to Section 4.7.3.2

$$\rho_{1212} = - \; 85 \; (\pm 9) \times 10^{-9}$$

$$\rho_{2323} = -65 \; (\pm 15) \times 10^{-9}$$

This value was not measured. It was inferred from other data. This was done in Appendix 3.

values were obtained on two or more samples (the one exception being ρ_{2211}/ρ_{22}) and at several magnetic field levels in the range of 8 to 12.5 kg. The average values of the Hall coefficient (considered to be isotropic – refer to Section 4.5) and the averages of the measured values of the electrical resistivities are also included. The limits of error have been included for the latter quantities.

These experimentally determined, arithmetic averages for the magneto-resistance coefficients were used to construct the curves of the form $\cos^2\theta$, $\sin^2\theta$ and $\cos^2\theta + \sin^2\theta$ which appear on Figures 4.17 through 4.28.

It is of particular significance to note the apparent numerical symmetries in the results shown in Table 4.5. Within the estimated probable error in the experimentally determined values:

$$
\begin{aligned}
\rho_{2211}/\rho_{22} &= \rho_{3311}/\rho_{33} \\
\rho_{1122}/\rho_{11} &= \rho_{3322}/\rho_{33} \\
\rho_{1133}/\rho_{11} &= \rho_{2233}/\rho_{22}
\end{aligned}
\qquad (4.7)
$$

The significance of these results are discussed in Chapter 5.

4.7.3.2 Measurements on off-axis samples

Galvanomagnetic sample bars were cut with longitudinal axes (current axes) which did not coincide with a principal axis direction of the crystal. These bars were cut from crystal C-1078-C – on which most of the magnetoresistance measurements were made. The bars are identified by the sample numbers GV-24-1, GV-25-1 and GV-26-1. Figures 4.29 and 4.30 present the observed data. These figures include sketches of the orientation of the individual bars with respect to the principal axis system of the crystal. Sample GV-26-1 was cut from an (001) plane wafer at 45° to the <100> and <010> directions. Sample GV-24-1 was cut from an (010) wafer at 45° to the <100> and <001> directions. Finally,

sample GV-25-1 was cut from this same (010) wafer, but at 90° to the orientation of GV-24-1. The magnetoresistance of the axial (parallel to the current) component of the internal electric field was measured. Thus, the arrangement of the magneto-resistance probes was the same as that of the previous galvanomagnetic samples (Section 4.7.3.1) and is shown in Figure 2.9.

Using the results of Appendix 3, it can be shown that, with the electric current at 45° to the <100> and <001> directions and in the (010) plane, the measured magnetoresistance is given by:

$$\frac{\Delta\rho}{\rho^\circ B^2} = (\frac{1}{\rho^\circ_{11}+\rho^\circ_{33}}) \ [(\rho_{1122} + \rho_{3322}) \ \cos^2\theta$$

$$+ \frac{1}{2} (\rho_{1133} + \rho_{3311}) \ \sin^2\theta + 2\rho_{1313} \sin^2\theta] \qquad (4.8)$$

The plane of rotation of the magnetic field vector $\vec{B}$, and the angular reference for θ are given on Figure 4.30. This equation describes the measurement results for samples GV-24-1 and GV-25-1. A similar equation can be written to describe the measurement results for sample GV-26-1. At $\theta = 0°$ (transverse magneto-resistance) Eq. 4.8 becomes:

$$\frac{\Delta\rho}{\rho^\circ B^2} = (\frac{1}{\rho^\circ_{11}+\rho^\circ_{33}}) \ (\rho_{1122} + \rho_{3322}) \qquad (4.9)$$

ρ°_{11}, ρ°_{33}, ρ_{1122} and ρ_{3322} have all been determined by the previous measurements. The experimental values are presented in Table 4.5. Inserting these in Eq. 4.8 yields:

$$\frac{\Delta\rho}{\rho^\circ B^2} \ (\theta = 0°) = 150 \times 10^{-7} \ (\text{kilogauss})^{-2}$$

which is in excellent agreement with the average measured value of about 153 x 10^{-7} which is indicated on Figure 4.30.

At $\theta = 90°$ (longitudinal magnetoresistance):

$$\frac{\Delta\rho}{\rho°B^2} = \frac{1}{2} \left(\frac{1}{\rho°_{11}+\rho°_{33}} \right) (\rho_{1133} + \rho_{3311} + 4\rho_{1313}) \qquad (4.10)$$

Inserting values for $\rho°_{11}$, $\rho°_{33}$, ρ_{1133} and ρ_{3311} from Table 4.5 as well as the average measured value for $\Delta\rho/\rho°B^2$ (at this angle) from Figure 4.30 yields an equation which can be solved for ρ_{1313}. The value so determined is:

$$\rho_{1313} \simeq -24 \times 10^{-9} \frac{(ohm-cm)}{(kilogauss)^2}$$

Following the same procedure with the data of Figure 4.29 for sample GV-26-1 yields:

$$\rho_{1212} \simeq -85 \times 10^{-9} \frac{(ohm-cm)}{(kilogauss)^2}$$

These values have been included in Table 4.5. ρ_{2323} was not determined experimentally. Its value can be inferred from the above two results once a model for the valence band of ZnSb has been formulated. This has been done in Appendix 3 by using the model developed in Chapter 5. Since the above values were determined by subtracting two experimentally measured magnetoresistance voltage ratios, a probable error as high as $\pm$ 25% should be assigned to them.

The observed off-axis longitudinal magnetoresistance is almost as small as the on-axis longitudinal magnetoresistances which are considered to be residual (Section 4.7.3.1). Thus, it is uncertain as to how much of the magnitude of the observed off-axis longitudinal magnetoresistance is actually real. This point is dealt with in Section 5.6.2.

The developments in Appendix 3 indicate that it is reasonable to expect the off-axis longitudinal magnetoresistance to be zero.

4.8 BIBLIOGRAPHY

1. M.V. Kot and I.V. Kretsu, Sov. Phys. Solid State, $\underline{6}$, 1134 (1960).

2. R.Mazelsky, Westinghouse Research Laboratory, priviate communication.

3. Turner, Fischler, and Reese, J. Appl. Phys. $\underline{32}$, 2241 (1961).

4. Komiya, Masumoto, and Fan, Phys. Rev., $\underline{133}$, A1679 (1964).

5. W.W. Scanlon, Phys. Rev., $\underline{126}$, 509 (1962).

6. F.S. Ham, J. Appl. Phys., $\underline{30}$, 915 (1959).

7. Harper, Phys. Rev., $\underline{83}$, 709 (1951).

8. Handbook of Chemistry and Physics, 39th Ed., p. 2434, Chemical Rubber Publishing Co., Cleveland, Ohio (1957).

9. Justi, Rasch and Schneider, Adv. Energy Conv., $\underline{4}$, 27 (1964).

10. H.J. Goldsmid, Applications of Thermoelectricity, p. 34, Methuen and Co. Ltd., London, 1960.

11. Ibid.,p. 15.

12. J.R. Drabble and H.J. Goldsmid, Thermal Conduction in Semiconductors, Section 5.4.1, Pergamon Press, New York, (1961).

13. Ibid., p. 115.

14. T. Kawasaki and T. Tanaka, Japan, J. Appl. Phys., $\underline{2}$, 516 (1963).

15. E.H. Putley, The Hall Effect and Related Phenomena, Section 4.7, Butterworths, London, (1960).

16. C. Kittel, Introduction to Solid State Physics, p. 363, John Wiley & Sons, New York, New York (1959).

17. A.C. Beer, Galvanomagnetic Effects in Semiconductors, p. 69, Academic Press, New York, 1963.

18. E.H. Putley, op, cit., p. 19.

19. Woods and Chen, Phys. Rev., $\underline{135}$, (A1462) 1964.

20. A.C. Beer, op. cit., p. 141.

CHAPTER 5

MODEL FOR THE ELECTRONIC TRANSPORT PROCESSES IN P-TYPE ZnSb

5.1 INTRODUCTION

This chapter presents a model for the electronic transport properties of p-type ZnSb. This model explains the following observed properties of p-type ZnSb:

1. Isotropic thermoelectric power (Section 4.3.2)

2. Isotropic Hall coefficients (Section 4.5)

3. The qualitative symmetry of the magnetoresistance measurements, namely that the longitudinal effects vanish. (Section 4.7 and Figures 4.13-4.30)

4. The numerical symmetry observed in experimentally measured magneto-resistance ratios. (Section 4.7.3.1, Table 4.5 and Equation 4.7).

5.2 QUALITATIVE IMPLICATIONS OF THE MAGNETORESISTANCE MEASUREMENTS

The longitudinal magnetoresistance vanishes within reasonable experimental error when the electric current is directed along the principal axes of the crystal. This implies that the valence band can be characterized by one or more general ellipsoids which are oriented with their principal axes along the <100> <010> and <001> directions of the crystal.

The cyclotron resonance work of Stevenson[1] did not disclose the sign of the charge carrier which was responsible for the single observed resonance line (refer to Table 1.1). He was able to fit his data to a single zone centered ellipsoid of revolution (about the a axis). This geometry is a special case of the model which is developed here. Since it did not disclose the sign of the charge carrier and since only one resonance peak was observed, no further use will be made of this work.

The observed symmetry in the magnetoresistance measurements can be accounted for in terms of a valence band which has a surface of constant energy in the shape of a single general ellipsoid. This single, general ellipsoidal band is assumed to be centered at the point Γ (i.e., k = (0,0,0)), Figure 5.1(b). From his group theoretical study of the ZnSb crystal structure, Khartsiev[6] has shown that the gradient of $E(\vec{k})$ is zero – in all directions – at the symmetry points Γ and R. These have been shown in Figure 5.1(b).

The transport measurements which were made in this work offer no possibility of unambiguously establishing whether a single or many valley valence band is present. The fact that the off-axis longitudinal magneto-resistance is approximately zero (Figures 4.29 and 4.30, Section 5.6.2 and Appendix 3) indicates that a many valley band structure would have to contain ellipsoids which had the same relative spatial orientation. This rules out a many valley structure such as that of n-type silicon. A single valley valence band structure will be developed for a model in this work.

Finally, it should be noted that the lack of a magnetic field dependence in the measured Hall coefficients and magnetoresistance quantities, $\Delta\rho/\rho^\circ B^2$, (refer to Section 4.6) indicated that a "light hole" band (e.g. p-type germanium) is not present. Also, in comparison with data on p-type germanium and silicon, these results on ZnSb infer that serious warping of the valence band is not present.

5.3 THEORETICAL DEVELOPMENT

The transport coefficients for a general ellipsoid have been derived from a solution of the Boltzmann equation. In Appendix 2, results are presented for the:
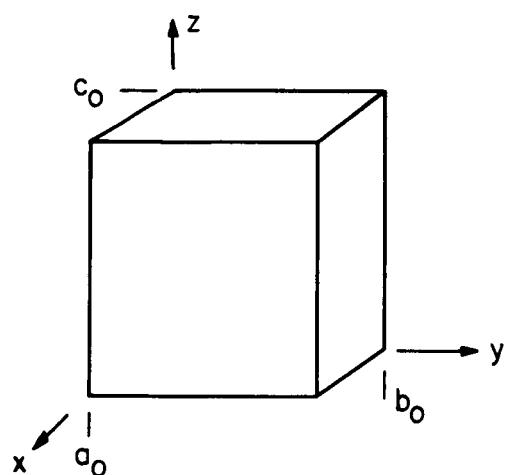
(a) ORTHORHOMBIC
PRIMITIVE UNIT CELL
OF THE CRYSTAL LATTICE

$a_o = 6.20 \ \overset{o}{A}$

$b_o = 7.74$

$c_o = 8.10$
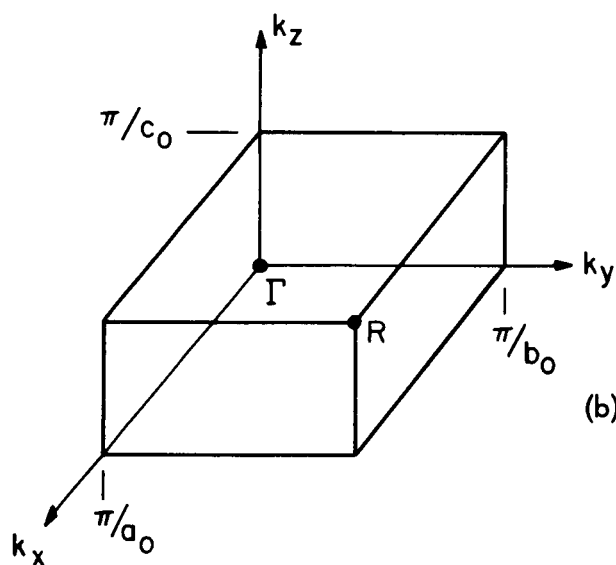
(b) ONE OCTANT OF
THE BRILLOUIN ZONE
FOR THE SIMPLE
ORTHORHOMBIC LATTICE

(c) ONE OCTANT OF
A SURFACE OF
CONSTANT ENERGY
OF A POSSIBLE VALENCE
BAND -
RELATIVE DIMENSIONS
ARE INDICATED
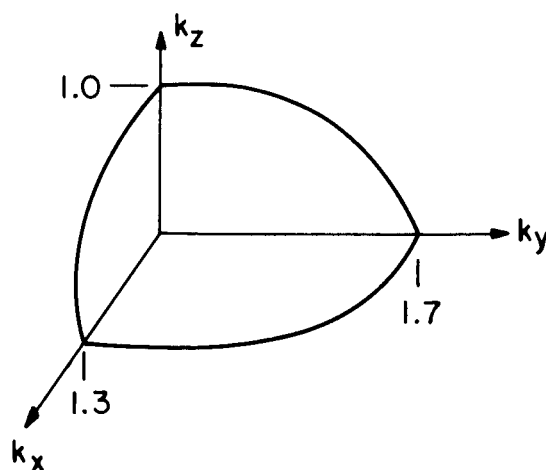
Fig. 5.1 Important Geometries for Zinc Antimonide

1. Thermoelectric power

2. Electronic contribution to the thermal conductivity

3. Electrical resistivity

4. Hall coefficients

5. Magnetoresistance coefficients.

These analytical results and a summary of the approximations which were used in solving the Boltzmann equation are summarized in Sections A.2.1 and A.2.7. In particular, the relaxation time was assumed to be a diagonal tensor when referred to the coordinate system in which the effective mass is diagonal. The elements of the relaxation time are assumed to be functions of energy only. Each element can possibly be a different function of energy. This assumed form of the relaxation time is in accordance with the work of Herring and $\text{Vogt}^{(2)}$, who have shown that scattering processes which either conserve energy or randomize particle velocity can be approximated by relaxation times of this form. This includes ionized impurity scattering and scattering by acoustic phonons.

In the following discussion, it will be assumed that the action of two or more simultaneous scattering mechanisms can be represented by:

$$\left(\frac{1}{\tau_{net}} \right)_{ii} = \left(\frac{1}{\tau_A} \right)_{ii} + \left(\frac{1}{\tau_I} \right)_{ii} + \ldots \qquad (5.1)$$

where $(\tau_A)_{ii}$ and $(\tau_I)_{ii}$ are the relaxation time tensor elements for acoustic phonon and ionized impurity scattering, respectively. The presense of additional scattering mechanisms, such as neutral impurity scattering, will not be considered.

The following functional forms for the net relaxation time will be considered:

A. Constant relaxation time:

$\tau = \tau^{\circ}$ a constant

B. Constant tensor relaxation time:

$$\overset{\leftrightarrow}{\tau} = \begin{pmatrix} A & 0 & 0 \\ 0 & B & 0 \\ 0 & 0 & C \end{pmatrix} \quad \text{where A,B,C are constants}$$

C. Scalar function of energy relaxation time:

$\tau = F(E)$, $F(E)$ is a function of electron (hole) energy

D. Relaxation time tensor with a factorable energy dependence

$$\overset{\leftrightarrow}{\tau} = \begin{pmatrix} \tau_1 & 0 & 0 \\ 0 & \tau_2 & 0 \\ 0 & 0 & \tau_3 \end{pmatrix} F(E)$$

where τ_1, τ_2 and τ_3 are constants (not necessarily equal) and $F(E)$ is some function of energy.

E. Relaxation time tensor with an unfactorable energy dependence:

$$\overset{\leftrightarrow}{\tau} = \begin{pmatrix} \tau_1(E) & 0 & 0 \\ 0 & \tau_2(E) & 0 \\ 0 & 0 & \tau_3(E) \end{pmatrix}$$

Figure 5.1(a) shows the shape and dimensions of the primitive orthorhombic unit cell of the ZnSb crystal structure. Figure 5.1(b) shows one octant of the first Brillouin zone of ZnSb. Finally, anticipating the results of Section 5.7, Figure 5.1(c) presents one octant of a surface of constant energy for one possible model of the ZnSb valence band.

5.4 ISOTROPY OF THE THERMOELECTRIC POWER

As discussed in Section 4.3.2 and illustrated by Figure 4.3, the thermoelectric power of p-type ZnSb is isotropic. For a single general ellipsoid the thermoelectric power has the form (Eq. A.2.84):

$$\alpha_{ij} = \frac{1}{Tq} \frac{<(E-E_F)\tau_{ii}>}{<\tau_{ii}>} \delta_{ij} \tag{5.2}$$

It is seen that relaxation times of the forms A, B, C, and D, above, will give an isotropic thermoelectric power. In general a relaxation time of the form E will not give an isotropic thermoelectric power.

5.5 ISOTROPY OF THE HALL COEFFICIENT

As discussed in Section 4.5 and illustrated by Tables 4.2, 4.3 and 4.4 the Hall coefficients of p-type ZnSb are isotropic. For a single general ellipsoid the Hall coefficient of ZnSb has the form (Eq. A.2.88):

$$\rho_{ijk} = - \epsilon_{ijk} \frac{1}{pq} \frac{<\tau_{ii} \tau_{jj}>}{<\tau_{ii}><\tau_{jj}>} \tag{5.3}$$

It is seen that relaxation times of the form A, B, C and D, above, will give an isotropic Hall effect. In general a relaxation time of the form E will not give isotropic Hall coefficients.

5.6 OBSERVATIONS FROM THE MAGNETORESISTANCE MEASUREMENTS

5.6.1 Numerical Symmetry in the On-Axis Measurements

As mentioned in Section 4.7.3.1 and shown by Table 4.5 the following numerical symmetry was observed in the results of the magnetoresistance measurements:

$$\rho_{2211}/\rho_{22} = \rho_{3311}/\rho_{33} \tag{5.4}$$
$$(90 \times 10^{-7} = 95 \times 10^{-7})$$

$$\rho_{1122}/\rho_{11} = \rho_{3322}/\rho_{33} \tag{5.5}$$
$$(143 \times 10^{-7} = 157 \times 10^{-7})$$

$$\rho_{1133}/\rho_{11} = \rho_{2233}/\rho_{22} \tag{5.6}$$
$$(53 \times 10^{-7} = 50 \times 10^{-7})$$

The observed numerical results have been inserted beneath the literal

expressions. Using Equations A.2.89 it is seen that:

$$\rho_{2211}/\rho_{22} = \rho_{3311}/\rho_{33}$$

implies that:

$$\frac{pq^2 <\tau_{22}>}{m_2} \frac{1}{pm_3} \left[\frac{<\tau_{22}^2 \tau_{33}>}{<\tau_{22}>^2} - \frac{<\tau_{22} \tau_{33}>^2}{<\tau_{22}>^2 <\tau_{33}>} \right]$$
$$= \frac{pq^2 <\tau_{33}>}{m_3} \frac{1}{pm_2} \left[\frac{<\tau_{33}^2 \tau_{22}>}{<\tau_{33}>^2} - \frac{<\tau_{33} \tau_{22}>^2}{<\tau_{33}>^2 <\tau_{22}>} \right] \tag{5.7}$$

which reduces to:

$$<\tau_{22}^2 \tau_{33}> <\tau_{33}> = <\tau_{33}^2 \tau_{22}><\tau_{22}> \tag{5.8}$$

Notice that a relaxation time of the forms A or B will give a magnetoresistance

which is identically zero. Thus, the above expressions are satisfied trivially

and have no physical significance. Relaxation times of the form C and D will

satisfy Eq. 5.6. A relaxation time of the form E will not, in general, satisfy

Eq. 5.6.

Similarly Equations 5.5 and 5.6 imply that:

$$<\tau_{11}^2 \tau_{22}> <\tau_{22}> = <\tau_{22}^2 \tau_{11}><\tau_{11}> \tag{5.9}$$
$$<\tau_{11}^2 \tau_{33}> <\tau_{33}> = <\tau_{33}^2 \tau_{11}><\tau_{11}> \tag{5.10}$$

The above discussion applies here, also. These equations are satisfied, in

general, only by relaxation times of the form C and D.

5.6.2 Longitudinal Magnetoresistance on Off-Axis Samples

As was mentioned in Section 4.7.3.1 and shown by Figures 4.29 and 4.30,

the off-axis longitudinal magnetoresistance is close to zero in the two

different off-axis orientations which were measured. Intuitively this might

be a disturbing result. It might be expected that a zero longitudinal magneto-resistance would be observed only when $\vec{B}$ and $\vec{J}$ are parallel to a principal axis of a valence band which has a general ellipsoid for a constant energy surface.

However, as is shown in Appendix 3, the longitudinal magnetoresistance of an energy band which has a general ellipsoid for a constant energy surface vanishes regardless of the direction of the electric current density vector. This result is only true, in general, for relaxation times of the form C and D of Section 5.2. Hence, the fact that the observed longitudinal magnetoresistance is practically zero is entirely consistent with the single general ellipsoid valence band model.

5.6.3 Probable Form of the Relaxation Time

The above discussion reasonably establishes that a relaxation time appropriate to p-type ZnSb is either a scalar function of energy (form C of Section 5.2)

$$\tau = F(E) \tag{5.11}$$

or a tensor with a factorable energy dependence:

$$\overset{\leftrightarrow}{\tau} = \begin{pmatrix} \tau_1 & 0 & 0 \\ 0 & \tau_2 & 0 \\ 0 & 0 & \tau_3 \end{pmatrix} F(E) \qquad \text{(form D of} \atop \text{Section 5.2)} \tag{5.12}$$

where τ_1, τ_2, and τ_3 are constants.

A relaxation time with either of these two forms will account for the experimentally observed:

1. Isotropic thermoelectric power (at 0°C).

2. Isotropic Hall effect (300°K and 77.3°K).

3. Numerical symmetry in the on-axis ($\vec{J}$ parallel to a principal crystal axis) longitudinal magnetoresistance results (77.3°K).

4. Approximately zero longitudinal magnetoresistance off-axis ($\vec{J}$

not parallel to a principal crystal axis) (77.3°K).

The above relaxation times, forms C and D, fit the symmetry of the observed

results even though mixed scattering is important - especially at 77.3°K

in the magnetoresistance samples cut from crystal C-1078-C (refer to the Hall

mobility vs. temperature curves on Figure 4.9).

For scattering by acoustical phonons:

$$(\tau_A)_{ii} = (\tau_A^o(T))_{ii} \, E^{-1/2} \qquad (5.13)$$

and for scattering by ionized impurities:

$$(\tau_I)_{ii} = (\tau_I^o(T))_{ii} \, E^{+3/2} \qquad (5.4)$$

where $\tau_A^o(T)$ and $\tau_I^o(T)$ are temperature dependent coefficients. Combining

these two expressions according to Eq. 5.1 yields:

$$\left(\frac{1}{\tau_{net}}\right)_{ii} \equiv \nu_{ii} = \left(\frac{1}{\tau_A^o}\right)_{ii} E^{+1/2} + \left(\frac{1}{\tau_I^o}\right)_{ii} E^{-3/2} \qquad (5.15)$$

where $i = 1, 2, 3$.

From the functional form of Eq. 5.15 it is seen that the net relaxation

time will be an isotropic function of energy (form C or Eq. 5.11) if there is

no anisotropy in the acoustic phonon or ionized impurity scattering. On the

other hand the net relaxation time will be a tensor with a factorable energy

dependence (form D or Eq. 5.12) only if both acoustic phonon and ionized

impurity scattering have the same anisotropy.

There is no reason to chosse relaxation form C over relaxation form D

without further experimental work on ZnSb. This work would include a reliable

determination of the effective masses of the holes, of the velocities of sound,

the deformation potentials and the static dielectric constants of ZnSb.

5.7 COMPARISON OF MAGNETORESISTANCE AND MOBILITY RATIOS

Using the results of Appendix 2 (Equations A.2.87, 88 and 89) it is seen that the magnetoresistance:

$$\frac{\rho_{iiii}}{\rho_{ii}} = \frac{1}{\beta_i \beta_k} q^2 \left[\frac{<F(E)^3>}{<F(E)>} - \frac{<F(E)^2>^2}{<F(E)>^2} \right] \tag{5.16}$$

and the Hall mobility:

$$\mu_{ii} = \frac{1}{\beta_i} q \frac{<F(E)^2>}{<F(E)>} \tag{5.17}$$

and the electrical conductivity

$$\sigma_{ii} = \frac{1}{\beta_i} pq^2 <F(E)> \tag{5.18}$$

where $i \neq j \neq k$ and can range over any of the six permutations of 1, 2 and 3. In the above:

$$\beta_i \equiv (\frac{m_i}{\tau_i}); \qquad i = 1, 2, 3 \tag{5.19}$$

The relaxation time has been assumed to be of form D:

$$\tau_{ij} = \begin{pmatrix} \tau_1 & 0 & 0 \\ 0 & \tau_2 & 0 \\ 0 & 0 & \tau_3 \end{pmatrix} F(E)$$

where $\tau_1 \neq \tau_2 \neq \tau_3$ and all are constants at a given temperature. $F(E)$ is a function of energy. Finally, the above forms of Equation 5.17, 5.18 and 5.19 have been derived for a valence band of a general ellipsoidal form and which has its principal axes parallel to the principal axes of the crystal.

Notice that a direct check on the validity of the magnetoresistance results can be made. Using the calculated magnetoresistance coefficients and taking care to use ratios that contain only one form of ρ_{ii}:

$$\frac{\rho_{iiii}/\rho_{ii}}{\rho_{iikk}/\rho_{ii}} = \frac{\beta_i}{\beta_k} \qquad (5.20)$$

Likewise, using the Hall mobilities:

$$\frac{\mu_{kk}}{\mu_{jj}} = \frac{\beta_j}{\beta_k} \qquad (5.21)$$

and the electrical conductivities:

$$\frac{\sigma_{kk}}{\sigma_{jj}} = \frac{\beta_j}{\beta_k} \qquad (5.22)$$

The results obtained are summarized in Table 5.1. The magnetoresistance results of Table 4.5 were used to compute the magnetoresistance ratios. Notice that if the relaxation is isotropic (form C), then the ratios of the β_{ii}'s are actually equal to the ratios of the hole effective masses. A sketch of one quadrant of a surface of constant energy in the valence band, calculated under this assumption, appears as Figure 5.1(c). This table shows that the magnetoresistance data is entirely consistent with the Hall mobility and electrical conductivity data. The magnetoresistance ratios e.g.;

$$\frac{\rho_{3311}/\rho_{11}}{\rho_{3322}/\rho_{22}}$$

have a probable accuracy of about $\pm$ 10% and the mobility and conductivity ratios about $\pm$ 5%.

The observed numerical agreement in Table 5.1 is a demonstration of the validity of the band structure model assumed for p-type ZnSb.

TABLE 5.1

COMPARISON OF MAGNETORESISTANCE RATIOS
AND THE RATIOS OF HALL MOBILITIES
OR ELECTRICAL CONDUCTIVITIES

All of the following quantities were measured experimentally:

A. MAGNETORESISTANCE RATIOS:

Crystal C-1078-C, $p \sim 4 \times 10^{17}$ cm^{-3}, 77.3°K
Data taken from Table 4.5:

$$\frac{\rho_{1133}/\rho_{11}}{\rho_{1122}/\rho_{11}} = \frac{\beta_3}{\beta_2} = \frac{53}{143} = 0.37$$

$$\frac{\rho_{3311}/\rho_{33}}{\rho_{3322}/\rho_{33}} = \frac{\beta_1}{\beta_2} = \frac{95}{157} = 0.61$$

$$\frac{\rho_{2233}/\rho_{22}}{\rho_{2211}/\rho_{22}} = \frac{\beta_3}{\beta_1} = \frac{50}{90} = 0.56$$

B. HALL MOBILITY RATIOS:

(1). Crystal C-1078-C, $p \sim 4 \times 10^{17}$ cm^{-3}, 77.3°K
Data shown on Figure 4.9:

$$\frac{\mu_b}{\mu_c} = \frac{\beta_3}{\beta_2} = \frac{750}{1860} = 0.40; \quad \frac{\mu_b}{\mu_a} = \frac{\beta_1}{\beta_2} = \frac{750}{1150} = 0.65$$

$$\frac{\mu_a}{\mu_c} = \frac{\beta_3}{\beta_1} = \frac{1150}{1860} = 0.62$$

(2). Crystal C-1078-C, $p \sim 4 \times 10^{17}$ cm^{-3}, 300°K
Data shown on Figure 4.9:

$$\frac{\mu_b}{\mu_c} = \frac{\beta_3}{\beta_2} = \frac{290}{750} = 0.39; \quad \frac{\mu_b}{\mu_a} = \frac{\beta_1}{\beta_2} = \frac{290}{430} = 0.67$$

$$\frac{\mu_a}{\mu_c} = \frac{\beta_3}{\beta_1} = \frac{430}{750} = 0.57$$

(3). Komiya, Masumoto and Fan[5], $p \sim 2 \times 10^{16}$ cm^{-3}, 273°K
Undoped crystal, their Figure 2:

$$\frac{\mu_b}{\mu_c} = \frac{\beta_3}{\beta_2} = \frac{210}{620} = 0.34; \quad \frac{\mu_b}{\mu_a} = \frac{\beta_1}{\beta_2} = \frac{210}{405} = 0.52$$

$$\frac{\mu_a}{\mu_c} = \frac{\beta_3}{\beta_1} = \frac{405}{620} = 0.65$$

(4). Crystal C-1081-C, $p \sim 2 \times 10^{16}$ cm^{-3}, 273°K
Undoped crystal, data shown on Figures 4.6 and 4.7:

$$\frac{\mu_b}{\mu_c} = \frac{\beta_3}{\beta_2} = \frac{330}{830} = 0.40; \quad \frac{\mu_b}{\mu_a} = \frac{\beta_1}{\beta_2} = \frac{330}{520} = 0.63$$

$$\frac{\mu_a}{\mu_c} = \frac{\beta_3}{\beta_1} = \frac{520}{830} = 0.63$$

C. ELECTRICAL CONDUCTIVITY RATIOS:

Crystal C-1075-B, $p \sim 1.1 \times 10^{19}$ cm^{-3}, 273°K
Typical of the data of Figure 4.3:

$$\frac{\sigma_b}{\sigma_c} = \frac{\beta_3}{\beta_2} = \frac{370}{950} = 0.39; \quad \frac{\sigma_b}{\sigma_a} = \frac{\beta_1}{\beta_2} = \frac{370}{615} = 0.60$$

$$\frac{\sigma_a}{\sigma_c} = \frac{\beta_3}{\beta_1} = \frac{614}{950} = 0.64$$

5.8 ESTIMATION OF THE EFFECTIVE MASSES

Using thermoelectric power data, the carrier concentration obtained from Hall effect measurements, and an assumed form of the relaxation time, the density of states effective mass can be estimated.[7] Using experimental results for crystal C-1078-C at 0°C and assuming that lattice scattering (acoustic phonon scattering) is dominant at 0°C (see Figure 4.9), the value obtained is:

$$m_d = 0.42 \, m_o \tag{5.23}$$

where m_o is the rest mass of a free electron.

From Appendix 2, Equation A.2.68:

$$m_d = (m_1 \, m_2 \, m_3)^{1/3} \tag{5.24}$$

Assuming that the relaxation time is isotropic, Table 5.1 yields

$$\frac{m_1}{m_2} = 0.61$$

$$\tag{5.25}$$

$$\frac{m_3}{m_2} = 0.37$$

Combining these equations yields:

$$m_1 = 0.42 \, m_o$$

$$m_2 = 0.69 \, m_o \tag{5.26}$$

$$m_3 = 0.26 \, m_o$$

These results are only approximate.

5.9 BIBLIOGRAPHY

1. M.J. Stevenson, Proceedings of the International Conference on Semiconductor Physics, Prague, 1960, p. 1083.

2. A.C. Beer, Galvanomagnetic Effects in Semiconductors, Ch. 7, Academic Press, New York, New York, (1963).

3. C. Herring and E. Vogt, Phys. Rev., 101, 944 (1956).

4. W.E. Krag and M.C. Brown, Phys. Rev., 134, A779 (1964).

5. Komiya, Masumoto and Fan, Phys. Rev., 133, A1679 (1964).

6. V.E. Khartsiev, Soviet Physics Sol. State, 4, 721 (1962).

7. R.A. Smith, Semiconductors, p. 172, Cambridge University Press, Cambridge, England, (1959).

CHAPTER 6

SUMMARY AND RECOMMENDATIONS FOR FURTHER WORK

6.1 SUMMARY

This work has described the preparation, growth, doping, and cutting of p-type ZnSb single crystals (Chapter 2). Instrumentation and techniques for the measurement of the thermoelectric power and thermal conductivity (at 0°C), electrical resistivity and Hall mobility (77.3°K to 325°K), and magneto-resistance at 77.3°K have been described (Chapter 3) and the measurement results presented (Chapter 4). Reversible changes in the hole concentrations of undoped crystals were found to occur under annealing at elevated temperatures (Chapter 4).

Measurements at 0°C indicate (Section 4.3.4) a maximum thermoelectric figure of merit of 0.74×10^{-3} (°K)$^{-1}$. The figure of merit may be considerably improved by reducing the comparatively large thermal conductivity of the single crystals (0.037 watts/cm-°K as opposed to ∿0.014 for polycrystalline material).

The experimentally observed results of the galvanomagnetic measurements have been shown (Chapter 5) to be consistent with a model of the valence band which assumes that:

1. A single ellipsoid describes a surface of constant energy. This ellipsoid is assumed to be a general ellipsoid with the corresponding effective masses, m_1, m_2 and m_3. The principal axes of this ellipsoid coincide with those of the crystal.

2. The relaxation time is either a scalar function of energy or a diagonal tensor with a factorable energy dependence. This tensor has been assumed to be diagonal in the principal axis system for the crystal.

A numerical comparison (Table 5.1) of equalities in magnetoresistance ratios and Hall mobility ratios has been made. The relations expected from the above model of the conduction processes have been observed and are found

to be in good agreement.

6.2 RECOMMENDATIONS FOR FURTHER WORK

It is felt that immediate experimental effort is best placed in the following areas:

1. The growth of single crystal in controlled atmospheres of antimony or zinc vapor should be investigated. The resulting control of crystal stoichiometry may result in the production of n-type single crystals. Up to the present time chemical doping has not produced n-type crystals.

2. The annealing phenomena--the increase in hole concentration with increased ambient temperature--should be investigated. The specific areas in which further work is needed have been outlined in Section 4.2.4. There is probably a direct link between this observed phenomena and the high temperature (400°C) instabilities which previous workers have observed in thermoelectric elements constructed from ZnSb.

3. Attempts should be made to reduce the large lattice contribution to the thermal conductivity of this material. This could possibly be done by incorporating a third atom into the zinc antimonide crystal lattice.

4. Detailed galvanomagnetic measurements should be extended to undoped, p-type material. The measurement program which is used must insure that each measurement sample has an identical thermal history. This will avoid the changes in carrier concentration with time that have been observed on annealed crystals in this work. Hopefully, the results of these galvanomagnetic measurements would confirm the model of the conduction processes in p-type ZnSb which has been developed in this work.

5. An independent and unambiguous determination of the absolute effective

masses of the charge carriers should be made. This can be done by

cyclotron resonance or the magnetooptical techniques. These experiments

would hopefully substantiate the valence band model which has been

proposed in this work. It would be also then possible to obtain a

direct measure of the possible anisotropy in the relaxation time for holes

in ZnSb.

APPENDIX I

MACROSCOPIC SYMMETRY CONSIDERATIONS IN THE D_{2h} POINT GROUP

Each of the second order transport tensors, such as electrical and thermal conductivity, and thermoelectric power, can be phenomenologically expanded as a Taylor series in magnetic field strength. In the limit of low enough magnetic field strengths, the sum of the first few terms of the Taylor series expansion will supply a good approximation to the actual numerical value of any one of the elements of the second order transport tensors. The coefficients corresponding to the same power of magnetic field strength in the phenomenological expansions can be grouped together in such a way that they themselves are the elements of tensors or pseudotensors. These tensors are of rank two or greater. The purpose of this appendix is to derive the zero elements of these phenomenological tensors from macroscopic symmetry considerations.

Before continuing it is of interest to note that TiO_2, gallium, crystalline benzol, cadmium antimonide and materials with the Olivine crystal structure share the same point group with zinc antimonide.

The D_{2h}^{15} space group contains three mutually perpendicular, right handed, 180° screw axes and a center of inversion as its non-trivial microscopic symmetry elements. For the purpose of macroscopic transport experiments, the one half of a unit cell edge translation in a screw symmetry operation is not detectable. Hence the pertinent symmetry properties can be characterized as those of the D_{2h} point group. These are three mutually perpendicular two-fold rotation axes and a center of inversion. These are equivalent to three mutually perpendicular reflection planes. Choosing the former representation, the generating operations, in the principal coordinate system of the unit cell, are:

I. 180° rotation about the "1" ("x" or "a") axis:

$$(a_{ij}) = \begin{pmatrix} 1 & 0 & 0 \\ 0 & -1 & 0 \\ 0 & 0 & -1 \end{pmatrix}$$

II. 180° rotation about the "2" ("y" or "b") axis:

$$(a_{ij}) = \begin{pmatrix} -1 & 0 & 0 \\ 0 & 1 & 0 \\ 0 & 0 & -1 \end{pmatrix}$$

III. 180° rotation about the "3" ("z" or "c") axis:

$$(a_{ij}) = \begin{pmatrix} -1 & 0 & 0 \\ 0 & -1 & 0 \\ 0 & 0 & 1 \end{pmatrix}$$

IV. Center of inversion:

$$(a_{ij}) = \begin{pmatrix} -1 & 0 & 0 \\ 0 & -1 & 0 \\ 0 & 0 & -1 \end{pmatrix}$$

V. Identity operation:

$$(a_{ij}) = \begin{pmatrix} 1 & 0 & 0 \\ 0 & 1 & 0 \\ 0 & 0 & 1 \end{pmatrix}$$

The electrical resistivity will be used as an example in the following cal-
culation. It should be remembered that the results of the calculation,
excluding those algebraic condensations resulting from the application of
Onsager symmetry, apply to any second order tensor crystal property that can
be expanded, at least formally, in a Taylor series in the magnetic field.

From the definition of a tensor:

$$\rho_{i'j'}(H_{1'}, H_{2'}, H_{3'}) = a_{i'i} \, a_{j'j} \, \rho_{ij}(H_1, H_2, H_3)$$

where a coordinate in the transformed coordinate system is denoted by a primed subscript. The Einstein summation convention is used here unless otherwise stated. The implicit dependence on magnetic field strength, $\vec{H}$, is denoted by the functional indication of the magnetic field strength components, H_1, H_2, H_3. The magnetic field strength is a pseudovector, that is

$$H_{i'} = ||a|| \; a_{i'i} \; H_i$$

where $||a||$ is the determinant of the transformation matrix, a_{ij}.

Applying symmetry operation I($180°$ rotation about the x or "1" axis), it is seen that:

$$\rho_{1'1'}(H_{1'}, \; H_{2'}, \; H_{3'}) = \rho_{11}(H_1, \; H_2, \; H_3)$$

where $H_{1'} = H_1$

$H_{2'} = -H_2$

$H_{3'} = -H_3$

Since the transformation is a symmetry operation, the (1') axis is experimentally equivalent to the (1) axis. Thus:

$$\rho_{11}(H_1, \; -H_2, \; -H_3) = \rho_{11}(H_1, \; H_2, \; H_3)$$

Applying symmetry operation II:

$$\rho_{11}(-H_1, \; H_2, \; -H_3) = \rho_{11}(H_1, \; H_2, \; H_3)$$

Applying symmetry operation III:

$$\rho_{11}(-H_1, \; -H_2, \; H_3) = \rho_{11}(H_1, \; H_2, \; H_3)$$

The other symmetry operations, or combinations thereof, yield no new information.

The above three symmetry results indicate that a Taylor series expansion of $\rho_{11}(\vec{H})$:

$$\rho_{11}(\vec{H}) = \rho_{11}{}^{\circ} + \rho_{11k}H_k + \rho_{11k\ell}H_kH_\ell + \rho_{11k\ell m}H_kH_\ell H_m + \rho_{11k\ell mn}H_kH_\ell H_mH_n \qquad \text{(A.1.1)}$$

must be functionally even in H_2, H_3, even in H_1, H_3, and even in H_1, H_2.

Hence, the <u>zero field resistivity</u>:

$$\rho_{11}{}^{\circ} \neq 0$$

The component of the <u>Hall effect tensor</u>:

$$\rho_{11k} = 0$$

The $\rho_{11k\ell}$ component of the <u>magnetoresistance tensor</u> is a second rank tensor. It has nine elements. In order to systematically consider the elements of this tensor, the following cases may be defined:

<u>Case I</u>: $k = \ell$

Thus $\rho_{11k\ell} = \rho_{11kk}$. (3 elements)

From the above results of the symmetry considerations, it is seen that:

$$\rho_{1111}, \ \rho_{1122}, \ \rho_{1133} \neq 0$$

<u>Case II</u>: $k \neq \ell$ (6 elements)

The above results of the symmetry considerations it is seen that:

$$\rho_{11k\ell} = 0 \text{ for } k \neq \ell$$

Continuing with the next Taylor series term which is <u>cubic in H</u>:

$$\rho_{11k\ell m}$$

it is seen that twenty-seven elements have to be considered. Proceeding in a systematic fashion, the following cases can be considered:

<u>Case I</u>: $k = \ell = m$ (3 elements)

Thus: $\rho_{11k\ell m} = \rho_{11kkk}$

From the above results of the symmetry considerations:

$$\rho_{11kkk} = 0$$

Case II: $k = \ell \neq m$ (18 elements)

It should be remembered that since k, ℓ, and m are dummy indices which are used

in the Einstein summation convention within the Taylor series expansion:

$$\rho_{11k\ell m} \, H_k H_\ell H_m = \rho_{11m\ell k} \, H_m H_\ell H_k, \text{ etc.}$$

The condition $k = \ell \neq m$ is equivalent to $k \neq \ell = m$. At any rate, reasoning

from symmetry, as above:

$$\rho_{11kk\ell} = \rho_{11k\ell k} = \rho_{11\ell kk} = 0$$

Case III: $k \neq \ell \neq m$ (6 elements)

In this case (without the application of Onsager symmetry):

$$\rho_{11123} = \rho_{11231} = \rho_{11312} = \rho_{11213} = \rho_{11321} = \rho_{11132} \neq 0$$

The possible non-zero nature of these elements follows from the symmetry

arguments. The equality of these six elements follows from the fact that

they are simply symbols for equivalent partial derivatives in a Taylor series

expansion. Notice that $3 + 18 + 6 = 27$. Thus, all possible twenty-seven

elements have been considered.

Finally consider:

$$\rho_{11k\ell mn}$$

which is quartic in H. In this case, eighty-one elements must be considered.

Proceeding systematically:

Case I: $k = \ell = m = n$ (3 elements)

$$\rho_{11kkkk} \neq 0$$

Case II: $k = \ell \neq m = n$ (18 elements)

$$\rho_{11kk\ell\ell} \neq 0$$

<u>Case III</u>: $k = \ell = m \neq n$ (24 elements)

$$\rho_{11kkk\ell} = 0$$

<u>Case IV</u>: $k = \ell \neq m \neq n$ (36 elements)

$$\rho_{11kkmn} = 0$$

Notice again that $3 + 18 + 24 + 36 = 81$.

Collecting these results, including a summation of equivalent terms in the Taylor series expansion:

$$\rho_{11}(H) = \rho_{11}^{\circ} + \rho_{1111}H_1^2 + \rho_{1122}H_2^2 + \rho_{1133}H_3^2 + 6\rho_{11123}H_1H_2H_3$$

$$+ \rho_{111111}H_1^4 + \rho_{112222}H_2^4 + \rho_{113333}H_3^4 + 6\rho_{111122}H_1^2H_2^2 \qquad (A.1.2)$$

$$+ 6\rho_{111133}H_1^2H_3^2 + 6\rho_{112233}H_2^2H_3^2$$

through fourth order terms in H and without the application of Onsager symmetry.

The expansion of the other eight elements of $\rho_{ij}(\vec{H})$ can be derived in exactly the same manner. Table A-I summarizes the results of the complete calculation. The proper multiplicative numerical factors which result from the summation of equivalent terms in the Taylor series expansion are included. Notice that Onsager symmetry has not been introduced as yet. Hence, these results can be applied to the small magnetic field expansions of any second order tensor property of a D_{2h} point group crystal.

The electrical resistivity should exhibit the following Onsager symmetry: $\rho_{ij}(\vec{H}) = \rho_{ji}(-\vec{H})$. In addition to supplying relations between off diagonal elements, this additional condition requires that: $\rho_{11123} = \rho_{22123} = \rho_{33123} = 0$.

Each of the above results may be recovered from the following expansion. <u>In this expansion the Einstein summation convention has been abandoned.</u> The literal subscripts mean that the components are to be assigned according to the following list of permutations:

$\underline{i}$	$\underline{j}$	$\underline{k}$
1	2	3
2	3	1
3	1	2

TABLE A.1

POSSIBLE NON-ZERO TENSOR ELEMENTS FROM MACROSCOPIC CRYSTAL
SYMMETRY CONSIDERATIONS IN THE D_{2h} POINT GROUP

Second rank tensor elements are given up through fourth order terms in a phenomenological expansion in magnetic field strength. Onsager symmetry has not been included.

The crystal is referenced to its principal coordinate system. The numbers in parentheses indicate the multiplicity of equivalent coefficients.

Element of Tensor	$T_{11}(H)$	$T_{22}(H)$	$T_{33}(H)$	$T_{12}(H)$	$T_{13}(H)$	$T_{23}(H)$	$T_{21}(H)$	$T_{31}(H)$	$T_{32}(H)$
0th order in H	$T°_{11}$	$T°_{22}$	$T°_{33}$						
1st order in H				T_{123}	T_{132}	T_{231}	T_{213}	T_{312}	T_{321}
2nd order in H	T_{1111} T_{1122} T_{1133}	T_{2211} T_{2222} T_{2233}	T_{3311} T_{3322} T_{3333}	$(2)T_{1212}$	$(2)T_{1313}$	$(2)T_{2323}$	$(2)T_{2121}$	$(2)T_{3131}$	$(2)T_{3232}$
3rd order in H	$(6)T_{11123}$	$(6)T_{22213}$	$(6)T_{33312}$	T_{12333} $(3)T_{12113}$ $(3)T_{12223}$	T_{13222} $(3)T_{13112}$ $(3)T_{13233}$	T_{23111} $(3)T_{23122}$ $(3)T_{23133}$	T_{21333} $(3)T_{21113}$ $(3)T_{21223}$	T_{31222} $(3)T_{31112}$ $(3)T_{31233}$	T_{32111} $(3)T_{32122}$ $(3)T_{32133}$
4th order in H	T_{111111} T_{112222} T_{113333} $(6)T_{111122}$ $(6)T_{111133}$ $(6)T_{112233}$	T_{221111} T_{222222} T_{223333} $(6)T_{221122}$ $(6)T_{221133}$ $(6)T_{222233}$	T_{331111} T_{332222} T_{333333} $(6)T_{332233}$ $(6)T_{331122}$ $(6)T_{331133}$	$(4)T_{121112}$ $(4)T_{122221}$ $(12)T_{121233}$	$(4)T_{131333}$ $(4)T_{131113}$ $(12)T_{131223}$	$(4)T_{232333}$ $(4)T_{232223}$ $(12)T_{232311}$	$(4)T_{211222}$ $(4)T_{212111}$ $(12)T_{211233}$	$(4)T_{311333}$ $(4)T_{311113}$ $(12)T_{311223}$	$(4)T_{322333}$ $(4)T_{322223}$ $(12)T_{322311}$

Example: Through 4th order in H

$$T_{11}(H) = T°_{11} + T_{1111} H_1^2 + T_{1122} H_2^2 + T_{1133} H_3^2 + 6T_{1123} H_1 H_2 H_3 + T_{111111} H_1^4 + T_{112222} H_2^4 + T_{113333} H_3^4 + 6T_{111122} H_1^2 H_2^2$$
$$+ 6T_{111133} H_1^2 H_3^2 + 6 T_{112233} H_2^2 H_3^2 + \cdots$$

$$E_i = J_i \, (\rho_{ii}^{\circ} + \rho_{iiii} \, H_i^2 + \rho_{iijj} \, H_j^2 + \rho_{iikk} \, H_k^2)$$

$$+ J_j \, (\rho_{ijk} \, H_k + 2 \, \rho_{ijij} \, H_i \, H_j)$$

$$+ J_k \, (\rho_{ikj} \, H_j + 2 \, \rho_{ikik} \, H_i \, H_k)$$

with the following higher order terms:

$$+ J_i \, (\rho_{iiiiii} \, H_i^4 + \rho_{iijjjj} \, H_j^4 + \rho_{iikkkk} \, H_k^4$$

$$+ 6 \, \rho_{iiiijj} \, H_i^2 \, H_j^2 + 6 \, \rho_{iiiikk} \, H_i^2 \, H_k^2$$

$$+ 6 \, \rho_{iijjkk} \, H_j^2 \, H_k^2)$$

$$+ J_j \, (\rho_{ijkkk} \, H_k^3 + 3 \, \rho_{ijiik} \, H_i^2 \, H_k + 3 \, \rho_{ijjjk} \, H_j^2 \, H_k$$

$$+ 4 \, \rho_{ijiiij} \, H_i^3 \, H_j + 4 \, \rho_{ijijjj} \, H_i \, H_j^3$$

$$+ 12 \, \rho_{ijijkk} \, H_i \, H_j \, H_k^2)$$

$$+ J_k \, (\rho_{ikjjj} \, H_j^3 + 3 \, \rho_{ikiij} \, H_i^2 \, H_j + 3 \, \rho_{ikjkk} \, H_j \, H_k^2$$

$$+ 4 \, \rho_{ikikkk} \, H_i \, H_k^3 + 4 \, \rho_{ikiiik} \, H_i^3 \, H_k$$

$$+ 12 \, \rho_{ikijjk} \, H_i \, H_j^2 \, H_k)$$

In general, throughout this work $\vec{B}$ is used in the magnetic field expansions. This should cause no confusion, since it can be assumed that $B = \mu_o H$ for non-ferromagnetic crystals, where μ_o is the permeability of free space, $\mu_o = 4\pi \times 10^{-7}$ henries per meter. The results of this appendix are valid whether $\vec{B}$ or $\vec{H}$ is used in the expansions.

APPENDIX 2

THEORETICAL DERIVATION OF THE TRANSPORT COEFFICIENTS OF A GENERAL ELLIPSOID

A2.1 THE BOLTZMANN TRANSPORT EQUATION

The Boltzmann transport equation is the continuity equation in phase space. Numerous textbooks and other references discuss the formulation of this equation and methods of solution[1-5].

Using M.K.S. units, this equation may be written as:

$$\frac{\partial f}{\partial t} + \dot{\vec{k}} \cdot \tilde{\nabla} f + \dot{\vec{r}} \cdot \nabla f = \left(\frac{\partial f}{\partial t} \right)_c$$

here: f = the statistical distribution function which distributes electrons (or holes) over the available energy states.

k = the wave vector which is used to label the energy states in reciprocal space.

r = the real space coordinates of an electron.

$\left(\frac{\partial f}{\partial t} \right)_c$ = the time rate of change in the electronic (hole) distribution function due to "collision" interactions.

∇ = the gradient operator in real space.

$$\nabla = \left(\vec{i}_x \frac{\partial}{\partial x} + \vec{i}_y \frac{\partial}{\partial y} + \vec{i}_z \frac{\partial}{\partial z} \right)$$

$$\nabla f = \left(\vec{i}_x \frac{\partial}{\partial x} + \vec{i}_y \frac{\partial}{\partial y} + \vec{i}_z \frac{\partial}{\partial z} \right) f$$

$\tilde{\nabla}$ = the gradient operator in reciprocal space:

$$\tilde{\nabla} = \left(\vec{i}_{kx} \frac{\partial}{\partial k_x} + \vec{i}_{ky} \frac{\partial}{\partial k_y} + \vec{i}_{kz} \frac{\partial}{\partial k_z} \right)$$

$$\tilde{\nabla} f = \left(\vec{i}_{kx} \frac{\partial}{\partial k_x} + \vec{i}_{ky} \frac{\partial}{\partial k_y} + \vec{i}_{kz} \frac{\partial}{\partial k_z} \right) f$$

where the $\vec{i}_x$, $\vec{i}_{kx}$, etc. are the appropriate unit vectors.

In general, the distribution function is a function of real space and reciprocal space coordinates:

$$f = f(\vec{k}, \vec{r})$$

In the steady state (constant applied fields) the Boltzmann equation becomes:

$$\dot{\vec{k}} \cdot \widetilde{\nabla} f + \dot{\vec{r}} \cdot \nabla f = \left(\frac{\partial f}{\partial t}\right)_c \qquad (A.2.1)$$

Now, it has been shown that:[3]

$$\dot{\vec{r}} \equiv \vec{v} = (h)^{-1} \widetilde{\nabla} E \qquad (A.2.2)$$

$$\dot{\vec{k}} = (h)^{-1} F = q(\hbar)^{-1}(\vec{\varepsilon} + \vec{v} \times \vec{B}) \qquad (A.2.3)$$

where: $\hbar = \frac{h}{2\pi}$, h being Planck's constant (h=6.628 x 10^{-34} joule-sec.)

$E \equiv E(\vec{k})$ = describes the total energy of a single electron with

wave vector $\vec{k}$ in reciprocal space.

$\vec{\varepsilon}$ = the total electric field which acts on an electron (hole).

$\vec{F}$ = the accelerating force due to electromagnetic fields.

q = the total charge of the electrical conduction species.

= − 1.601 x 10^{-19} coulomb for electrons.

= + 1.601 x 10^{-19} coulomb for holes.

$\vec{B}$ = the applied magnetic flux density in Webers/m^2.

Hence, the Boltzmann equation becomes:

$$q(\hbar)^{-1} (\vec{\varepsilon} + (\hbar)^{-1} \widetilde{\nabla} E \times \vec{B}) \cdot \widetilde{\nabla} f + (\hbar)^{-1} \widetilde{\nabla} E \cdot \nabla f = \left(\frac{\partial f}{\partial t}\right)_c \qquad (A.2.4)$$

Once again, note that q is numerically negative for electron conduction and numerically positive for hole conduction.

Assume that the conduction medium is chemically homogeneous. Then, in equilibrium:

$$f(\vec{k},r) = f^\circ(\vec{k},r) = f^\circ(\vec{k}) = \cfrac{1}{1 + \exp\left(\cfrac{E(\vec{k})-E_F}{kT}\right)}$$

where $f^\circ(\vec{k})$ is the Fermi-Dirac distribution function.

Here: k = Boltzmann's constant, 1.38×10^{-23} joule/°K.

(not to be confused with the wave vector, $\vec{k}$, which will

always be written as a vector).

E_F = the Fermi level, or electrochemical potential of the particular

conduction species (holes or electrons).

It should be noted that E_F is an explicit function of the absolute

temperature T. When a temperature gradient is applied to the conduction

medium, T becomes an explicit function of position and, therefore, $E_F(T)$

is an implicit function of position in real space.

If the applied fields only slightly perturb the distribution function

from its equilibrium value, the perturbed distribution function may be

written as:

$$f(\vec{k},\vec{r}) = f^\circ - \vec{G} \cdot (\hbar)^{-1} \widetilde{\nabla} E \frac{\partial f^\circ}{\partial E} + \ldots \tag{A.2.5}$$

This is equivalent to expanding the distribution function in spherical

harmonics in reciprocal space[5]. Here, $\vec{G}$ is an explicit function of

energy only and the "equilibrium" distribution function, f°, can vary with

position in real space due to the applied temperature gradient:

$$f^\circ(\vec{k},\vec{r}) = \cfrac{1}{1 + \exp\left[\cfrac{E(\vec{k}) - E_F(T)}{kT(\vec{r})}\right]}$$

It is now assumed that surfaces of constant electron (hole) energy in

reciprocal space are general ellipsoids. That is:

$$E(\vec{k}) = \frac{\hbar^2}{2} \left(\frac{k_1^2}{m_1} + \frac{k_2^2}{m_2} + \frac{k_3^2}{m_3} \right)$$

$$= \frac{\hbar^2}{2} \vec{k} \cdot \overleftrightarrow{\left(\frac{1}{m}\right)} \cdot \vec{k} = \frac{\hbar^2}{2} \vec{k} \cdot \overleftrightarrow{W} \cdot \vec{k} \tag{A.2.6}$$

where

$$\overleftrightarrow{\left(\frac{1}{m}\right)} = \overleftrightarrow{W} = \begin{pmatrix} \dfrac{1}{m_1} & 0 & 0 \\ 0 & \dfrac{1}{m_2} & 0 \\ 0 & 0 & \dfrac{1}{m_3} \end{pmatrix} \tag{A.2.7}$$

is the reciprocal effective mass tensor. The following convention regarding sbuscripts is also being introduced here: Whether in real space or reciprocal space

"x" component $\longrightarrow$ "1"

"y" component $\longrightarrow$ "2"

"z" component $\longrightarrow$ "3"

The presence of one energy extremum will be assumed and it is assumed that the principle coordinates of the ellipsoidal approximation to this extremum coincide with the Cartesian coordinates of reciprocal space. Hence, the effective mass is a diagonal tensor in this coordinate system.

It is now assumed that a tensor relaxation time exists in a form defined by[5]:

$$\left(\frac{\partial f}{\partial t}\right)_c = \vec{G} \cdot \overleftrightarrow{\nu} \cdot (\hbar)^{-1} \widetilde{\nabla}E \frac{\partial f_o}{\partial E} \tag{A.2.8}$$

Here, $\overleftrightarrow{\nu}$ is the inverse tensor to the following relaxation time tensor:

$$\overleftrightarrow{\tau} = \begin{pmatrix} \tau_{11} & 0 & 0 \\ 0 & \tau_{22} & 0 \\ 0 & 0 & \tau_{33} \end{pmatrix} ; \quad \overleftrightarrow{\nu} = \overleftrightarrow{(\tau)}^{-1} = \begin{pmatrix} \dfrac{1}{\tau_{11}} & 0 & 0 \\ 0 & \dfrac{1}{\tau_{22}} & 0 \\ 0 & 0 & \dfrac{1}{\tau_{33}} \end{pmatrix} \tag{A.2.9}$$

The relaxation time tensor is assumed to be diagonal in the same coordinate system as the effective mass. In general, τ_{11}, τ_{22}, and τ_{33} can be different functions of energy. Korenblit[6] has considered the case where the assumed relaxation time is not diagonal in the same coordinate system as the effective mass tensor.

If $\tau = \tau^\circ \delta_{ij}$ (where δ_{ij} is the Kronecker delta), the above form for the collision term reduces to the familiar:

$$(\frac{\partial f}{\partial t})_c = - \frac{f-f^\circ}{\tau^\circ}$$

The Boltzmann equation, Eq. A.2.4, can be linearized by inserting the assumed form for the perturbed distribution function, Eq. A.2.5, performing the differential operations and keeping only the lowest order non-vanishing terms.

With:
$$f = f(\vec{k},\vec{r}) = f^\circ - \vec{G} \cdot (\hbar)^{-1} \widetilde{\nabla}E \frac{\partial f^\circ}{\partial E}$$

$$\nabla f \simeq \nabla f^\circ = T \frac{\partial f^\circ}{\partial E} \nabla(\frac{E-E_F}{T})$$

$$= T (E-E_F) \frac{\partial f^\circ}{\partial E} \nabla(\frac{1}{T}) - \frac{\partial f^\circ}{\partial E} \nabla(E_F) \qquad (A.2.10)$$

and:
$$\widetilde{\nabla} f = \widetilde{\nabla} f^\circ - \widetilde{\nabla}(\vec{G} \cdot (\hbar)^{-1} \widetilde{\nabla}E \frac{\partial f^\circ}{\partial E})$$

$$= \frac{\partial f^\circ}{\partial E} \widetilde{\nabla}E - \hbar \vec{G} \cdot \overleftrightarrow{W} \frac{\partial f^\circ}{\partial E} - (\hbar)^{-1} \widetilde{\nabla}E (\frac{\partial \vec{G}}{\partial E} \cdot \widetilde{\nabla}E) \frac{\partial f^\circ}{\partial E}$$

$$- (\hbar)^{-1} (\vec{G} \cdot \widetilde{\nabla}E) \frac{\partial^2 f^\circ}{\partial E^2} \widetilde{\nabla}E \qquad (A.2.11)$$

In Eq. A.2.11, only the first term is important when vector scalar product multiplied into the $\vec{\varepsilon}$ term of the Boltzmann equation. The second term of Eq. A.2.11 is the only term that gives a non-zero contribution when vector scalar product multiplied into the $\widetilde{\nabla}E \times \vec{B}$ term of the Boltzmann equation.

This is because

$$\widetilde{\nabla} E \times \vec{B} \cdot \widetilde{\nabla} E = 0$$

Thus, collecting Eq. A.2.8-10-11, the Boltzmann equation, Eq. A.2.4, may be written as:

$$q(\hbar)^{-1} \frac{\partial f^\circ}{\partial E} \widetilde{\nabla} E \cdot (\vec{\varepsilon} - \frac{1}{q} \nabla E_F) - q(\hbar)^{-1} \widetilde{\nabla} E \times \vec{B} \cdot (\vec{G} \cdot \overleftrightarrow{W}) \frac{\partial f^\circ}{\partial E}$$

$$+ (\hbar)^{-1} T(E-E_F) \widetilde{\nabla} E \cdot \nabla (\frac{1}{T}) \frac{\partial f^\circ}{\partial E}$$

$$= \vec{G} \cdot \overleftrightarrow{v} \cdot \widetilde{\nabla} E \ (\hbar)^{-1} \frac{\partial f^\circ}{\partial E} \qquad (A.2.12)$$

Now note that the total electric field which acts on a species of charge carrier is given by

$$\vec{\varepsilon} = - \nabla \phi$$

where ϕ is the total electrostatic potential (volts). It is assumed that $\vec{B}$ is a d.c. magnetic field. Hence, the first term of Eq. A.2.12 can be written as:

$$- (\hbar)^{-1} \frac{\partial f^\circ}{\partial E} \widetilde{\nabla} E \cdot \nabla \bar{\mu}$$

Here, $\bar{\mu} = (q\phi + E_F)$ is the nonequilibrium electrochemical potential of the charge carrier species. Recalling that

$$\vec{v} = (\hbar)^{-1} \widetilde{\nabla} E \qquad (A.2.2)$$

and using the above result, the Boltzmann equation, Eq. A.2.12, becomes:

$$- \vec{v} \cdot \nabla \bar{\mu} + T(E-E_F) \vec{v} \cdot \nabla (\frac{1}{T})$$

$$- q \vec{v} \times \vec{B} \cdot (\vec{G} \cdot \overleftrightarrow{W}) = \vec{G} \cdot \overleftrightarrow{v} \cdot \vec{v} \qquad (A.2.13)$$

where the common factor of $\frac{\partial f^\circ}{\partial E}$ has been cancelled out. This equation holds on every surface of constant charge carrier energy in reciprocal space. The quantity:

$$\nabla \bar{\mu} - T(E-E_F) \nabla (\frac{1}{T}) \equiv \vec{P} \qquad (A.2.14)$$

is a vector which is constant in magnitude and direction over a surface of constant energy. Recall, also, the vector identity

$$\vec{A} \times \vec{B} \cdot \vec{C} = \vec{A} \cdot \vec{B} \times \vec{C}$$

Hence, the Boltzmann equation can be written as:

$$- \vec{v} \cdot \vec{P} - q \vec{v} \cdot \vec{B} \times (\vec{G} \cdot \overleftrightarrow{W}) = \vec{v} \cdot \overleftrightarrow{v} \cdot \vec{G} \qquad (A.2.15)$$

or

$$\vec{v} \cdot [\vec{P} + q \vec{B} \times (\vec{G} \cdot \overleftrightarrow{W}) + \overleftrightarrow{v} \cdot \vec{G}] = 0 \qquad (A.2.16)$$

Since $\vec{P}$ and $\vec{G}$ are constant on a surface of constant energy – as also is $\overleftrightarrow{v}$ because of the assumed form of the relaxation time (Eq. A.2.9 and following), the bracketed quantity in Eq. A.2.16 is a constant vector over a constant energy surface in reciprocal space. Since $\vec{v}$ can vary both in direction and magnitude over a constant energy surface, the bracketed term must be identically zero.

$$\vec{P} + q \vec{B} \times (\vec{G} \cdot \overleftrightarrow{W}) + \overleftrightarrow{v} \cdot \vec{G} = 0 \qquad (A.2.17)$$

The problem of obtaining the perturbed distribution function has been reduced to solving this equation for $\vec{G}$. Before continuing with the solution, it is useful to collect the major assumptions and approximations which have been used to produce Eq. A.2.17. These are:

1. The classical Boltzmann equation adequately describes the electronic conduction processes.

2. The perturbed distribution function has the form of Eq. A.2.5.

3. A tensor relaxation time exists. Its elements are functions of energy only.

4. The energy band extremum responsible for the conduction phenomena can be described as a general ellipsoid in reciprocal space – Eq. A.2.6.

5.   Both the effective mass and the relaxation time tensors are diagonal in the same coordinate system. This coordinate system is taken to coincide with the principle axes of the effective mass ellipsoid.

6.   The Boltzmann equation has been linearized. As written in the forms of Eq. A.2.15 or 16, the Boltzmann equation contains the electric field, $\vec{\epsilon}$, and thermal gradient, ∇T, to the first power only.

A.2.2 SOLUTION OF THE BOLTZMANN EQUATION IN THE LIMIT OF LOW MAGNETIC

FIELD STRENGTHS

For very small $\vec{B}$, the second term of Eq. A.2.17 may be neglected. Hence, to zeroth order in magnetic field strength:

$$\vec{P} + \overset{\leftrightarrow}{\nu} \cdot \vec{G}^{(o)} = 0$$

or

$$\vec{G}^{(o)} = -\overset{\leftrightarrow}{\tau} \cdot \vec{P}$$

A better approximation to the actual value of $\vec{G}$ can be obtained by using the above result in Eq. A.2.17:

$$\vec{P} + q \, \vec{B} \times (\vec{G}^{(o)} \cdot \overset{\leftrightarrow}{W}) + \overset{\leftrightarrow}{\nu} \cdot \vec{G}^{(1)} = 0$$

or:

$$\vec{G}^{(1)} = -\overset{\leftrightarrow}{\tau} \cdot \vec{P} - q \, \overset{\leftrightarrow}{\tau} \cdot [\vec{B} \times (\vec{G}^{(o)} \cdot \overset{\leftrightarrow}{W})]$$

$$= -\overset{\leftrightarrow}{\tau} \cdot \vec{P} + q \, \overset{\leftrightarrow}{\tau} \cdot [\vec{B} \times (\vec{P} \cdot \overset{\leftrightarrow}{\tau} \cdot \overset{\leftrightarrow}{W})]$$

Continuing this iteration for one more step:

$$\vec{G} \simeq \vec{G}^{(2)} = -\overset{\leftrightarrow}{\tau} \cdot \vec{P} + q \, \overset{\leftrightarrow}{\tau} \cdot [\vec{B} \times (\vec{P} \cdot \overset{\leftrightarrow}{\tau} \cdot \overset{\leftrightarrow}{W})]$$

$$- q^2 \, \overset{\leftrightarrow}{\tau} \cdot \{\vec{B} \times [(\overset{\leftrightarrow}{\tau} \cdot \overset{\leftrightarrow}{W}) \cdot (\vec{B} \times [\vec{P} \cdot \overset{\leftrightarrow}{\tau} \cdot \overset{\leftrightarrow}{W}])]\}$$

(A.2.18)

A.2.3 MACROSCOPIC TRANSPORT COEFFICIENTS FROM IRREVERSIBLE THERMODYNAMICS

Callen[7] has presented the basic notions and developments of

irreversible thermodynamics. In particular, his one dimensional dynamical

equations (equations 17.10, 11 and 12) can be directly generalized to three

dimensions as follows:

$$- \vec{J}_N = \overset{\leftrightarrow}{L_1^0} \cdot \frac{\nabla(\bar{\mu})}{T} + \overset{\leftrightarrow}{L_2^0} \cdot \nabla(\tfrac{1}{T}) \qquad (A.2.19)$$

$$\vec{J}_Q = \overset{\leftrightarrow}{L_3^0} \cdot \frac{\nabla(\bar{\mu})}{T} + \overset{\leftrightarrow}{L_4^0} \cdot \nabla(\tfrac{1}{T}) \qquad (A.2.20)$$

with the Onsager relations:

$$\overset{\leftrightarrow}{L_1^0}(+\vec{B}) = \overset{\leftrightarrow}{L_1^0}{}^{(T)}(-B)$$

$$\overset{\leftrightarrow}{L_4^0}(+\vec{B}) = \overset{\leftrightarrow}{L_4^0}{}^{(T)}(-B) \qquad (A.2.21)$$

$$\overset{\leftrightarrow}{L_2^0}(+\vec{B}) = \overset{\leftrightarrow}{L_3^0}{}^{(T)}(-B)$$

In the above:

T = absolute temperature − °K

$\vec{J}_N$ = matter flux-particles/m^2-sec.

$\vec{J}_Q$ = heat flux − joules/m^2-sec.

$\bar{\mu}$ = electrochemical potential of transport

species − joules.

$\overset{\leftrightarrow}{L_1^0}{}^{(T)}$ = transpose of matrix $\overset{\leftrightarrow}{L_1^0}$, etc.

$\overset{\leftrightarrow}{L_1^0}$, $\overset{\leftrightarrow}{L_2^0}$, $\overset{\leftrightarrow}{L_3^0}$ and $\overset{\leftrightarrow}{L_4^0}$ are second rank tensors which characterize the dynamics of

the physical system under consideration. These tensors are generally functions

of the intensive parameters of the physical system, such as temperature, T,

and applied magnetic field, $\vec{B}$.

It should also be noted that Eqs. A.2.19 and A.2.20 are only linear approximations to the dynamical response of the physical system to applied "forces". For small gradients of electrochemical potential, $\bar{\mu}$, and temperature, T, the linear approximation will be adequate, especially if the physical system is chemically homogeneous in equilibrium. Finally, note that the Boltzmann equation has been solved in a linear approximation to the effects of $\nabla(\bar{\mu})$ and $\nabla(T)$ - (Eqs. A.2.10, 11-17).

The electric current is just:

$$\vec{J}_E = q \, \vec{J}_N$$

where $\quad q = - 1.601 \times 10^{-19}$ coulomb for electrons

$\quad\quad = + 1.601 \times 10^{-19}$ coulomb for holes.

Hence, Eqs. A.2.19 and 20 can be rewritten as:

$$- \vec{J}_E = \frac{q^2 \overleftrightarrow{L}_1^o}{T} \cdot \nabla(\frac{\bar{\mu}}{q}) + q \, \overleftrightarrow{L}_2^o \cdot \nabla(\frac{1}{T}) \tag{A.2.22}$$

$$\vec{J}_Q = \frac{q \, \overleftrightarrow{L}_3^o}{T} \cdot \nabla(\frac{\bar{\mu}}{q}) + \overleftrightarrow{L}_4^o \cdot \nabla(\frac{1}{T}) \tag{A.2.23}$$

Defining:

$$\overleftrightarrow{L}_1 = \frac{q^2}{T} \overleftrightarrow{L}_1^o \; ; \quad \overleftrightarrow{L}_2 = q \, \overleftrightarrow{L}_2^o$$

$$\overleftrightarrow{L}_3 = \frac{q}{T} \overleftrightarrow{L}_3^o \; ; \quad \overleftrightarrow{L}_4 = \overleftrightarrow{L}_4^o \tag{A.2.24}$$

The above equations become:

$$- \vec{J}_E = \overleftrightarrow{L}_1 \cdot \nabla(\frac{\bar{\mu}}{q}) + \overleftrightarrow{L}_2 \cdot \nabla(\frac{1}{T}) \tag{A.2.25}$$

$$\vec{J}_Q = \overleftrightarrow{L}_3 \cdot \nabla(\frac{\bar{\mu}}{q}) + \overleftrightarrow{L}_4 \cdot \nabla(\frac{1}{T}) \tag{A.2.26}$$

where now, because of the Onsager relations on the original $\overleftrightarrow{L}_1^o$, $\overleftrightarrow{L}_2^o$, etc. (Eq. A.2.21):

$$\overleftrightarrow{L_1}(+B) = \overleftrightarrow{L_1}^{(T)}(-B)$$

$$\overleftrightarrow{L_4}(+B) = \overleftrightarrow{L_4}^{(T)}(-B) \qquad\qquad (A.2.27)$$

$$\overleftrightarrow{L_2}(+B) = T\,\overleftrightarrow{L_3}^{(T)}(-B)$$

The reason for casting the macroscopic dynamical equations in the form of Eqs. A.2.25 and 26 is that the coefficients $\overleftrightarrow{L_1}$, $\overleftrightarrow{L_2}$, $\overleftrightarrow{L_3}$ and $\overleftrightarrow{L_4}$ can be immediately identified from the corresponding equations which will be calculated using microscopic transport theory. Anticipating this calculation, which appears as Section A.2.4, more familiar and useful tensor quantities will be interpreted in terms of $\overleftrightarrow{L_1}$, $\overleftrightarrow{L_2}$, $\overleftrightarrow{L_3}$ and $\overleftrightarrow{L_4}$.

To this end:

I. Set $\nabla(T) = 0$.

Then:

$$- \vec{J}_E = \overleftrightarrow{L_1} \cdot \nabla\left(\frac{\bar{\mu}}{q}\right)$$

but

$$\nabla\left(\frac{\bar{\mu}}{q}\right) = \nabla\left(\frac{E_F}{q} + \phi\right) = \nabla\phi = -\vec{\varepsilon}$$

since $\nabla(T) = 0$ and the conduction medium is assumed to be chemically homogeneous in equilibrium.

Hence

$$\vec{J}_E = \overleftrightarrow{L_1} \cdot \vec{\varepsilon}$$

or

$$\overleftrightarrow{\sigma} = \overleftrightarrow{L_1} \qquad\qquad (A.2.28)$$

where $\overleftrightarrow{\sigma}$ is the electrical conductivity tensor (ohm-m)$^{-1}$.

II. Set $\vec{J}_E = 0$, then:

$$\overleftrightarrow{L_1} \cdot \nabla\left(\frac{\bar{\mu}}{q}\right) = -\overleftrightarrow{L_2} \cdot \nabla\left(\frac{1}{T}\right) = +\frac{\overleftrightarrow{L_2}}{T^2} \cdot \nabla(T)$$

Defining the absolute thermoelectric power of a medium by:

$$\nabla(\frac{\bar{\mu}}{q}) = - \vec{\varepsilon} = -\overleftrightarrow{\alpha} \cdot \nabla(T) \qquad (A.2.29)$$

it is seen that:

$$\overleftrightarrow{\alpha} = -\frac{\overleftrightarrow{(L_1)}^{-1} \cdot \overleftrightarrow{L_2}}{T^2}$$

where $\overleftrightarrow{(L_1)}^{-1}$ is the inverse tensor to $\overleftrightarrow{L_1}$. Thus:

$$\overleftrightarrow{\alpha} = -\frac{1}{T^2} \overleftrightarrow{\rho} \cdot \overleftrightarrow{L_2} \quad (\frac{volts}{°K}) \qquad (A.2.30)$$

where $\overleftrightarrow{\rho}$ is the electrical resistivity tensor which is the inverse to $\overleftrightarrow{\sigma}$.

III. Set $\vec{J}_E = 0$ but $\vec{J}_Q$ and $\nabla(T) \neq 0$, then:

$$\vec{J}_Q = (\overleftrightarrow{L_3} \cdot \frac{\overleftrightarrow{(L_1)}^{-1} \cdot \overleftrightarrow{L_2}}{T^2} - \frac{\overleftrightarrow{L_4}}{T^2}) \cdot \nabla(T)$$

but

$$\vec{J}_Q = - \overleftrightarrow{\kappa} \cdot \nabla(T) \qquad (A.2.31)$$

Hence, the thermal conductivity (under the usual open circuit electrical conditions) is:

$$\overleftrightarrow{\kappa} = \frac{1}{T^2} (\overleftrightarrow{L_4} - \overleftrightarrow{L_3} \cdot \overleftrightarrow{\rho} \cdot \overleftrightarrow{L_2}) \quad (\frac{watts}{m-°K}) \qquad (A.2.32)$$

If the thermal conductivity is measured in the absence of a magnetic field, then:

$$\overleftrightarrow{\kappa} (B=0) = \frac{1}{T^2} (\overleftrightarrow{L_4} - \frac{\overleftrightarrow{L_2}(T) \cdot \overleftrightarrow{\rho} \cdot \overleftrightarrow{L_2}}{T}) \quad (\frac{watts}{m-°K}) \qquad (A.2.33)$$

since

$$\overleftrightarrow{L_3} (B=0) = \frac{1}{T} \overleftrightarrow{L_2}(T) \ (B=0)$$

which is inferred by the Onsager reciprocity conditions (see Eqs. A.2.27).

The original (and correct) statement of Onsager reciprocity requires that:

$$\overrightarrow{\sigma}(+B) = \overrightarrow{\sigma^{(T)}}(-B)$$

$$\overrightarrow{\kappa}(+B) = \overrightarrow{\kappa^{(T)}}(-B) \tag{A.2.34}$$

and imposes no symmetry relations on the thermoelectric power tensor when considered by itself.

The important results of this section are presented below. The results are stated in index notation. The Einstein summation convention of summing over repeated indicies ($i = 1$ to 3) is observed.

Electrical conductivity:

$$\sigma_{ij}(B) = (\rho(B))_{ij}^{-1} = (L_1(B))_{ij} \tag{A.2.35}$$

Thermoelectric power:

$$\alpha_{ij}(B) = \frac{-1}{T^2}(\rho(B))_{ik}(L_2(B))_{kj} \tag{A.2.36}$$

when $B = 0$

$$\alpha_{ij} = \frac{-1}{T^2}\rho_{ik}(L_2)_{kj} \tag{A.2.37}$$

Thermal conductivity:

$$\kappa_{ij}(B) = \frac{1}{T^2}[(L_4(B))_{ij} - (\overrightarrow{L}_3(B))_{ik}(\rho(B))_{k\ell}(L_2(B))_{\ell j}] \tag{A.2.38}$$

when $B = 0$

$$\kappa_{ij} = \frac{1}{T^2}[(L_4)_{ij} - \frac{1}{T}\rho_{k\ell}(L_2)_{ki}(L_2)_{\ell j}] \tag{A.2.39}$$

A.2.4   CALCULATION OF THE MACROSCOPIC TRANSPORT COEFFICIENTS FROM ELECTRONIC TRANSPORT THEORY

The net electrical conduction current density for a single species of charge carriers (holes or electrons) is simply:

$$\vec{J}_E = q \; \vec{J}_N = \frac{q}{4\pi^3} \int_{BZ} \vec{v} \; f(\vec{k},\vec{r}) d\vec{k}$$

or

$$\vec{J}_E = \frac{q}{4\pi^3} \int_{BZ} \vec{v} \; g(\vec{k}) d\vec{k} \tag{A.2.40}$$

where $f(\vec{k},\vec{r}) = f^{\circ}(\vec{k},\vec{r}) + g$, the subscript BZ indicates integration over the first Brillouin zone and, referring to Eq. A.2.5:

$$g = -\; \vec{G} \cdot (\hbar)^{-1} \; \widetilde{\nabla} E \; \frac{\partial f^{\circ}}{\partial E} = -\; \vec{G} \cdot \vec{v} \; \frac{\partial f^{\circ}}{\partial E} \tag{A.2.41}$$

The solution for $\vec{G}$ has been given as Eq. A.2.18.

Following Callen[8] and Nye[9], the thermal current density can be written as:

$$\vec{J}_Q = \vec{J}_U - \bar{\mu} \; \vec{J}_N \tag{A.2.42}$$

Here:

$\vec{J}_U$ = the total energy current density: $\dfrac{\text{joules}}{\text{m}^2\text{-sec}}$

$\bar{\mu}$ = E_F, the equilibrium electrochemical potential : joules

$\vec{J}$ = particle current density: $\dfrac{1}{\text{m}^2\text{-sec}}$

Now:

$$\vec{J}_U = \frac{1}{4\pi^3} \int_{BZ} E\vec{v} g(\vec{k}) d\vec{k}$$

and

$$\bar{\mu} \; \vec{J}_N = \frac{E_F}{4\pi^3} \int_{BZ} \vec{v} g(\vec{k}) d\vec{k}$$

Hence,

$$\vec{J}_Q = \frac{1}{4\pi^3} \int_{BZ} (E-E_F)\vec{v}\ g(\vec{k})d\vec{k} \qquad (A.2.43)$$

Now consider the form of $g(\vec{k})$:

$$g(\vec{k}) = -\ \vec{G}\cdot\vec{v}\ \frac{\partial f^\circ}{\partial E}$$

and from Eq. A.2.18:

$$\vec{G} = -\ \overleftrightarrow{\tau}\cdot\vec{P} + q\ \overleftrightarrow{\tau}\cdot[\vec{B} \times (\vec{P}\cdot\overleftrightarrow{\tau}\cdot\overleftrightarrow{W})]$$
$$-\ q^2\overleftrightarrow{\tau}\cdot\{\vec{B}\times[(\overleftrightarrow{\tau}\cdot\overleftrightarrow{W})\cdot(\vec{B}\times[\vec{P}\cdot\overleftrightarrow{\tau}\cdot\overleftrightarrow{W}])]\} \qquad (A.2.18)$$

By definition:

$$\vec{P} = q\ \nabla(\frac{\bar{\mu}}{q}) - T(E-E_F)\ \nabla(\frac{1}{T}) \qquad (A.2.14)$$

Thus, it is seen that $g(\vec{k})$ and, therefore, $\vec{J}_E$ and $\vec{J}_Q$ each can be split up into two terms. One term depends on $\nabla(\bar{\mu}/q)$ and the other on $\nabla(1/T)$.

In the experimental portion of this work, no thermal measurements were made in an applied magnetic field. Hence, only the zero magnetic field terms will be developed in the explicitly temperature gradient dependent integrals contained in $\vec{J}_E$ and $\vec{J}_Q$.

Before continuing, define:

$$\underline{\beta} = \overleftrightarrow{\tau}\cdot\overleftrightarrow{W} = \begin{pmatrix} \dfrac{\tau_{11}}{m_1} & 0 & 0 \\ 0 & \dfrac{\tau_{22}}{m_2} & 0 \\ 0 & 0 & \dfrac{\tau_{33}}{m_3} \end{pmatrix} \qquad (A.2.44)$$

Note that $\underline{\beta}$, Equation A.2.44, is essentially the inverse of β, Equation 5.19.

Then

$$\vec{G} = - \overleftrightarrow{\tau} \cdot \vec{P} + q \overleftrightarrow{\tau} \cdot [\vec{B} \times \vec{P} \cdot \overleftrightarrow{\underline{\beta}}] - q^2 \overleftrightarrow{\tau} \cdot \{ \vec{B} \times [\underline{\beta} \cdot (\vec{B} \times \vec{P} \cdot \overleftrightarrow{\underline{\beta}})] \} \qquad (A.2.45)$$

When expressed in index notation:

$$g(\vec{k}) = - \vec{G} \cdot \vec{v} \frac{\partial f^\circ}{\partial E}$$

$$= v_h \tau_{hj} P_j \frac{\partial f^\circ}{\partial E}$$

$$- q \, v_h \tau_{hk} \varepsilon_{k\ell m} B_\ell P_j \beta_{jm} \frac{\partial f^\circ}{\partial E}$$

$$+ q^2 \, v_h \tau_{hp} \varepsilon_{pnf} B_n \beta_{fk} \varepsilon_{k\ell m} B_\ell P_j \beta_{jm} \qquad (A.2.46)$$

where, once again, the Einstein summation convention is used. τ_{hk} and β_{hk} are elements of diagonal matricies. Finally, $\varepsilon_{k\ell m}$ is the permutation symbol which is defined as:

$$\varepsilon_{123} = \varepsilon_{231} = \varepsilon_{312} = + 1$$

$$\varepsilon_{213} = \varepsilon_{321} = \varepsilon_{132} = - 1 \qquad (A.2.47)$$

and $\varepsilon_{k\ell m} = 0$ whenever two or more indicies are the same.

In the same notation:

$$P_j = q \, \nabla_j (\frac{\bar{\mu}}{q}) - T(E - E_F) \, \nabla_j (\frac{1}{T}) \qquad (A.2.48)$$

where ∇_j is the jth component of the real space gradient operator, ∇. Using these developments, the electrical and heat current densities become:

$$(J_E)_i = \frac{q}{4\pi^3} \int_{BZ} v_i \, g(\vec{k}) \, d\vec{k}$$

$$= \frac{q^2}{4\pi^3} \left(\int_{BZ} v_i v_h \tau_{hj} \frac{\partial f^\circ}{\partial E} \, d\vec{k} \right) \nabla_j \left(\frac{\bar{\mu}}{q} \right)$$

$$- \frac{q^3}{4\pi^3} \left(\int_{BZ} v_i v_h \tau_{hk} \epsilon_{k\ell m} B_\ell \beta_{jm} \frac{\partial f^\circ}{\partial E} \, d\vec{k} \right) \nabla_j \left(\frac{\bar{\mu}}{q} \right)$$

$$+ \frac{q^4}{4\pi^3} \left(\int_{BZ} v_i v_h \tau_{hp} \epsilon_{pnf} B_n \beta_{fk} \epsilon_{k\ell m} B_\ell \beta_{jm} \frac{\partial f^\circ}{\partial E} \, d\vec{k} \right) \nabla_j \left(\frac{\bar{\mu}}{q} \right)$$

$$- \frac{q}{4\pi^3} \left(\int_{BZ} T(E-E_F) v_i v_h \tau_{hj} \frac{\partial f^\circ}{\partial E} \, d\vec{k} \right) \nabla_j \left(\frac{1}{T} \right) \tag{A.2.49}$$

And

$$(J_Q)_i = \frac{1}{4\pi^3} \int_{BZ} (E-E_F) v_i \, g(\vec{k}) \, d\vec{k}$$

$$= \frac{q}{4\pi^3} \left(\int_{BZ} (E-E_F) v_i v_h \tau_{hj} \frac{\partial f^\circ}{\partial E} \, d\vec{k} \right) \nabla_j \left(\frac{\bar{\mu}}{q} \right)$$

$$- \frac{1}{4\pi^3} \left(\int_{BZ} T(E-E_F)^2 v_i v_h \tau_{hj} \frac{\partial f^\circ}{\partial E} \, d\vec{k} \right) \nabla_j \left(\frac{1}{T} \right) \tag{A.2.50}$$

From Eqs. A.2.25 and A.2.28:

$$-(J_E)_i = \sigma_{ij}(\vec{B}) \, \nabla_j \left(\frac{\bar{\mu}}{q} \right) + (L_2)_{ij} \, \nabla_j \left(\frac{1}{T} \right) \tag{A.2.51}$$

$$(J_Q)_i = (L_3)_{ij} \, \nabla_j \left(\frac{\bar{\mu}}{q} \right) + (L_4)_{ij} \, \nabla_j \left(\frac{1}{T} \right) \tag{A.2.52}$$

As already mentioned, the magnetic field dependences of $\overleftrightarrow{L_2}$, $\overleftrightarrow{L_3}$ and $\overleftrightarrow{L_4}$ will not be considered. This is because only the magnetic field dependence of σ_{ij} $(=(L_1)_{ij})$ enters into the experimental body of this work.

Examing Eqs. A.2.49-50, it is immediately seen that:

$$(L_2)_{ij} = \frac{q}{4\pi^3} \int_{BZ} T(E-E_F) v_i v_h \tau_{hj} \frac{\partial f^\circ}{\partial E} d\vec{k} \qquad (A.2.53)$$

$$(L_3)_{ij} = \frac{q}{4\pi^3} \int_{BZ} (E-E_F) v_i v_h \tau_{hj} \frac{\partial f^\circ}{\partial E} d\vec{k} \qquad (A.2.54)$$

$$(L_4)_{ij} = -\frac{1}{4\pi^3} \int_{BZ} T(E-E_F)^2 v_i v_h \tau_{hj} \frac{\partial f^\circ}{\partial E} d\vec{k} \qquad (A.2.55)$$

Notice that $(L_2)_{ij} = T(L_3)_{ij}$ which corresponds to Eq. A.2.27 for the matricies L_2 and L_3 which are diagonal in this model.

Finally writing:

$$\sigma_{ij}(B) = \sigma_{ij}^\circ + \sigma_{ijk} B_k + \sigma_{ijk\ell} B_k B_\ell \qquad (A.2.56)$$

it is seen that:

$$\sigma_{ij}^\circ = -\frac{q^2}{4\pi^3} \int_{BZ} v_i v_h \tau_{hj} \frac{\partial f^\circ}{\partial E} d\vec{k} \qquad (A.2.57)$$

$$\sigma_{ijk} = \frac{q^3}{4\pi^3} \int_{BZ} v_i v_h \tau_{h\ell} \epsilon_{\ell km} \beta_{jm} \frac{\partial f^\circ}{\partial E} d\vec{k} \qquad (A.2.58)$$

and finally:

$$\sigma_{ijk\ell} = \frac{-q^4}{4\pi^3} \left[\frac{\epsilon_{pkf} \epsilon_{n\ell m} + \epsilon_{p\ell f} \epsilon_{nkm}}{2} \right] \int_{BZ} v_i v_h \tau_{hp} \beta_{fn} \beta_{jm} \frac{\partial f^\circ}{\partial E} d\vec{k}$$

$$(A.2.59)$$

It should be recalled that:

1. $q = + 1.601 \times 10^{-19}$ coulomb for holes

    $q = - 1.601 \times 10^{-19}$ coulomb for electrons

2. $\overleftrightarrow{\tau}$ and $\overleftrightarrow{\beta}$ are diagonal tensors.

A.2.5 ANALYTICAL EVALUATION OF THE TRANSPORT COEFFICIENTS

The integrals which express the transport coefficients (Eqs. A.2.53, 54, 55, 57, 58, and 59) now will be transformed into a form which is convenient for numerical evaluation. The independent variable in these integrals will be changed from $\vec{k}$, a reciprocal lattice vector, to E, the energy of a hole or electron. This transformation is easily made since:

1. $E(\vec{k})$ is assumed to be a quadratic form in $\vec{k}$.

2. The elements of the diagonal relaxation time tensor

     are taken to be functions of energy only.

All of the integrals of interest can be expressed in the form:

$$I = \frac{1}{4\pi^3} \int_{BZ} v_i v_j \frac{\partial f^\circ}{\partial E} F(E) d\vec{k} \qquad (A.2.60)$$

where F(E) is some function of energy. Now:

$$E(\vec{k}) = \frac{\hbar^2}{2} \left(\frac{k_1^2}{m_1} + \frac{k_2^2}{m_2} + \frac{k_3^3}{m_3} \right) = (k_1^{\circ 2} + k_2^{\circ 2} + k_3^{\circ 2}) \qquad (A.2.61)$$

Here:

$$k_1^\circ = \frac{\hbar k_1}{\sqrt{2m_1}} \; ; \quad k_2^\circ = \frac{\hbar k_2}{\sqrt{2m_2}} \; ; \quad k_3^\circ \; \frac{\hbar k_3}{\sqrt{2m_3}} \qquad (A.2.62)$$

In this new orthogonal coordinate system in reciprocal space:

$$d\vec{k} = dk_1 dk_2 dk_3 = \frac{\partial k_1}{\partial k_1^\circ} \frac{\partial k_2}{\partial k_2^\circ} \frac{\partial k_3}{\partial k_3^\circ} dk_1^\circ dk_2^\circ dk_3^\circ$$

$$= \frac{\sqrt{8m_1 m_2 m_3}}{\hbar^3} dk_1^\circ dk_2^\circ dk_3^\circ \qquad (A.2.63)$$

Also:

$$v_i = \frac{1}{\hbar} \frac{\partial E}{\partial k_i} = \frac{1}{\hbar} \frac{\partial E}{\partial k_i^\circ} \frac{\partial k_i^\circ}{\partial k_i} = \frac{1}{\hbar} \frac{\hbar}{\sqrt{2m_i}} \frac{\partial E}{\partial k_i^\circ}$$

$$v_i = \frac{2}{\sqrt{2m_i}} k_i^\circ \; ; \quad v_j = \frac{2}{\sqrt{2m_j}} k_j^\circ \qquad (A.2.64)$$

Thus:

$$I = \frac{1}{4\pi^3} \frac{\sqrt{8\, m_1 m_2 m_3}}{\hbar^3} \frac{4}{2\sqrt{m_i m_j}} \int_{BZ} k_i^\circ k_j^\circ \frac{\partial f^\circ}{\partial E} F(E)\, d\vec{k}^\circ$$

Concentrate on the integral. This can be written as:

$$\int_{BZ} k_i^\circ k_j^\circ \frac{\partial f^\circ}{\partial E} F(E)\, d\vec{k}^\circ = \int_0^\infty dE \frac{\partial f^\circ}{\partial E} F(E) \iint_{E=constant} \frac{ds}{|\widetilde{\nabla}^\circ E|} k_i^\circ k_j^\circ$$

where $|\widetilde{\nabla}^\circ E|$ is the absolute magnitude of the gradient of E with respect to the new reciprocal space coordinates, k_i°.

$$|\widetilde{\nabla}^\circ E| = 2\sqrt{k_1^{\circ 2} + k_2^{\circ 2} + k_3^{\circ 2}} = 2\sqrt{E}$$

Hence:

$$\int_{BZ} k_i^\circ k_j^\circ \frac{\partial f^\circ}{\partial E} F(E)\, d\vec{k}^\circ = \frac{1}{2} \int_0^\infty dE (E)^{-1/2} F(E) \frac{\partial f^\circ}{\partial E} \iint_{E=constant} ds\, k_i^\circ k_j^\circ$$

The energy integral has been written with limits of zero to infinity. This assumes that:

1. The reference level for energy (E=0) is taken at the band edge.

2. The Fermi-Dirac distribution function, f°, cuts off the integral long before the energy band departs from ellipsoidal form or before other bands begin to contribute to the conduction processes.

Now, k_i° and k_j° are orthogonal vectors if $i \neq j$. Thus:

$$\iint_{E=constant} ds\, k_i^\circ k_j^\circ = \frac{4\pi}{3} E^2 \delta_{ij}$$

Thus:

$$\int_{BZ} k_i^\circ k_j^\circ \frac{\partial f^\circ}{\partial E} F(E)\, d\vec{k}^\circ = \frac{2\pi}{3} \int_0^\infty (E)^{3/2} F(E) \frac{\partial f^\circ}{\partial E} dE\, \delta_{ij} \qquad (A.2.65)$$

Finally

$$I = \frac{2}{3} \frac{\sqrt{8\, m_1 m_2 m_3}}{2\pi^2 \hbar^3} \frac{\delta_{ii}}{m_i} \int_0^\infty F(E)\, (E)^{3/2} \frac{\partial f^\circ}{\partial E}\, dE \qquad (A.2.66)$$

The concentration of charge carriers - holes or electrons - is:

$$n \text{ or } p = \frac{\sqrt{8\, m_1 m_2 m_3}}{2\pi^2 \hbar^3} \int_0^\infty f^\circ(E)\, \sqrt{E}\ dE \quad \text{per } (m)^3 \qquad (A.2.67)$$

In passing, the expression above defines a density of states effective mass as:

$$m_d = (m_1 m_2 m_3)^{1/3} \qquad (A.2.68)$$

Combining Eqs. A.2.66 and 67 it is seen that

$$I = - \frac{p}{m_i}\ <F(E)>\ \delta_{ij} \qquad (A.2.69)$$

where

$$<F(E)> = \frac{-2/3 \displaystyle\int_0^\infty F(E)\, (E)^{3/2} \frac{\partial f^\circ}{\partial E}\, dE}{\displaystyle\int_0^\infty f^\circ(E)\, (E)^{1/2}\, dE} \qquad (A.2.70)$$

Using these developments, it is seen that:

$$(L_2)_{ij} : \text{Eq. A.2.53} : F(E) = qT\, (E-E_F)\tau_{ii}$$

$$(L_2)_{ij} = - \frac{p}{m_i}\ <qT(E-E_F)\tau_{ii}>\ \delta_{ij} = - \frac{pqT}{m_i}\ <(E-E_F)\tau_{ii}>\delta_{ij}$$

$$(A.2.71)$$

$$(L_3)_{ij} : \text{Eq. A.2.54} : F(E) = q\, (E-E_F)\tau_{ii}$$

$$(L_3)_{ij} = - \frac{p}{m_i}\ <q(E-E_F)\tau_{ii}>\ \delta_{ij} = - \frac{pq}{m_i}\ <(E-E_F)\tau_{ii}>\ \delta_{ij}$$

$$(A.2.72)$$

$$(L_4)_{ij} : \text{Eq. A.2.55} : F(E) = - T(E-E_F)^2\tau_{ii}$$

$$(L_4)_{ij} = - \frac{p}{m_i}\ <-T(E-E_F)^2\tau_{ii}>\ \delta_{ij} = \frac{pT}{m_i}\ <(E-E_F)^2\tau_{ii}>\ \delta_{ij}$$

$$(A.2.73)$$

And the electrical conductivities are:

$$\sigma_{ij}^{\circ} : \text{Eq. A.2.57} : F(E) = -q^2 \tau_{ii}$$

$$\sigma_{ij}^{\circ} = -\frac{p}{m_i} <-q^2 \tau_{ii}> \delta_{ij} = \frac{pq^2}{m_i} <\tau_{ii}> \delta_{ij} \qquad \text{(A.2.74)}$$

$$\sigma_{ijk} : \text{Eq. A.2.58} : F(E) = q^3 \tau_{ii} \epsilon_{ikj} \beta_{jj}$$

$$\sigma_{ijk} = -\frac{p}{m_i} <q^3 \tau_{ii} \epsilon_{ikj} \beta_{jj}>$$

$$\sigma_{ijk} = \epsilon_{ijk} \frac{pq^3}{m_i m_j} <\tau_{ii} \tau_{jj}> \qquad \text{(A.2.75)}$$

$$\sigma_{ijk\ell} : \text{Eq. A.2.59}$$

$$F(E) = -q^4 \left[\frac{\epsilon_{ikf}\epsilon_{f\ell j} + \epsilon_{i\ell f}\epsilon_{fkj}}{2} \right] \tau_{ii} \beta_{ff} \beta_{jj}$$

and

$$\sigma_{ijk} = \frac{pq^4}{m_i m_j} \left[\frac{\epsilon_{ikf}\epsilon_{f\ell j} + \epsilon_{i\ell f}\epsilon_{fkj}}{2} \right] <\tau_{ii} \tau_{jj} \beta_{ff}> \qquad \text{(A.2.76)}$$

The tensors $\overleftrightarrow{L_2}$, $\overleftrightarrow{L_3}$, $\overleftrightarrow{L_4}$, and $\overleftrightarrow{\sigma^{\circ}}$ all have simple forms – they are diagonal second rank tensors. Their elements will not be written out explicitly. σ_{ijk} and $\sigma_{ijk\ell}$ are the elements of higher rank tensors – rank 3 and 4 respectively. The non zero elements are listed below.

$$\sigma_{ijk} : \text{From Eq. A.2.75}$$

$$\sigma_{123} = -\sigma_{213} = \frac{pq^3}{m_1 m_2} <\tau_{11} \tau_{22}>$$

$$\sigma_{312} = -\sigma_{132} = \frac{pq^3}{m_1 m_3} <\tau_{11} \tau_{33}> \qquad \text{(A.2.77)}$$

$$\sigma_{231} = -\sigma_{321} = \frac{pq^3}{m_2 m_3} <\tau_{22} \tau_{33}>$$

$$\sigma_{ijk\ell} : \text{From Eq. A.2.76}$$

$$\sigma_{1111} = \sigma_{2222} = \sigma_{3333} = 0$$

$$\sigma_{1122} = - pq^4 \frac{<\tau_{11}^2 \tau_{33}>}{m_1^2 m_3}$$

$$\sigma_{1133} = - pq^4 \frac{<\tau_{11}^2 \tau_{22}>}{m_1^2 m_2}$$

$$\sigma_{2211} = - pq^4 \frac{<\tau_{22}^2 \tau_{33}>}{m_2^2 m_3} \qquad (A.2.78)$$

$$\sigma_{2233} = - pq^4 \frac{<\tau_{22}^2 \tau_{11}>}{m_2^2 m_1}$$

$$\sigma_{3311} = - pq^4 \frac{<\tau_{33}^2 \tau_{22}>}{m_3^2 m_2}$$

$$\sigma_{3322} = - pq^4 \frac{<\tau_{33}^2 \tau_{11}>}{m_3^2 m_1}$$

$$\sigma_{1212} = \sigma_{1313} = \sigma_{2323} = \frac{1}{2} pq^4 \frac{<\tau_{11}\tau_{22}\tau_{33}>}{m_1 m_2 m_3}$$

A.2.6 FORMULAS FOR THE INVERSION OF THE TRANSPORT COEFFICIENTS

Formulas for $\overleftrightarrow{L}_2(B=0)$, $\overleftrightarrow{L}_3(B=0)$, $\overleftrightarrow{L}_4(B=0)$ and $\overleftrightarrow{L}_1(B\neq0) = \overleftrightarrow{\sigma}(B\neq0)$ have been developed in the previous section.

Formulas which express thermoelectric power, thermal conductivity, and the electrical resistivities in terms of these quantities are given below. The Einstein summation convention is used.

Thermoelectric Power:

When $\vec{B} = 0$:

$$\alpha_{ij} = -\frac{1}{T^2} \rho^o_{ik} (L_2)_{kj} \qquad (A.2.36)$$

Thermal Conductivity:

When $\vec{B} = 0$:

$$\kappa_{ij} = \frac{1}{T^2} [(L_4)_{ij} - \frac{1}{T} \rho^\circ_{k\ell} (L_2)_{ki} (L_2)_{\ell j}] \qquad (A.2.38)$$

Since, by definition, the electrical resistivity tensor is the inverse tensor to the electrical conductivity tensor:

$$\sigma_{ij} (\vec{B}) \rho_{jk} (\vec{B}) = \delta_{ik} \quad . \qquad (A.2.79)$$

Using the low magnetic field approximations:

$$\sigma_{ij}(\vec{B}) = \sigma^\circ_{ij} + \sigma_{ijp} B_p + \sigma_{ij\ell p} B_\ell B_p \qquad (A.2.80)$$

$$\rho_{jk}(\vec{B}) = \rho^\circ_{jk} + \rho_{jkm} B_m + \rho_{jkmn} B_m B_n$$

in Eq. A.2.79 it is seen that:

$$\sigma^\circ_{ij} \rho^\circ_{jk} = \delta_{ik}$$

or

$$\rho^\circ_{ij} = (\sigma^\circ)^{-1}_{ij} \qquad (A.2.81)$$

Furthermore:

$$\rho_{\ell kp} = - \rho^\circ_{\ell i} \sigma_{ijp} \rho^\circ_{jk} \qquad (A.2.82)$$

And:

$$\rho_{\ell kmn} = \frac{1}{2} \rho^\circ_{\ell i} \rho^\circ_{jp} \rho^\circ_{rk} [\sigma_{ijn} \sigma_{prm} + \sigma_{ijm} \sigma_{prn}]$$
$$-\rho^\circ_{\ell i} \rho^\circ_{jk} \sigma_{ijmn} \qquad (A.2.83)$$

A.2.7 SUMMARY OF ANALYTICAL EXPRESSIONS FOR EXPERIMENTALLY MEASURED TRANSPORT COEFFICIENTS

The results of the preceding two sections can be used to produce analytical expressions for the electronic transport parameters which are usually determined by experiment.

The following results have been derived for a single energy band extremum which has general ellipsoids for constant energy surfaces in reciprocal space. The effective mass tensor is assumed to be diagonal in the Cartesian coordinate system which is used. The relaxation time is assumed to be a diagonal tensor in the same coordinate system. The elements of the diagonal relaxation time tensor are assumed to be functions of energy only. These functions of energy are not necessarily the same. $f° = f°(E)$ is the Fermi-Dirac distribution function. Since p-type ZnSb was the subject of this investigation, p denotes hole density in the following and $q = + 1.601 \times 10^{-19}$ coulomb.

$$\tau_{ii}(E) \equiv \tau_{ii}$$

Recall that for some function of energy, $F(E)$:

$$\langle F(E) \rangle \equiv \frac{-2/3 \int_0^\infty F(E) \, E^{3/2} \frac{\partial f°}{\partial E} \, dE}{\int_0^\infty f°(E) \, (E)^{1/2} dE} \tag{A.2.70}$$

The Einstein summation convention is not used in the following formulas.

Thermoelectric Power:

$$\alpha_{ij} = \frac{1}{Tq} \frac{\langle (E-E_F)\tau_{ii} \rangle}{\langle \tau_{ii} \rangle} \delta_{ij} \quad \frac{\text{volts}}{°K} \tag{A.2.84}$$

Hole Conduction Thermal Conductivity:

$$\kappa_{ij} = \frac{p}{Tm_i} \left[\langle (E-E_F)^2 \tau_{ii} \rangle - \frac{\langle (E-E_F)\tau_{ii} \rangle^2}{\langle \tau_{ii} \rangle} \right] \delta_{ij} \frac{\text{watts}}{\text{m-}°K} \tag{A.2.85}$$

Lorentz Numbers:

$$L_{ij} = \frac{\kappa_{ii}}{\sigma_{ij}T} = \frac{1}{T^2 q^2} \left[\frac{\langle (E-E_F)^2 \tau_{ii} \rangle}{\langle \tau_{ii} \rangle} - \frac{\langle (E-E_F)\tau_{ii} \rangle^2}{\langle \tau_{ii} \rangle^2} \right] \delta_{ij} \tag{A.2.86}$$

$\vec{B} = 0$ **Electrical Resistivity:**

$$\rho_{ij}^{\circ} = \frac{m_i}{pq^2 \langle\tau_{ii}\rangle}\,\delta_{ij} \quad \text{ohm-meter} \tag{A.2.87}$$

Hall Coefficients:

$$\rho_{ijk} = -\,\epsilon_{ijk}\,\frac{1}{pq}\,\frac{\langle\tau_{ii}\,\tau_{jj}\rangle}{\langle\tau_{ii}\rangle\langle\tau_{jj}\rangle}\,\frac{m^3}{\text{coulomb}} \tag{A.2.88}$$

Magnetoresistance Coefficients:

$$\rho_{iiii} = 0 \tag{A.2.89}$$

$$\rho_{iijj} = \frac{1}{pm_k}\left[\frac{\langle\tau_{ii}^2\tau_{kk}\rangle}{\langle\tau_{ii}\rangle^2} - \frac{\langle\tau_{ii}\tau_{kk}\rangle^2}{\langle\tau_{ii}\rangle^2\langle\tau_{kk}\rangle}\right]\frac{\text{ohm-m}^5}{\text{weber}^2}$$

$$\rho_{ijij} = \frac{-1}{2pm_k}\left[\frac{\langle\tau_{ii}\tau_{jj}\tau_{kk}\rangle}{\langle\tau_{ii}\rangle\langle\tau_{jj}\rangle} - \frac{\langle\tau_{ii}\tau_{kk}\rangle\,\langle\tau_{jj}\tau_{kk}\rangle}{\langle\tau_{ii}\rangle\langle\tau_{jj}\rangle\langle\tau_{kk}\rangle}\right]$$

The Einstein summation convention is not used in the above formulas. Unless required by the Kronecker delta, δ_{ij}, $i \neq j \neq k$ and can be assigned according to any of the six permutations of 1, 2 and 3.

A.2.8 BIBLIOGRAPHY

1. C. Kittel, Elementary Statistical Physics, Sections 3 and 40, John Wiley & Sons, Inc., New York, N.Y. (1958).

2. A.H. Wilson, The Theory of Metals, 2nd Ed., Ch. 8, Cambridge University Press, Cambridge, England, 1958.

3. R.A. Smith, Wave Mechanics of Crystalline Solids, Ch. 10, Chapman & Hall, London, England, (1961).

4. A.C. Beer, Galvanomagnetic Effects in Semiconductors, Section 5, Academic Press, New York, N.Y., (1963).

5. W.M. Bullis, Galvanomagnetic Effects in n-Type Germanium, Ph.D. thesis, Department of Physics, Massachusetts Institute of Technology, Cambridge, Mass., (1956).

6. I. YA. Korenblit, Sov. Phys. Solid State, $\underline{2}$, 2739, (1961).

7. H.B. Callen, Thermodynamics, Chaps. 15, 16, 17, John Wiley & Sons, Inc., New York, N.Y. (1960).

8. H.B. Callen, Op. Cit., Eq. 17.8.

9. J.F. Nye, Physical Properties of Crystals, p. 220-1, Oxford University Press, London, (1960).

APPENDIX 3

LONGITUDINAL MAGNETORESISTANCE OF AN
ENERGY BAND OF GENERAL ELLIPSOIDAL FORM

A.3.1 CALCULATION OF THE MAGNETORESISTANCE

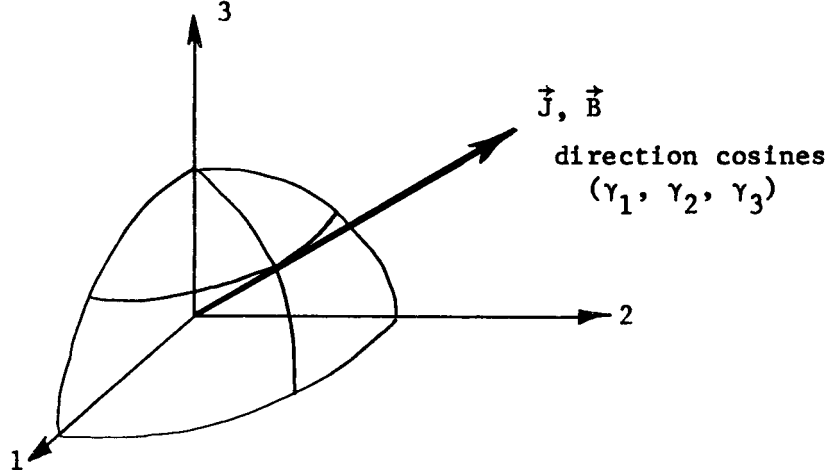The geometry of interest is shown below in Figure A.3.1.

Fig. A.3.1 Off Axis Longitudinal Magnetoresistance Geometry

The electric current density and magnetic field density vectors are assumed
to be parallel (longitudinal magnetoresistance) and directed in a general
orientation with respect to the 1, 2 and 3 axes. The direction cosines of
this arbitrary orientation with respect to the 1, 2 and 3 axes are denoted
by γ_1, γ_2 and γ_3 respectively.

Thus, the electric current density and the magnetic field density have
the components:

$$\vec{J}: \quad J_1 = J\gamma_1; \quad J_2 = J\gamma_2; \quad J_3 = J\gamma_3 \tag{A.3.1}$$

$$\vec{B}: \quad B_1 = B\gamma_1; \quad B_2 = B\gamma_2; \quad B_3 = B\gamma_3 \tag{A.3.2}$$

Let B = 0, then since the ellipsoid is being referenced to its principal
coordinate system:

$$E_1 = J\gamma_1 \, \rho_{11}^\circ; \quad E_2 = J\gamma_2 \, \rho_{22}^\circ; \quad E_3 = J\gamma_3 \, \rho_{33}^\circ \tag{A.3.3}$$

These components may be combined to give the resultant electric field:

$$E^\circ = J(\gamma_1^2 \rho_{11}^\circ + \gamma_2^2 \rho_{22}^\circ + \gamma_3^2 \rho_{33}^\circ) \qquad (A.3.4)$$

When $B \neq 0$; the results of Appendix 1 may be used to write:

$$E_1 = J\gamma_1(\rho_{11}^\circ + \rho_{1111} \gamma_1^2 B^2 + \rho_{1122} \gamma_2^2 B^2 + \rho_{1133} \gamma_3^2 B^2)$$

$$+ J\gamma_2(\rho_{123} \gamma_3 B + 2\rho_{1212} \gamma_1\gamma_2 B^2)$$

$$+ J\gamma_3(\rho_{132} \gamma_2 B + 2\rho_{1313} \gamma_1\gamma_3 B^2) \qquad (A.3.5)$$

Similarly:

$$E_2 = J\gamma_2(\rho_{22}^\circ + \rho_{2222} \gamma_2^2 B^2 + \rho_{2211} \gamma_1^2 B^2 + \rho_{2233} \gamma_3^2 B^2)$$

$$+ J\gamma_3(\rho_{231} \gamma_1 B + 2\rho_{2323} \gamma_2\gamma_3 B^2)$$

$$+ J\gamma_1(\rho_{213} \gamma_3 B + 2\rho_{2121} \gamma_1\gamma_2 B^2) \qquad (A.3.6)$$

And finally:

$$E_3 = J\gamma_3(\rho_{33}^\circ + \rho_{3333} \gamma_3^2 B^2 + \rho_{3322} \gamma_2^2 B^2 + \rho_{3311} \gamma_1^2 B^2)$$

$$+ J\gamma_1(\rho_{312} \gamma_2 B + 2\rho_{3131} \gamma_1\gamma_3 B^2)$$

$$+ J\gamma_2(\rho_{321} \gamma_1 B + 2\rho_{3232} \gamma_2\gamma_3 B^2) \qquad (A.3.7)$$

For a general ellipsoid, the on-axis longitudinal magnetoresistances are zero. Hence

$$\rho_{1111} = \rho_{2222} = \rho_{3333} = 0 \qquad (A.3.8)$$

Also, the total electric field, with $B \neq 0$ is given by:

$$E = \gamma_1 E_1 + \gamma_2 E_2 + \gamma_3 E_3 \qquad (A.3.9)$$

And the change in the longitudinal electric field which is caused by the application of the magnetic field is:

$$\Delta E = E - E^\circ \qquad (A.3.10)$$

Inserting Equations A.3.4, 5, 6, 7, 8 and 9 into Equation A.3.10 yields:

$$\frac{\Delta E}{JB^2} = \frac{E - E^{\circ}}{JB^2} =$$

$$(\rho_{1122} + \rho_{2211} + 4\rho_{1212})\gamma_1^2\gamma_2^2$$
$$+ (\rho_{1133} + \rho_{3311} + 4\rho_{1313})\gamma_1^2\gamma_3^2$$
$$+ (\rho_{2233} + \rho_{3322} + 4\rho_{2323})\gamma_2^2\gamma_3^2$$

The Hall effect terms do not appear in the above since $\rho_{ijk} = -\rho_{jik}$ and they cancel in pairs. Also, terms of the form ρ_{ijij} and ρ_{jiji} have been combined since they are equal.

From Equations A.2.89 it is seen that:

$$\rho_{iijj} = \frac{1}{pm_k} \left[\frac{<\tau_{ii}^2 \tau_{kk}>}{<\tau_{ii}>^2} - \frac{<\tau_{ii}\tau_{kk}>^2}{<\tau_{ii}>^2<\tau_{kk}>} \right] \qquad (A.3.12)$$

and

$$\rho_{ijij} = \frac{-1}{2pm_k} \left[\frac{<\tau_{ii}\tau_{ii}\tau_{kk}>}{<\tau_{ii}><\tau_{jj}>} - \frac{<\tau_{ii}\tau_{kk}><\tau_{ii}\tau_{kk}>}{<\tau_{ii}><\tau_{jj}><\tau_{kk}>} \right] \qquad (A.3.13)$$

In Equations A.3.12 and 13, i, j, k range over 1, 2, 3 and $i \neq j \neq k$. Hence, it is seen that for relaxation times of the forms (refer to Chapter 5):

(C). A scalar function of energy:

$$\tau = F(E) \qquad (A.3.14)$$

(D). A tensor with a factorable energy dependence - the tensor

being diagonal in the same coordinate system as the effective

mass:

$$\overset{\leftrightarrow}{\tau} = \begin{pmatrix} \tau_1 & 0 & 0 \\ 0 & \tau_2 & 0 \\ 0 & 0 & \tau_3 \end{pmatrix} F(E) \qquad (A.3.15)$$

the longitudinal magnetoresistance of a general ellipsoid valence band vanishes regardless of the direction of the electric current density vector. As an example of the use of Equations A.3.12 and A.3.13 to obtain this result, the second term on the right hand side of Equation A.3.11 will be explicitly evaluated for a relaxation of the form "D" (Equation A.3.15 above):

$$\dot{\rho}_{1133} = \frac{\tau_2}{pm_2} \left[\frac{\langle F(E)^3 \rangle}{\langle F(E) \rangle^2} - \frac{\langle F(E)^2 \rangle^2}{\langle F(E) \rangle^3} \right]$$

$$\rho_{3311} = \rho_{1133}$$

and

$$\rho_{1313} = \frac{-\tau_2}{2pm_2} \left[\frac{\langle F(E)^3 \rangle}{\langle F(E) \rangle^2} - \frac{\langle F(E)^2 \rangle^2}{\langle F(E) \rangle^3} \right]$$

And the claimed result, $(\rho_{1133} + \rho_{3311} + 4\rho_{1313}) = 0$, is true.

The bulk of the experimental results, namely the isotropic thermoelectric power (Section 4.3.2), the isotropic Hall coefficients (Section 4.5), and the observed numerical symmetry in the magnetoresistance coefficients, all imply that the relaxation time is of form "C" or "D" (Equations A.3.14 and 15, above). Thus, it is not surprising that a nearly zero longitudinal magneto-resistance was observed on the three off-axis samples investigated (Section 4.7.3.2 and Figures 4.29 and 4.30).

A.3.2 ESTIMATION OF THE NUMERICAL MAGNITUDES OF THE PLANAR HALL COEFFICIENTS

Using the above results, it is seen that

$$-2\rho_{1212} = \rho_{1122} = \rho_{2211} \tag{A.3.16}$$

$$-2\rho_{1313} = \rho_{1133} = \rho_{3311} \tag{A.3.17}$$

$$-2\rho_{2323} = \rho_{2233} = \rho_{3322} \tag{A.3.18}$$

Using the experimental results of Table 4.5 and Section 4.7.3.2, it is

seen that for:

Eq. A.3.16: $+ 170 \simeq 200 \simeq 200$

and for:

Eq. A.3.17: $+ 48 \simeq 74 \simeq 90$

The experimentally determined results for Equation A.3.17 are seen to contain quite a bit of experimental error. This is within the $\pm$ 25% probable error assigned to the plane Hall coefficients and the $\pm$ 10% probable error assigned to the other magnetoresistance coefficients.

Using the results of Table 4.5, ρ_{2323} can be estimated as:

$$\rho_{2323} \simeq - \frac{1}{2} (130) = - 65 \times 10^{-9} \frac{\text{ohm-cm}}{(\text{kilogauss})^2}$$

This estimate has been included in Table 4.5

ERRATA

THERMAL AND ELECTRONIC TRANSPORT
PROPERTIES OF ZINC ANTIMONIDE

Page:

v.   Section 4.3.3 appears on p. 79

viii.   TABLE 5.1 COMPARISON OF MAGNETORESISTANCE RATIOS AND....

4.   line 5:   ... Bridgman method.

          line 10: each of the planes of easy cleavage.

          last line: ... α_{33} = 440 $\mu V/°K$

10.   TABLE 1.1 (cont.) last line of second row:

                    0.61 ± 0.03 (4.2°K)

11.   Add to first row of table: EFFECTIVE MASSES:

          ELLIPSOID SYMMETRY AXIS IN "a" DIRECTION.

16.   read: 1.5 BIBLIOGRAPHY

41.   last line: ... (Section 3.2.2 and Figure 3.4)...

77.   Figure caption: Figure 4.3 α vs Logσ

78.   Fifth line from bottom: ... (refer to Section 4.4)...

79.   Read: 4.3.3 THERMAL CONDUCTIVITY MEASUREMENTS

101.   9th line: ... a given bracket seems to ...

110.   Second line at the very top of Figure 4.30:

                  ]ENCLOSES DATA POINTS FOR
                    SAMPLE GV-25-1

125.   Last line: ... transverse magnetoresistance results (77.3°K).

133.   4th line from bottom: ... axis system of the crystal.

146.   Eq. (A.2.2) read: $\vec{r} \equiv \vec{v} = (\hbar)^{-1} \overset{\sim}{\nabla} E$

          Eq. (A.2.3) read: $\vec{k} = (\hbar)^{-1} \vec{F} = ...$

148.   Eq. (A.2.6) read: $= \frac{\hbar^2}{2} \vec{k} \cdot \overset{\leftrightarrow}{W} \cdot \vec{k}$

          6th line: ... subscripts is also being introduced here: ...

176.   7th line: ... assigned to the planar Hall ...